Università degli Studi di Padova

Università degli Studi di Napoli Federico II

Funded by the European Union
NextGenerationEU

Ministero dell'Università e della Ricerca

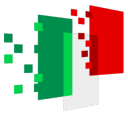

Italiadomani
PIANO NAZIONALE DI RIPRESA E RESILIENZA

Università degli Studi di Padova
Centro di Ateneo "Centro Ricerche Fusione" (CRF) c/o Consorzio RFX

Università degli Studi di Napoli Federico II
Dipartimento di Ingegneria Elettrica e delle Tecnologie dell'Informazione

---

Ph.D. COURSE IN: FUSION SCIENCE AND ENGINEERING

CYCLE XXXVIII

Laser ablation models and experimental activities in support of the implementation of a LIBS diagnostics for the BiGyM linear plasma device for fusion-relevant applications

Thesis written with the financial contribution of the European Union - Next Generation EU - National Recovery and Resilience Plan (NRRP), M4C2 – Investment 3.1 - Area ESFRI Energy - Call for tender No. 3264 of 28-12-2021 of Italian University and Research Ministry (MUR), Project ID IR0000007, MUR Concession Decree No. 243 of 04-08-2022, CUP B53C22003070006, "NEFERTARI - New Equipment for Fusion Experimental Research and Technological Advancements with RFX Infrastructure".

Coordinator
Prof. Emanuele Sartori

Supervisors
Dr. Anna Cremona
Prof. Gianmaria De Tommasi

Ph.D. Student
Stefano Francesco Cipelli
Student ID 2097706

Academic Year 2024/2025

Abstract

Laser-Induced Breakdown Spectroscopy (LIBS) is a powerful and versatile laser-based diagnostic technique widely used to analyze the chemical composition of solids, liquids, and gases. By applying optical emission spectroscopy to a laser-induced plasma, LIBS enables rapid and minimally invasive elemental and isotopic characterization of a thin superficial layer, typically without the need for sample preparation.
Owing to these intrinsic features, LIBS is currently considered a promising diagnostic tool for in-situ monitoring of Plasma Facing Components (PFCs) in magnetic confinement fusion devices, such as tokamaks and Linear Plasma Devices (LPDs). Compared with other post-mortem diagnostics, LIBS enables remote measurements in harsh environments and provides depth-resolved information, key capabilities for investigating processes such as impurity deposition and fuel retention, which are critical issues for future nuclear fusion devices.
The main objective of this thesis is to develop some preparatory activities, including conceptual design, numerical modeling, and experiments, for the installation of an in-situ LIBS diagnostics dedicated to fusion-relevant plasma-material interaction studies on the BiGyM LPD, the upgraded version of GyM (CNR-ISTP, Milan).
The first outcome of the thesis is the definition of the diagnostic components and a preliminary layout. Based on a literature review of existing LIBS systems and experiments, together with some simple spectral sensitivity analyses, a picosecond Nd:YAG laser and a compact, high-resolution IsoPlane 320 spectrometer were identified as suitable instruments to perform in-situ fuel retention studies on BiGyM. In addition, a preliminary technical drawing of the optical path connecting the laser system to the linear device was designed.
A substantial contribution of this work is represented by the development of a finite element numerical model of the laser ablation process, conceived as a support tool for the LIBS diagnostics. The modeling activity, implemented using COMSOL Multiphysics, initially focuses on the nanosecond pulse regime,

which is currently the most widely adopted approach in fusion-related LIBS applications. The model describes laser energy deposition, heat diffusion, phase transitions, and material removal, enabling the prediction of ablation crater features (depth and diameter) as well as the temperature evolution within the computational domain. The modeling framework was subsequently extended to the picosecond regime, in order to progressively align with the diagnostic parameters that will be used on BiGyM. This extension enables the investigation of a different computational approach, describing the temperature evolution through separate heating dynamics for the electron and lattice subsystems. Both approaches were successfully validated by comparing predicted crater characteristics with ablation crater data obtained from dedicated laser irradiation experiments.

The final part of this thesis includes an experimental activity on in-situ retention LIBS measurements performed on the PSI-2 linear device (FZJ, Jülich). This experiment provided practical insight into hydrogen isotope detection in fusion-relevant materials and enabled the extraction of retention data for tantalum, a potential but still less explored alternative to tungsten as a PFC.

Overall, the results obtained in this thesis, combining preliminary diagnostic design, numerical modeling, and experimental results about laser ablation and retention measurements, provide a solid basis for the development and implementation of an in-situ LIBS diagnostic system on the BiGyM linear plasma device.

Contents

1 Nuclear fusion and Plasma Wall Interaction **1**
- 1.1 Nuclear energy . . . 1
- 1.2 Nuclear fusion and tokamak devices . . . 2
- 1.3 Plasma-Wall Interaction . . . 5
- 1.4 Linear Plasma Devices as support facilities for nuclear fusion studies 6
  - 1.4.1 GyM linear plasma device . . . 7
  - 1.4.2 The upgrade: BiGyM linear plasma device . . . 10

2 Theoretical LIBS introduction and motivation of the work **13**
- 2.1 Theoretical background . . . 14
  - 2.1.1 Laser fundamentals . . . 14
  - 2.1.2 LIBS: diagnostic components and different layouts . . . 18
  - 2.1.3 Plasma plume temporal evolution . . . 20
  - 2.1.4 Laser energy absorption mechanisms . . . 22
  - 2.1.5 Laser ablation mechanisms . . . 25
  - 2.1.6 Plume expansion and emission . . . 27
- 2.2 State of the art of LIBS in nuclear fusion . . . 30
- 2.3 State of the art of laser ablation modeling . . . 32
- 2.4 Thesis layout and objectives . . . 34

3 LIBS instrumentation for BiGyM **37**
- 3.1 Influence of laser parameters on LIBS performance . . . 37
  - 3.1.1 Pulse duration . . . 38
  - 3.1.2 Pulse energy and fluence . . . 39
  - 3.1.3 Wavelength . . . 42
  - 3.1.4 Repetition rate . . . 44
  - 3.1.5 PL2231A-10 Ekspla laser parameters . . . 45
- 3.2 Spectrometer . . . 47
- 3.3 Optical path design . . . 51

4 Nanosecond laser ablation modeling **55**
- 4.1 Foundations of thermal modeling and validation of thermal response . . . 56
  - 4.1.1 Governing equation and laser heat source definition . . . 57
  - 4.1.2 First validation step: millisecond laser ablation of alumina 58
  - 4.1.3 Second validation step: nanosecond laser ablation of yttria 60

4.2 Nanosecond laser ablation model and validation for tungsten and silicon 63
4.2.1 Model assumptions and boundary conditions 63
4.2.2 Material removal mechanisms 65
4.2.3 Plasma shielding 67
4.2.4 Experimental 68
4.2.5 Results for tungsten ablation 71
4.2.6 Results for silicon ablation 76

5 Picosecond laser ablation modeling **83**
5.1 Two-Temperature Model equations and first validation step 83
5.1.1 Governing equations 84
5.1.2 Model validation with reference results 85
5.2 Picosecond laser ablation model and validation for tungsten . . . 87
5.2.1 Model assumptions, geometry and boundary conditions . 87
5.2.2 Material removal mechanism 88
5.2.3 Experimental 89
5.2.4 Validation against tungsten experimental data 91

6 In-situ LIBS investigation of short-term deuterium retention in tungsten and tantalum **99**
6.1 Experimental layout, procedure and methodologies 100
6.2 Spectra analysis and outgassing curve reconstruction 104
6.3 Results of NRA measurements 112

7 Conclusions and perspectives **117**

Bibliography **123**

Acknowledgments **137**

1 Nuclear fusion and Plasma Wall Interaction

1.1 Nuclear energy

The increasing global energy demand represents one of the greatest challenges of the 21st century. The continued reliance on fossil fuels, which currently dominate the global energy mix, is associated with greenhouse gas emissions that contribute significantly to global warming. Renewable energy sources such as wind and solar provide clean and potentially unlimited alternatives; however, their intermittent nature, low energy density, and currently higher associated costs limit their capability to fully satisfy total energy needs.
In this context, controlled thermonuclear fusion represents a promising candidate for a reliable and clean energy solution, characterized by the absence of greenhouse gas emissions during operation, capability to work in steady-state conditions, and a much higher energy density than the renewable sources mentioned above. Unlike fission reactors, where the fuel consists of heavy nuclides such as uranium, fusion relies on lighter nuclei (hydrogen isotopes); this avoids the production of long-lived radioactive transuranic elements in the decay chain. Furthermore, in a fusion reactor the fuel must be continuously supplied and it is rapidly consumed, so the amount of fuel mass inside the chamber always remains small, preventing the risk of uncontrolled chain reactions.
Despite these advantages, achieving an energy gain from thermonuclear fusion remains an important scientific and technological challenge. To ignite and sustain fusion reactions, it is necessary to produce a thermonuclear plasma characterized by a temperature of the order of $2 \cdot 10^8$ K, while high heat and particle fluxes ($\sim 10\,\mathrm{MW/m^2}$ and $10^{24}\,\mathrm{m^{-2}\,s^{-1}}$ respectively [1]) are continuously emitted. These extreme conditions require the exploration of new regimes in plasma

physics and impose strict requirements on materials, which must withstand very harsh environments. To address these challenges, large-scale international projects are currently being pursued. Among them, ITER [2], currently under construction, aims to achieve a fusion energy gain close to 10, while DEMO [3] is intended to demonstrate net electric power generation from nuclear fusion. In this context, the selection and development of suitable materials for plasma-facing components, as well as the investigation of their behavior after intense heat and particle fluxes, are essential research topics.

1.2 Nuclear fusion and tokamak devices

The nuclear fusion reaction consists of the merging of two or more light nuclei, mainly hydrogen and its isotopes, to produce a heavier nucleus accompanied by an energy release, which arises from the mass difference between the reactants and the products. The most relevant fusion reaction for energy production involves deuterium (D) and tritium (T) [4]:

$$\mathrm{D} + \mathrm{T} \longrightarrow \alpha + \mathrm{n} + 17.6\,\mathrm{MeV}. \tag{1.1}$$

This reaction has the advantage of exhibiting the highest cross section for the lowest particle energy, so it is the easiest to achieve compared to other fusion reactions involving hydrogen isotopes. The energy released per reaction is 17.6 MeV in the form of kinetic energy of the products, mostly carried by the neutron (14.1 MeV).

The simplest concept of a fusion reactor could be the impact of a deuteron beam on a tritium target, but this layout would be energetically inefficient due to energy losses in the target, especially by Coulomb collisions. For this reason, the most viable approach is to generate a hot and confined thermonuclear plasma, in which a large fraction of fuel is ionized and fusion reactions occur through collisions between plasma particles themselves.

To ignite and sustain fusion reactions, the plasma must be sufficiently hot and dense, with an energy confinement long enough to have an appreciable rate of fusion reactions. This requirement is described by the so-called triple product: the product of plasma temperature T, density n, and energy confinement time τ_E that must be sufficiently high [5]. An important threshold is represented by the ignition condition, in which the thermonuclear plasma is self-sustained by alpha particles emitted from fusion reactions, which compensate the losses generated by radiation emission and transport. This condition can be expressed by the Lawson criterion [5]:

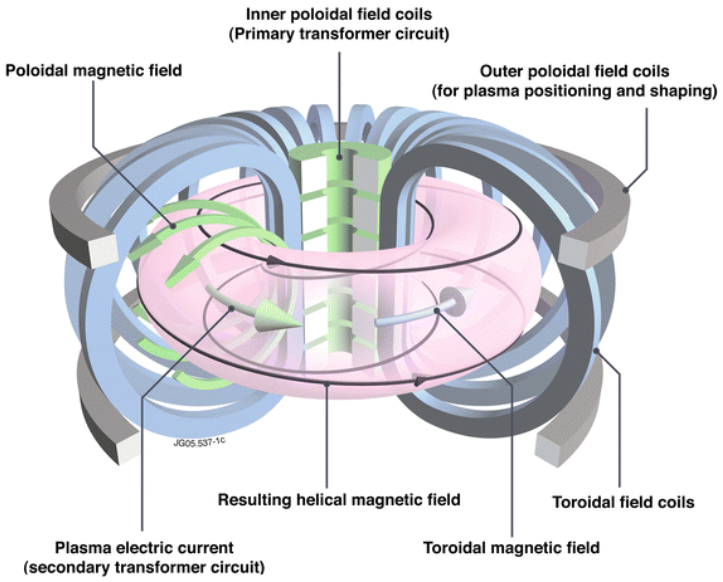

Figure 1.1: Simplified scheme of a tokamak configuration [7].

$$n\tau_E T \gtrsim 3 \cdot 10^{21}\,\mathrm{m}^{-3}\,\mathrm{s\,keV}. \tag{1.2}$$

In stars, the confinement is naturally guaranteed by the gravitational force. Since this mechanism cannot be reproduced on Earth, two main approaches have been developed to achieve plasma confinement:

- **Magnetic Confinement Fusion (MCF)**, where strong magnetic fields are employed to shape and confine the plasma, preventing charged particles from escaping.
- **Inertial Confinement Fusion (ICF)**, where high-power laser beams are used to compress small fuel pellets to reach extremely high densities and temperatures for very short times.

Among the two approaches, MCF is currently the most extensively investigated, and the studies presented in this thesis are positioned within this framework.
Of the various devices developed for magnetic confinement fusion, the tokamak is the most widely studied configuration. The tokamak design was proposed in the Soviet Union in the 1950s [6] and has subsequently become the reference approach for magnetic fusion research. The basic concept consists of generating a plasma inside a doughnut-shaped vacuum chamber and confining it using a combination of toroidal and poloidal magnetic fields, which together generate helical magnetic field lines.

Figure 1.1 illustrates a schematic layout of the tokamak configuration. The toroidal field is produced by external magnetic coils surrounding the chamber, while the poloidal component is induced by an electrical current flowing toroidally in the plasma; the latter is driven by a transformer system in which the primary circuit is the central solenoid and the secondary one is constituted by the plasma itself.
To separate the region occupied by the plasma from the internal walls of the machine the widely adopted strategy in advanced tokamaks is to generate an X-point in the magnetic field, such that there is a boundary between closed and open magnetic surfaces [8]. In this way, heat and particles escaping from magnetically confined plasma are guided to dedicated wall components, in a region called the divertor. Among the Plasma-facing Components (PFCs), which are the structures directly exposed to plasma, the divertor is the one receiving the highest heat and particle loads.
Tokamaks are considered nowadays the most promising configuration for MCF. Several large experimental devices have been constructed and operated worldwide over the last few decades.
Among these, the JET tokamak, located in Culham (UK) [9], is the largest tokamak ever operated and played a central role in the development of D-T fusion research. JET is currently under decommissioning after completing its last experimental campaign in 2023.
Alongside JET, a significant number of research tokamaks are contributing to plasma physics and fusion technology research. Important examples include JT-60SA (Japan) [10], EAST (China) [11], and ASDEX Upgrade (Germany) [12], all of which are currently operational.
The most ambitious tokamak project is ITER, which is under construction in Cadarache (France); it is a work in progress involving 35 different countries and aims to demonstrate a substantial energy gain (factor of 10) from a fusion plasma. In addition to ITER, other important projects include the SPARC [13] device, under development in the United States, which aims to demonstrate the energy gain with a compact device exploiting high-temperature superconducting magnets, and the BEST tokamak in China, designed as a compact plasma experiment to bridge the gap between present and future machines.
All these tokamaks, particularly the ones aiming at producing long discharges for energy gain demonstration, include components, such as first walls and divertor, which, due to physical processes such as magnetic lines deformation or plasma instabilities, are coming into contact with the hot plasma. These PFCs are subjected to extreme thermal and particle fluxes, involving phenomena called Plasma-Wall Interactions (PWI). Research and dedicated experiments in this

branch of plasma physics are fundamental to ensure good reactor performance and internal structure integrity.

1.3 Plasma-Wall Interaction

In magnetic confinement fusion devices, the plasma cannot be perfectly confined and fluxes of particles and energy inevitably reach PFCs. For a large experimental tokamak such as ITER, these fluxes are estimated to reach values of approximately $10\,\mathrm{MW/m^2}$ and $10^{24}\,\mathrm{m^{-2}s^{-1}}$ in the divertor region, and around $2\,\mathrm{MW/m^2}$ and $10^{21}\,\mathrm{m^{-2}s^{-1}}$ on the first walls during steady-state operations [14, 15, 16]. These values can become even higher during transient events such as Edge Localized Modes (ELMs), which are plasma instabilities that can cause rapid bursts of energy and particles [4].
When plasma interacts with material surfaces, a variety of processes may take place, whose nature depends on both the plasma composition and the characteristics of the target material. These phenomena can strongly affect plasma performance, as well as the lifetime and integrity of PFCs. For this reason, understanding PWI is a fundamental aspect for the design, safety, and economy of a fusion reactor. The most relevant physical and chemical phenomena for magnetic fusion devices are briefly described below.

Erosion: this category refers to processes by which atoms are removed from wall materials and enter into the plasma. Both chemical and physical processes need to be taken into account, dividing erosion mechanisms mainly into two categories. The first is the physical sputtering, caused by direct impact of incident energetic ions, which transfer momentum generating one or more chain collisions, resulting in atom removal. The other is the chemical erosion, in which reactions between incident particles and surface atoms cause mass removal. The latter is especially relevant when carbon-based materials are involved. Monitoring and controlling erosion is fundamental, since it is a limiting factor for the lifetime of components; moreover, impurity release into the plasma can degrade its performance and thus energy production.

Deposition and redeposition: atoms eroded from the wall can travel and subsequently redeposit onto the PFCs. Depending on plasma parameters and atomic properties, the process can occur immediately (prompt redeposition), which mitigates net erosion, or after some time, during which atoms migrate through the plasma in the form of dust, redeposit in different

locations, and generate mixed material layers that can be preferentially sputtered.

Fuel retention: this phenomenon occurs when part of the incident D and T flux originating from the plasma becomes trapped in the material instead of being released back into the plasma. Two main mechanisms are typically distinguished: implantation, in which incident ions are trapped inside defects on the surface and can diffuse into the material bulk, or co-deposition, in which mixed layers of eroded impurities and fuel atoms are generated on PFCs. Fuel retention is a critical issue for future reactors, both because tritium breeding is necessary for a sustainable fuel cycle and because excessive retention poses safety and regulatory challenges due to induced radioactivity.

Helium interaction: As a product of D-T fusion reactions, He will accumulate in burning plasmas as an impurity. Its interaction with tungsten (W), the main candidate material for divertor components, can induce significant surface modifications. A relevant example is the growth of W-fuzz, which consists of fiber-form nanostructures growing on the W surface. Although W-fuzz can reduce physical sputtering it alters the surface morphology and thermophysical properties of the target. More generally, He bombardment can cause high-temperature embrittlement and volumetric swelling, degrading material strength and potentially compromising component performance.

A comprehensive understanding of all these processes is crucial to ensure safety, efficiency, and economic viability of fusion reactors. For this reason, dedicated PWI experiments are indispensable, both for developing strategies for damage minimization and for identifying the most suitable material combinations that will enable long-time, sustainable operation of future fusion devices.

1.4 Linear Plasma Devices as support facilities for nuclear fusion studies

Although the present day tokamaks can already achieve plasma discharge parameters close to those expected in future reactors, there are still some physical parameters that cannot be reached. In particular, very high particle fluxes and fluences (i.e. flux integrated over time), as well as surface temperatures of PFCs cannot be reproduced. In this context Linear Plasma Devices (LPDs) represent a cost-effective and efficient solution for performing dedicated PWI experiments.

In an LPD, a plasma column is generated inside a cylindrical vacuum chamber and confined radially by an axial magnetic field produced by solenoidal coils. Samples of different materials can be mounted on a sample holder and exposed directly to the plasma. Since the discharge is continuously sustained by an energy source reaching a steady-state configuration, higher fluence values comparable to those foreseen for reactor operation can be reached after several hours of exposure.
Compared to tokamaks, LPDs provide greater accessibility for instrumentation and diagnostics. This allows precise control over plasma parameters and sample surface temperature, enabling the exposure of samples under pre-selected scenarios and ensuring the reproducibility of experimental conditions.
Several facilities worldwide have been constructed following this design. One of the most important LPDs is MAGNUM-PSI [17], located at the Dutch Institute for Fundamental Energy Research (DIFFER, the Netherlands). The machine exploits a cascade arc plasma source to produce a hot, dense plasma, directed towards the targets by a superconducting magnet. The entire structure is approximately 15 m long, including a water-cooled vacuum vessel surrounded by superconducting coils, capable of generating a magnetic field intensity up to 2.5 T; the machine can expose materials to ITER-relevant divertor conditions, achieving ion fluxes $\sim 10^{25}\,\mathrm{m^{-2}s^{-1}}$ and heat fluxes up to $\geq 10\,\mathrm{MW/m^2}$. Another important facility is PSI-2 [18, 19], located at the Forschungszentrum Jülich (FZJ, Germany). The device is able to produce a high current arc discharge between a heated cathode and an anode in a low-pressure environment. The machine is approximately 6 m long and operates with an axial magnetic field up to 100 mT in the target exposure region. In PSI-2, the ion flux can reach the maximum value of $10^{23}\,\mathrm{m^{-2}s^{-1}}$, while power flux densities of the order of $3\,\mathrm{GW/m^2}$ can be reached exploiting ms laser pulse heating, simulating the effect of transient pulsed tokamak events. At CNR-ISTP in Milan, the GyM LPD is currently in operation; its layout and main features will be presented in the following Section.

1.4.1 GyM linear plasma device

The GyM linear device [20] operates at the Institute for Plasma Science and Technology of the National Research Council (CNR-ISTP, Italy) in Milan. Initially designed to investigate plasma physics aspects, such as turbulent processes, since 2014 its experimental program has expanded to include PWI experiments for magnetic fusion devices.
The GyM linear device scheme with 3D rendering and lateral view is indicated in Figure 1.2. GyM consists of a cylindrical stainless-steel vacuum chamber (AISI 304L), with a radius of 0.125 m and a length of 2.11 m. The pumping

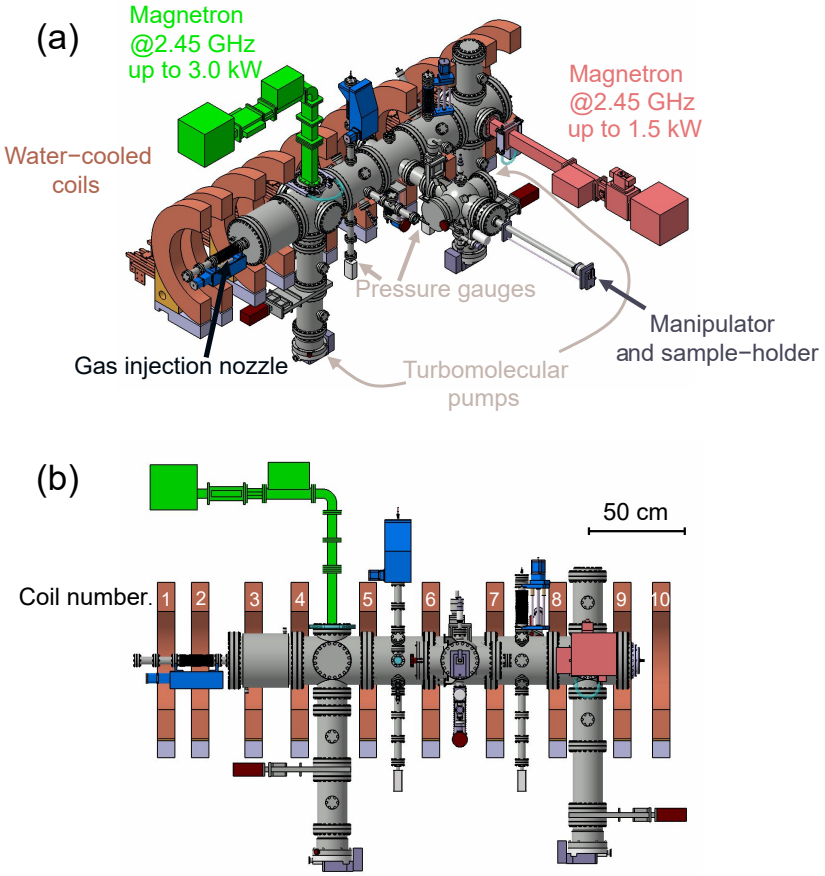

Figure 1.2: 3D schematic of the GyM linear plasma device indicating the location of ECRH sources, magnetic coils, manipulator, gas injection nozzle, pressure gauges and turbomolecular pumps (a). Lateral view of the device, highlighting magnetic coils with their assigned numbers (b).

system is composed of two turbomolecular pumps, to reach a base pressure of $5 \cdot 10^{-6}$ mbar. The vacuum chamber is segmented into 6 different sectors and surrounded by 10 identical oxygen-free copper coils connected in series, generating a maximum axial magnetic field of 0.13 T.
The device is equipped with two sample exposure systems, one of which includes a heating lamp capable of raising its temperature to 990 K, allowing the effect of wall heating to be mimicked. Both holders can be biased negatively down to -400 V, to tune the incident ion energy. The gas injection nozzle, including three mass flow controllers, is installed on the base of the vacuum vessel cylinder of sector 1; hydrogen, deuterium, helium, argon, and nitrogen can be injected inside the chamber, allowing the generation of plasmas with different compositions.
In GyM the plasma is sustained by Electron Cyclotron Resonance Heating

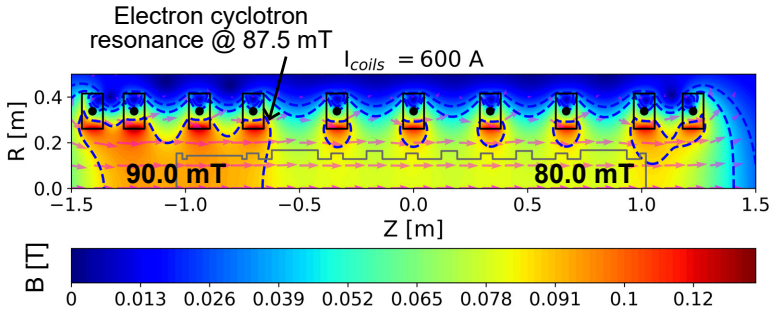

Figure 1.3: Two dimensional distribution of the magnetic field at $I_{\text{coils}} = 600\,\text{A}$. The blue dashed lines represent the resonant magnetic field value (0.0875 T) [20].

(ECRH) at the frequency of 2.45 GHz. In this heating scheme, which is also used in larger tokamaks, microwaves are injected into the chamber and absorbed resonantly by electrons when wave frequency matches their cyclotron frequency, allowing efficient energy transfer. In GyM microwaves are generated using two magnetron sources (1.5 kW and 3 kW). Since cyclotron frequency also depends on the magnetic field, the resonance is reduced to a small layer identified by the value $B = 0.0875\,\text{T}$, which in GyM is located between coils 4 and 5, as observed in the reconstructed magnetic field configuration for $I_{\text{coils}} = 600\,\text{A}$ (Figure 1.3).
A distinctive feature of the GyM plasma is its relatively large radial extension compared to the other LPDs, resulting in a plasma column that extends up to the vessel walls. In contrast, in linear devices such as PSI-2 and MAGNUM-PSI, the plasma column typically remains much narrower, with characteristic widths of about 6 mm and 10 mm, respectively.
Diagnostics on GyM include three different Langmuir Probes to reconstruct radial and axial profiles of plasma parameters. A high resolution spectrometer is used to measure radiation emitted by plasma for impurity identification and plasma state monitoring in a wavelength range $300 - 900\,\text{nm}$. In addition to this, a Quadrupole Mass Spectrometer (QMS) is connected to the device for the identification of impurities in the neutral gas (e.g. compounds of carbon, oxygen, and nitrogen). Moreover, a fast visible camera, capable of collecting images every 4 µs, is used for monitoring the plasma dynamics.
The main parameters of GyM plasma are indicated in Table 1.1. Employing a ECRH source, without the need of internal electrodes such as in arc discharge sources, the plasma generated is characterized by a low impurity content. As a drawback, the microwave source implies a theoretical limit on achievable plasma density, which in GyM is of the order of $10^{17}\,\text{m}^{-3}$. It is important to underline that the maximum Γ_i in GyM is comparable to the incident hydrogen isotope flux produced by Charge-Exchange Neutral (CXN) reaction on tokamak first walls.

Plasma parameters	**Ranges**
Electron density n_e [m^{-3}]	$\sim 1.0 \times 10^{17}$
Electron temperature T_e [eV]	≤ 15.0
Ion temperature T_i [eV]	≤ 0.1
Ion flux Γ_i [$m^{-2}s^{-1}$]	$\leq 1.0 \times 10^{21}$
Fluence* Φ [m^{-2}]	1.0×10^{25}

Table 1.1: Plasma parameters of the GyM linear device.
*Fluence after 7 hours of steady-state operation.

For this reason, assuming similar effects of ion and neutral fluxes with the same energy on materials, GyM PWI phenomena can be considered comparable to the ones happening in big tokamaks like ITER outside the divertor.

1.4.2 The upgrade: BiGyM linear plasma device

Although the GyM linear device has already demonstrated its capability to reach conditions relevant for tokamak first walls, its operational range is limited by the ECRH source. To increase device performance, an upgrade is planned within the framework of the NEFERTARI project, funded by the National Recovery and Resilience Plan (PNRR). The upgraded facility, which will be called BiGyM, is expected to start operations in 2026 and will feature some significant improvements, also from the diagnostics side.
The plasma source will be replaced by two helicon wave generators, employing a birdcage antenna geometry, with each unit working at 13.56 MHz delivering up to 10 kW of power. Helicon waves are low-frequency electromagnetic waves that can propagate in a magnetized plasma, coupling with electrons with a high efficiency, allowing the generation of denser plasma than that obtained with a conventional radio frequency source [21, 22]. With the installation of these new units, as illustrated in Figure 1.4, the goal is to extend plasma parameters up to divertor-relevant conditions for big tokamaks such as ITER. The expected plasma parameters for BiGyM are reported in Table 1.2. Mach probes, together with Langmuir probes and optical emission spectroscopy, will be employed for plasma characterization.
A new sample exposure system will be installed, equipped with a manipulator that allows axial displacement up to 1 m, full rotation of the sample holder, and tilting up to 90°. Samples can be negatively biased down to -300 V and actively heated up to 1500 K, enabling experiments under relevant thermal loads.
In addition, the diagnostics suite available on the device will be expanded. A new Optical emission Gas Analyzer (OGA) will be installed for fuel retention studies

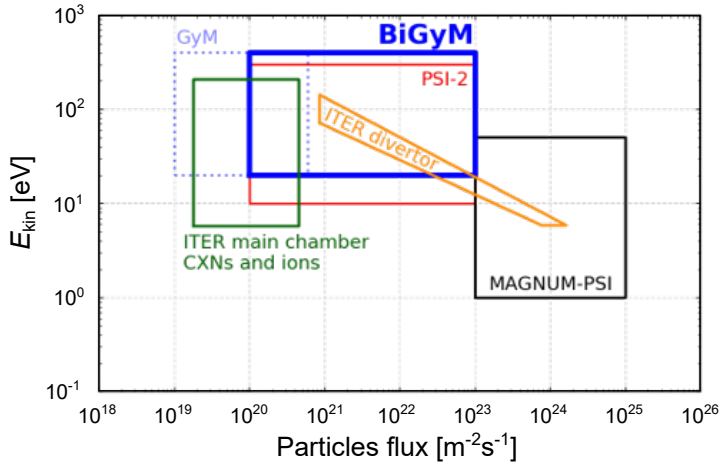

Figure 1.4: Main parameters of BiGyM compared to other linear devices and ITER divertor.

Plasma parameters	**Ranges**
Electron density n_e [m^{-3}]	$\leq 1.0 \times 10^{19}$
Electron temperature T_e [eV]	$\lesssim 6.0$
Ion temperature T_i [eV]	$\lesssim 0.1$
Ion flux Γ_i [m^{-2}s^{-1}]	$\leq 1.0 \times 10^{23}$
Fluence* Φ [m^{-2}]	1.0×10^{27}

Table 1.2: Expected parameters of the upgraded BiGyM linear device.
*Fluence after 7 hours of steady-state operation.

and an infrared camera will be employed for real-time temperature monitoring. Moreover, a picosecond high-power pulsed laser will be coupled to the linear device with an optical path to constitute an in-situ Laser-Induced Breakdown Spectroscopy (LIBS) diagnostic. This system, whose details will be explained in Chapter 3, will be used for in-situ monitoring and retention measurement of plasma-exposed samples by observing Laser-Induced Plasma (LIP) emissions with a high-resolution spectrometer.
With these new systems, BiGyM will significantly broaden the experimental capabilities of GyM, enabling PWI investigations in a wider parameter space and allowing both post-mortem and in situ monitoring of materials. The integration of LIBS in particular will provide a powerful tool for real-time surface composition and fuel retention measurements, supporting materials testing in fusion-relevant conditions.

2 Theoretical LIBS introduction and motivation of the work

With the invention of the laser, an effective method of producing coherent, monochromatic, and high-intensity light sources was introduced, enabling a wide range of applications.
One of these is the LIBS diagnostic technique, in which a high-intensity laser pulse is focused onto a sample surface to ablate a small amount of material, leading to the formation of a plasma plume. By analyzing the optical emission of this plasma and identifying the spectral features emitted by excited species (atoms, ions, or molecules), it is possible to obtain qualitative and quantitative information about the surface chemical composition and, under suitable conditions including chemometric ablation, Local Thermodynamic Equilibrium (LTE), and optical thinness of the plasma, thermodynamic properties of the plume.
A correct interpretation of the LIBS results requires a detailed understanding of laser energy deposition, plasma formation and expansion, and emission mechanisms. Moreover, studying the physics of ablation and the resulting crater characteristics is essential to determine the exact spatial resolution of the diagnostic.
This chapter provides the theoretical background of the LIBS process and the current state of research. Section 2.1 reviews fundamental theoretical concepts related to laser, LIBS architecture and layout, and physics of the plasma plume. Sections 2.2 and 2.3 present the state of the art of the LIBS applications in the nuclear fusion field and of the laser ablation modeling, which constitute an important part of this work. Finally, Section 2.4 outlines the motivations and objectives of the thesis.

2.1 Theoretical background

This section summarizes the theoretical concepts necessary for understanding the experiments and modeling activities presented in this thesis work. It is organized into six subsections. Subsection 2.1.1 introduces the basis of a laser system and the most important parameters relevant to laser-matter interaction. Subsection 2.1.2 describes the architecture of a typical LIBS diagnostic, outlining the most commonly adopted layouts. Subsection 2.1.3 gives a general introduction about time evolution of the plasma plume, analyzing the consequences of using laser with different pulse durations. Subsection 2.1.4 examines the main mechanisms leading to laser energy absorption into the target, while Subsection 2.1.5 summarizes the most relevant ablation mechanisms responsible for the formation of the ablation crater. Finally, Subsection 2.1.6 discusses the subsequent expansion stage of the plasma plume, which is the phase when the LIBS signal is collected.

2.1.1 Laser fundamentals

The operation of a laser is based on the physical phenomenon of stimulated emission, in which an incoming photon of a specific energy interacts with an excited atom, causing it to decay to a lower energy level while emitting a second photon identical in energy, phase, direction, and polarization. This process enables light amplification, with emitted radiation consequently characterized by monochromaticity, spatial and temporal coherence, high intensity, and directionality.
The laser beam is generated within an active (or gain) medium, which contains atoms capable of amplifying the initial light by stimulated emission. To achieve this, a pumping source provides energy to excite the atoms, reaching the so-called population inversion condition. A laser system is obtained by placing the active medium inside an optical cavity composed of two reflecting surfaces on opposite sides. When a photon propagates through the active medium, the emission of another identical photon can be induced by stimulated emission. Multiple reflections of the radiation between the two mirrors lead to a progressive amplification of the light intensity. If one of the two reflecting surfaces is partially transparent, a fraction of the amplified radiation can exit the cavity, forming the laser output beam.

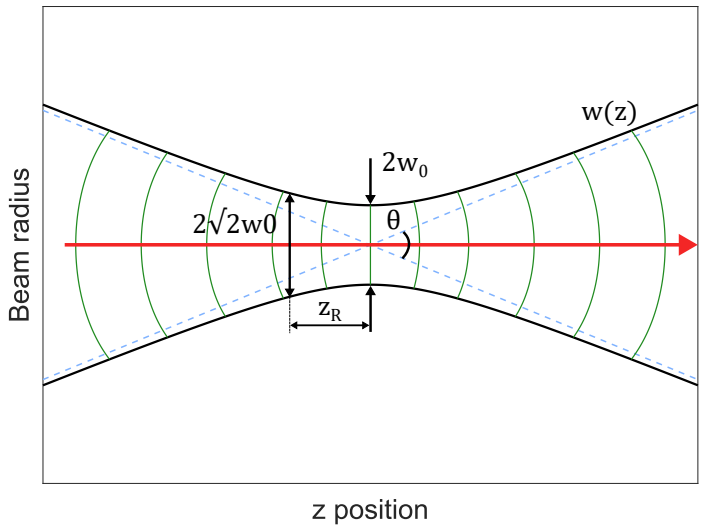

Figure 2.1: Gaussian beam propagation along the optical axis.

Gaussian beam

An important class of spatial radiation profiles that can propagate in a laser system is represented by Gaussian beams [23]. For this class of functions, the transverse intensity distribution – defined as the power delivered per unit area and proportional to the squared amplitude of the electromagnetic wave electric field – is expressed as:

$$I = I_0 \cdot \exp \frac{-2(x^2 + y^2)}{w^2} \tag{2.1}$$

where I_0 is the peak intensity, x and y are the coordinates orthogonal to the propagation axis z, and w is the spot size, defined as the radial distance where the intensity drops by a factor $1/e^2$ from its maximum value. Following this convention the laser spot diameter can be defined as $D = 2w$; in this way, a circular area of this diameter contains 86.5% of the total laser intensity.
In free space, a Gaussian laser beam is characterized by a point of minimum spot size w_0 (the beam waist) and propagates maintaining its Gaussian profile; the spot size changes as illustrated in Figure 2.1, evolving in accordance with the formula:

$$w^2(z) = w_0^2[1 + (z/z_\mathrm{R})^2] \tag{2.2}$$

where $z_\mathrm{R} = \pi w_0^2/\lambda$ is called the Rayleigh range of the beam (with λ being the wavelength of the laser). At a distance $z = z_\mathrm{R}$, the spot size is increased by a

factor $\sqrt{2}$ compared to the beam waist. In the far field approximation, identified when $z \gg z_{\mathrm{R}}$, the spot size increases linearly with the distance z:

$$w \approx \frac{\lambda z}{\pi w_0} = \theta_{\mathrm{d}} z \tag{2.3}$$

where $\theta_{\mathrm{d}} = \lambda/(\pi w_0)$ is the beam divergence, an intrinsic characteristic of the beam indicating the loss of collimation due to diffraction.
When a Gaussian beam is focused by a thin converging lens of focal length f, with the beam waist w_{0_1} located at the lens position, it is possible to show that the beam waist after the lens w_{0_2} and its position $z_{\min}$ are given by:

$$w_{0_2} = \frac{\lambda f}{\pi w_{0_1}} \cdot \left[1 + (f/z_{\mathrm{R}_1})^2\right]^{-1/2} \tag{2.4}$$

$$z_{\min} = \frac{f}{1 + (f/z_{\mathrm{R}_1})^2}; \tag{2.5}$$

under typical conditions where $z_{\mathrm{R}_1} \gg f$, these formulae simplify to:

$$w_{0_2} \approx \frac{\lambda f}{\pi w_{0_1}} \tag{2.6}$$

$$z_{\min} \approx f. \tag{2.7}$$

Thus, from Equations (2.6) and (2.7) it is clear that a planar wavefront entering a lens focuses nearly around the focal length; moreover, to reduce the focal spot, a smaller focal length or a larger incident beam waist are necessary.

Laser pulses and key parameters

An important class of lasers is represented by pulsed lasers, where the power delivered by the instrument is not constant in time but consists of individual shaped peaks, separated by a fixed time period T. The pulse temporal distribution of each pulse $P(t)$ is given in realistic cases by a Gaussian function, which can be expressed as [24]:

$$P(t) = P_0 \cdot \exp\left\{-2 \ln 2[(t - t_0)^2/\tau^2]\right\}, \tag{2.8}$$

where P_0 is the peak power in W, t_0 is the power peak time instant, and τ is the FWHM of the distribution.
Figure 2.2 shows a simple plot representing a train of some consecutive pulses. Starting from this representation, several important parameters can be defined:

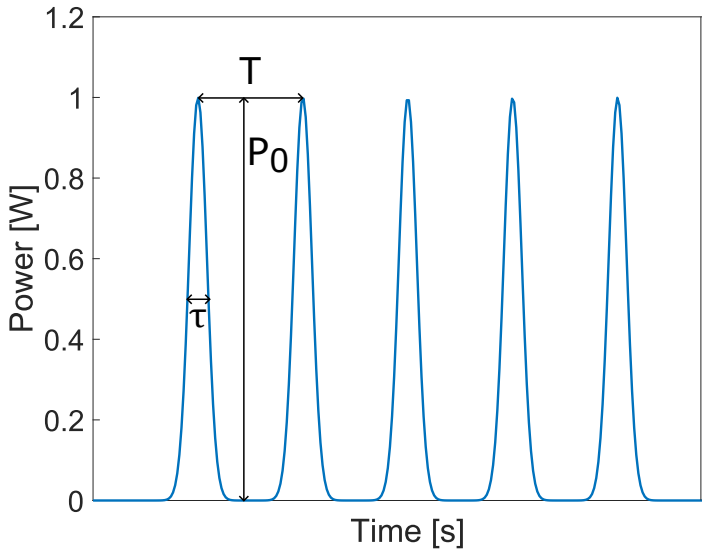

Figure 2.2: Train of 5 Gaussian pulses with peak power P_0, duration τ, separated by a period T.

- **Repetition rate**:

$$RR = \frac{1}{T} \tag{2.9}$$

  which indicates the number of pulses delivered per second. For commercial lasers typically employed for LIBS RR ranges from kHz down to 1 Hz.

- **Energy per pulse**:

$$E = \int P(t)\, dt, \tag{2.10}$$

  where the integral must be calculated choosing the proper time interval centered around the peak power function $P(t)$. The energy is related to the number of photons per pulse and their energy in a quantum description.

- **Laser fluence**:

$$F = \frac{E}{A_{\text{spot}}}, \tag{2.11}$$

  where the spot surface A_{spot} must be defined according to a convention consistent with the spatial shape of the pulse; for example, for a gaussian beam the area is typically calculated as $A_{\text{spot}} = \pi \cdot D^2/4$, where D is the beam spot diameter.

- **Intensity**:

$$I(t) = \frac{P(t)}{A_{\text{spot}}}. \tag{2.12}$$

As mentioned before, the intensity represents the instantaneous laser power delivered per unit area. A parameter sometimes used for LIBS and laser ablation modeling is the peak intensity I_0, defined as the ratio between the peak power P_0 and the spot area. To achieve high peak intensity is thus fundamental to have high-energy pulses with very short duration, focused on a small spot size.

2.1.2 LIBS: diagnostic components and different layouts

In the first phase of the LIBS technique, a high-power laser pulse is focused on the surface of a sample. The irradiated region is rapidly heated, causing the transition of the material into the gaseous phase, in a process known as laser ablation. The characteristics of this process, whose physical nature mainly depends on laser fluence, pulse duration, material properties, and focusing conditions, will be discussed in Subsection 2.1.5. When the absorbed laser energy is sufficiently high, the vaporized material becomes ionized, generating a small plasma volume referred to as the plasma plume.
Once the plasma is formed, atoms and ions within it are excited by the absorbed laser energy. As these species decay to lower energy states they emit element-specific radiation. Meanwhile, the plasma plume expands perpendicularly to the sample surface, with dynamic and shape depending on the laser parameters, the target material, and the background atmosphere.
The emitted radiation is collected typically via optical fiber and transferred to one or more spectrometers, which disperse the light into its spectral components, producing a digital spectrum visible on a computer. By identifying atomic and ionic emission lines superimposed on the continuum background, information about the elemental composition of the material and possibly plasma plume parameters can be obtained.
A complete LIBS system requires several components in addition to the laser source and the spectrometer [25]. Some mirrors and a focusing lens are necessary to guide the laser beam and focalize the spot onto the sample surface, while an additional lens or a parabolic mirror is positioned before the optical fiber to collect the plasma emission. The sample is often placed inside a measurement chamber, which allows for the control of ambient gas conditions or to operate in vacuum, in order to optimize plasma emission signal. Nevertheless, measurements can also be performed under atmospheric conditions, using a laser wavelength greater than 190 nm to avoid absorption by air. A delay generator

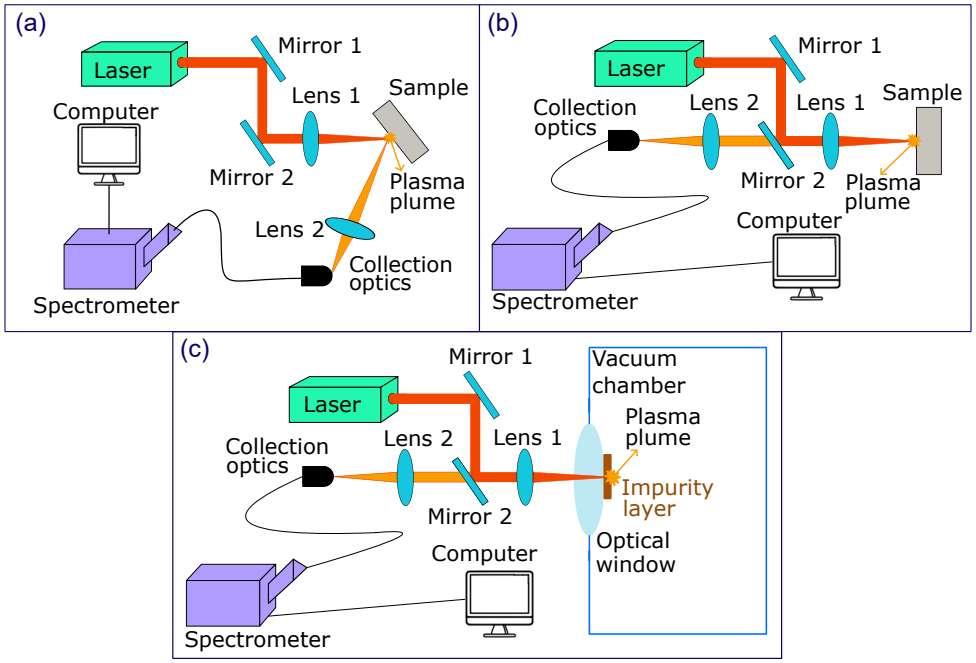

Figure 2.3: Possible LIBS setups usually adopted in experimental configurations: (a) inclined geometry, (b) collinear geometry, (c) back-collection geometry [25].

synchronized with a triggering system is typically used to adjust the delay time between the laser pulse and the spectrometer acquisition, thereby maximizing the signal-to-noise ratio. Finally, an Intensified Charge-Coupled Device (ICCD) with gating capability is often employed to enhance the plasma signal and restrict the acquisition to a precise time window.
As illustrated in Figure 2.3, the plasma emitted radiation can be collected along different Lines Of Sight (LOS). Considering that the plasma plume expands mainly perpendicularly to the surface, three main observation geometries are commonly adopted.

(1) Inclined geometry, Figure 2.3(a): the collection LOS differs from the laser incidence direction, typically forming an angle from 15° to 90°.

(2) Collinear geometry, Figure 2.3(b): the collection LOS is aligned with laser beam axis and orthogonal to the sample surface. This configuration allows to maximize the light collection and increase the observation time of the expanding plasma plume.

(3) Back-collection geometry, Figure 2.3(c): the laser beam is focused on an impurity layer deposited on the rear side of a transparent optical window. In this case, the plasma plume expands into the measuring chamber while

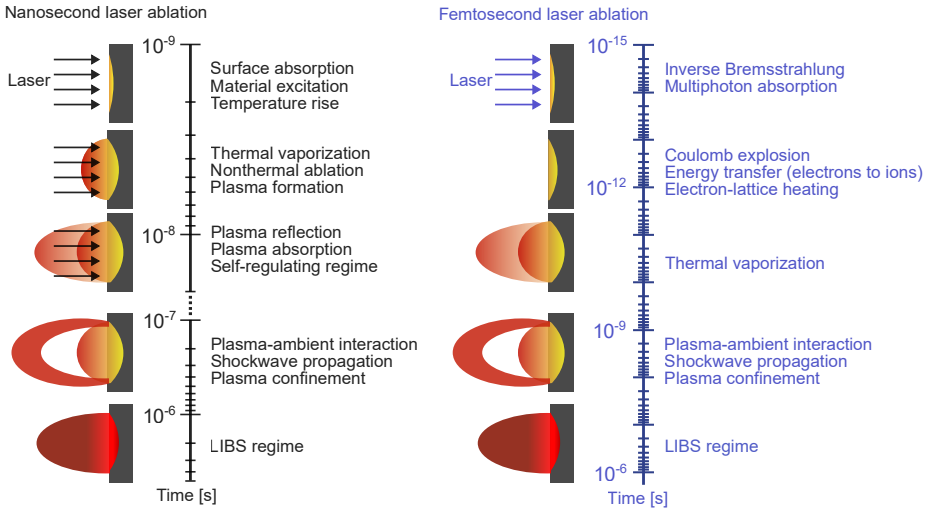

Figure 2.4: Approximate timescales for fs and ns LIBS from energy absorption to plasma plume recombination [26].

the emitted light is collected from outside. This configuration enables LIBS measurements of impurity layers without disturbing the vacuum environment.

Compared to other surface analysis techniques, such as Nuclear Reaction Analysis (NRA) and Thermal Desorption Spectroscopy (TDS), LIBS offers some intrinsic advantages. First, it allows for in-situ and standalone measurements, without requiring sample pretreatment. Moreover, LIBS can operate in harsh environments, including vacuum conditions and high magnetic fields, and it can be combined with other laser-based cleaning techniques or complementary diagnostics. These features make LIBS particularly suitable for the monitoring and chemical characterization of PFCs in tokamaks and LPDs.

2.1.3 Plasma plume temporal evolution

When a focused laser beam with fluence F deposits energy onto a surface, a plasma plume is generated through a sequence of processes spanning from the fs to the ms time scale. The physics of ablation, plasma generation and plume expansion strongly depends on the background atmosphere and the initial conditions of laser-matter interaction; in this context, one of the most important parameters is the laser pulse duration τ.
Figure 2.4 schematically illustrates the temporal evolution of the plasma plume, highlighting the main characteristic phenomena for two limiting regimes: femtosecond and nanosecond pulse duration.

Considering a conductive material at the beginning of laser-matter interaction, laser radiation is first coupled to the electron subsystem. The main difference between the different pulse duration regimes arises from the comparison of τ with the electron-phonon relaxation time (τ_{e-i}) of the system, which is typically of the order of several ps.
When $\tau \gg \tau_{e-i}$ as in the ns regime, the laser energy is transmitted to the lattice without delay. In this case, processes such as ionization, lattice heating, and vaporization occur while the pulse is still incident [27]. Moreover, the plasma plume is generated during the pulse and a significant fraction of laser energy is absorbed by the plasma, which becomes hotter.
In contrast, for a fs pulse, $\tau < \tau_{e-i}$ and so a strong non-equilibrium state is generated: electrons are heated almost instantaneously, while ionic lattice remains comparatively cold. As a consequence, thermal diffusion is effectively frozen during the laser-material interaction, resulting in reduced thermal damage and a limited Heat-Affected Zone (HAZ) [27]. In this regime, the laser pulse ends before the plasma plume, originating from the vaporized target material, can form and expand significantly. Consequently, the plasma does not appreciably absorb the incoming laser energy and is characterized by a lower temperature and a reduced continuum emission, with spectra dominated by neutral atomic lines [27].
In this context, the ps pulse regime behaves similarly to the fs one: since $\tau \sim \tau_{e-i}$, the heat transfer to the lattice is slightly delayed and heat conduction into the bulk material is reduced, generating a HAZ with dimensions between those observed in the ns and fs regime. In this case, the plasma plume appears several hundreds of ps after the laser pulse incidence [28], and only a weak plasma shielding effect due to air breakdown may occur, with an absorption up to $\sim 10\%$ of the incident energy [27].
The different physics of laser-matter interaction is also reflected in the characteristic ablation mechanisms. While for long pulse durations the ablation is mainly driven by thermal processes such as melting and vaporization, for very short pulse regimes non-thermal mechanisms, such as Coulomb explosion (discussed in Subsection 2.1.5) can become dominant.
These differences in the heat transport dynamics also influence the crater morphology: longer pulses produce craters showing irregularities because of melting, re-solidification, and splashing of liquid droplets, whereas shorter pulses result in craters characterized by cleaner shapes with well-defined edges because of minimization of thermal damage. The latter aspect is beneficial for LIBS measurements, as it ensures better spatial resolution and a cleaner signal.
The pulse duration also affects the expansion phase of the plasma plume. For

shorter pulse duration regimes, the plume is typically characterized by a hemispherical shape, with expansion dynamics influenced by the initial conditions: larger spot sizes lead to a sharper plume shape, caused by ion accelerated from the laser-plasma interaction [26]. In contrast, shorter pulse ablation typically produces narrower and more directional plumes, with expansion highly oriented in the direction normal to the target surface [29].
Finally, it is important to underline that the plasma lifetime depends on the pulse duration. Plasma induced by fs pulses typically persists for a few us on average, while in the ns regime, due to the higher amount of energy absorbed by the plume, plasma can last up to several tens of us before complete recombination [30].

2.1.4 Laser energy absorption mechanisms

Laser energy absorption represents the first step of the LIBS diagnostics process and strongly depends on laser parameters, material properties, and plasma conditions. For conductive materials, when a laser pulse impinges on a solid surface, the initial interaction stage involves the free electron subsystem.
For laser pulses of ns duration, typically characterized by peak intensities of the order of $I \sim 10^9 - 10^{11}\,\mathrm{W/cm^2}$, the incident electromagnetic energy is initially absorbed within the optical skin depth of the target. Under these conditions, rapid electron-phonon coupling leads to lattice heating and material removal driven by thermal processes. Once a plasma plume is generated, a significant fraction of laser energy can be further absorbed by the plasma itself through collisional processes, mainly inverse bremsstrahlung and photoionization.
In the case of ultra-short pulses (from tens of ps down to fs regime), energy deposition occurs on timescales comparable or shorter than τ_{e-i}, leading to a non-equilibrium heating phase. When the intensity becomes sufficiently high ($I \gtrsim 10^{12}\,\mathrm{W/cm^2}$), the interaction of the laser pulse with a transient pre-plasma, generated by the weak intensity leading edge of the pulse, can become relevant. In this regime, collisional absorption processes are important at moderate intensities ($10^{12}\,\mathrm{W/cm^2} \leq I \leq 10^{14}\,\mathrm{W/cm^2}$), while at higher intensities ($I > 10^{14}\,\mathrm{W/cm^2}$), non-collisional processes such as resonance absorption can play an important role [31].

Skin-depth absorption

When an electromagnetic wave hits a material surface, a fraction of its energy is reflected because of the abrupt change of refractive index at the interface. The ratio of reflected to incident power is quantified by the complex refractive index

of the medium, which determines the surface reflectivity R; this quantity depends on wavelength, polarization, angle of incidence, and temperature. Under standard light incidence conditions R can be calculated using Fresnel equations; however, during laser ablation, the rapid variation of temperature and the transient surface deformation complicate the use of simple analytical expressions. For this reason, the application of semi-empirical relations or experimental data is often preferred.
Before plasma formation, the incident wave penetrates a certain distance into the material, where its energy is deposited and converted into electronic and thermal energy. The penetration distance is quantified by the optical skin depth δ:

$$\delta = 1/\alpha = \lambda/4\pi\kappa, \tag{2.13}$$

where α is the absorption coefficient [m^{-1}], while κ is the extinction coefficient, i.e. the imaginary part of the complex refractive index [32]; δ represents the distance after which the intensity of the EM wave is reduced by a factor e. The extinction coefficient strongly depends on wavelength of incident radiation and on the nature of the material (whether it is a conductor, semiconductor, or dielectric), since different physical processes govern the absorption. For metals, considering an incident laser beam with $\lambda \sim 1\,\mu$m, the skin depth is of the order of some tens of nm.

Inverse bremsstrahlung

Bremsstrahlung is the emission of radiation by charged particles when there is a change of momentum caused by a Coulomb collision with other charged particles. Inverse Bremsstrahlung (IB) represents the reverse phenomenon: it is a three-body interaction where an electron absorbs a photon while simultaneously interacting with the electric field of another particle, mainly ions or atoms [33]. This process is considered the dominant plasma-laser absorption mechanism for long (ns) pulses, but it can also play a significant role for shorter pulses at moderate intensities.
The cross section for photon absorption by free electrons in the field of neutral atoms is typically $1-2$ orders of magnitude lower than in the field of ions; however, the former is dominant at low ionization degrees of plasma plume, while the latter prevails when ionization degree is approaching a unitary value. For photon absorption by electrons in the ion field, the IB coefficient can be expressed as [34]:

$$\alpha_{\mathrm{BI}}[cm^{-1}] \simeq C_{\mathrm{BI}} \frac{Z^2 n_i n_e \lambda^3}{T_{\mathrm{p}}^{1/2}} \left[1 - \exp\left(-\frac{\hbar\omega}{k_{\mathrm{B}} T_{\mathrm{p}}}\right)\right], \tag{2.14}$$

where C_{BI} is a proportionality constant, Z the average ionic charge, n_e and n_i the electron and ion densities expressed in cm^{-3}, k_{B} the Boltzmann constant in eV/K, T_{p} the plasma temperature in K, and λ the wavelength in nm.
Equation (2.14) shows that IB becomes more important for longer λ, being particularly effective for infrared lasers.

Photoionization

At intermediate ionization degrees (typically between 10^{-2} and 0.3) the plume contains a lot of excited molecules and atoms represented by n_a^*, with $n_a^* \gg n_e, n_i$. In this regime photoionization, the direct photon absorption with consequently bound electron release, becomes a relevant absorption channel.
Since the process requires photon energies comparable or greater to the ionization potential, this process is efficient for short λ radiation, for example when using UV laser. The excess photon energy above the electron binding energy is transferred to free electrons as kinetic energy.
For hydrogen-like atoms, in the hypothesis of photon energy $\hbar\omega$ lower than the ionization energy E_{ion}, the absorption coefficient can be described by the Kramers-Unsöld equation [34]:

$$\alpha_{\mathrm{KU}} \simeq C_{\mathrm{KU}} \cdot p \cdot \lambda^3 \left[exp\left(\frac{\hbar\omega}{k_{\mathrm{B}} T_{\mathrm{p}}} \right) - 1 \right] \cdot \exp\left(-\frac{E_{\mathrm{ion}}}{k_{\mathrm{B}} T_{\mathrm{p}}} \right) \tag{2.15}$$

where $C_{\mathrm{KU}} = 2.43 \cdot 10^{16}$, p is the plasma plume pressure expressed in Pa and λ is expressed in nm. The absorption coefficient α_{KU} becomes important in the UV range, where photon energy is higher than the plasma thermal energy, and for moderate laser intensities [35].

Resonance absorption

When an electromagnetic wave impinges perpendicularly on a plasma region with a density gradient, the wave can propagate into the low density region until n reaches a certain value, called the critical density n_{c}, which can be expressed in SI units as:

$$n_{\mathrm{c}} = \frac{\epsilon_0 m_e \omega^2}{e^2}, \tag{2.16}$$

where ϵ_0 is the vacuum permittivity, m_e the electron mass, e the unitary electric charge, and ω the angular frequency of the wave. When the wave encounters an overdense state it is reflected and the propagation through it is forbidden.
For p-polarized light waves, where the electric field lies in the same plane of the

incident wave vector and the surface normal, the situation is different. Assuming a density gradient perpendicular to the surface, the electric field component parallel to ∇n can drive charge density fluctuations which can be resonantly enhanced by the plasma. When the local plasma frequency equals the laser frequency, these oscillations are resonantly enhanced with efficient energy transfer from the wave to the plasma.
In a simplified model, considering a plasma slab of thickness L with a linear density profile $n = n_c \cdot z/L$, the absorbed fraction of the incident energy depends on the incident angle θ approximately as $(\omega L/c)^{2/3} \cdot \sin^2\theta$, with a maximum at a characteristic angle $\theta_{\max}$ [36].

2.1.5 Laser ablation mechanisms

Laser ablation is the process consisting of the material removal from a solid surface caused by the energy deposited by a high-power laser pulse. Ablation is a threshold process, which occurs only when the fluence overcomes a minimum value, known as the fluence threshold F_{th}, which depends on the pulse duration regime, the wavelength, and the material thermophysical properties.
The ablation process can be dominated by different physical mechanisms depending on the laser parameters, material properties, and focusing conditions; the latter determine both the incident fluence and the subsequent evolution of the plasma plume. In this section, the three most relevant mechanisms are discussed: normal evaporation and phase explosion, characterized by thermal origin, and Coulomb explosion, which is an electrostatic mechanism. These three processes are not mutually exclusive and may coexist or occur sequentially during a single laser pulse [37].

Normal evaporation

Normal evaporation is the most intuitive ablation mechanism, representing a thermally activated surface process. This regime typically dominates at relatively low laser fluences, up to several tens of J/cm^2, and for longer pulse durations (from ns regime upward), when heat diffusion allows the system to remain below the thermodynamic critical point [38].
In principle, this process occurs at any temperature and becomes significant as the surface is heated toward the boiling point, while remaining below the thermodynamic critical point. Normal evaporation is driven by the shifting towards higher velocities of the Maxwellian distribution of particles, caused by a temperature increase. Particles for which thermal energy overcomes the binding

potential are emitted from the surface, and a non-equilibrium state is generated when the evaporation rate is higher than the condensation rate.
The evaporation rate can be described using the Hertz-Knudsen equation, which relates the particle flux J to the equilibrium saturation pressure $p_{\mathrm{sat}}(T)$ at the surface temperature T:

$$J = \alpha \frac{p_{\mathrm{sat}}(T)}{\sqrt{2\pi m k_{\mathrm{B}} T}}, \tag{2.17}$$

where α is the evaporation coefficient and m the particle mass. The strong T dependence arises from the saturation pressure, which can be expressed using the Clausius-Clapeyron relation:

$$p_{\mathrm{sat}}(T) = p_{\mathrm{atm}} \cdot \exp\left[\frac{m L_v}{k_{\mathrm{B}}}\left(\frac{1}{T_v} - \frac{1}{T}\right)\right], \tag{2.18}$$

where p_{atm} is the atmospheric pressure and L_v is the enthalpy of vaporization. From this relation, it becomes evident that the evaporation flux increases exponentially with surface temperature.

Phase explosion

Above a critical fluence threshold, which depends on material properties and irradiation conditions, the rapid energy deposition drives the surface into a superheated metastable liquid state, approaching the limit of thermodynamic stability. When the temperature tends toward the value of $0.9 \cdot T_{\mathrm{crit}}$ (where T_{crit} is the thermodynamic critical temperature), the homogeneous nucleation rate increases by several orders of magnitude in a very small temperature interval, leading to the formation of multiple growing vapor bubbles inside the liquid. This situation generates an environment characterized by an explosive liquid-vapor transition, known as phase explosion [38].
This phenomenon becomes the dominant ablation mechanism for ns pulses at fluences exceeding several tens of J/cm^2, while for ps pulses it can occur at significantly lower fluences, of the order of 10 J/cm^2, due to the higher peak intensity.
Phase explosion differs from normal evaporation as it is a volumetric process, in which a mixture of vapor, droplets, and clusters are emitted from the target on a very short timescale. This mechanism also produces strong surface morphology modifications inside and around the ablation crater. Experimentally, phase explosion is often associated with an abrupt increase in ablation rate, delayed ejection of liquid and droplets, nanoparticle formation in the plume, and rough or porous morphologies of the ablation crater surface.

Coulomb explosion

Coulomb explosion is a non-thermal ablation mechanism of electrostatic origin, associated with ultrashort pulses (typically to the fs regime), and is often reported to be relevant for dielectrics and semiconductors rather than metals. The process is typically considered a gentle ablation mechanism, becoming dominant at low fluence values just above the ablation threshold, often in the range of fractions of J/cm^2 [39].
In Coulomb explosion, the very high laser intensity causes direct electron ejection, creating a charge separation between the positively charged surface and the electron cloud; the resulting electric field pulls ions out of the surface, causing the removal of some layers of material. In this case, ablation occurs without the need for thermal diffusion in the lattice, resulting in a cleaner ablation geometry with respect to thermal processes.

2.1.6 Plume expansion and emission

After breakdown, the laser-induced plasma plume detaches from the surface, beginning an expansion phase whose dynamical evolution is determined by its initial thermodynamic state and by the ambient gas conditions. This stage occupies a significant fraction of the plume lifetime, ranging from ns to us.
In the proximity of the target, the ablated species are generally emitted with a non-equilibrium velocity distribution; the distance over which the particle velocity distribution thermalizes is called the Knudsen layer [40]. This region is characterized by steep temperature and pressure gradients, particularly large in the direction orthogonal to the surface, which gives a strong directionality to the plasma plume expansion. Two different regimes can be identified, depending on the density of emitted material [34].

1. When the density of the ablated species is low, typically below 0.5 Mono-Layers (ML) within a few tens of ns ($F \sim$ ablation threshold of the material), particles travel away from the surface without collisions, maintaining the characteristic energy distribution of the ejection mechanism. This distribution is typically non-Maxwellian, especially for short and high-power density pulses, when non-equilibrium effects are important.

   When the emitted particle density becomes high enough for each atom to collide at least three times within the Knudsen layer, the velocity distribution relaxes to a Maxwellian form in the center-of-mass frame, characterized by a flow velocity:

$$u_{\mathrm{Kn}} = \sqrt{\frac{\gamma k_{\mathrm{B}} T_{\mathrm{Kn}}}{m}} \tag{2.19}$$

and a $\cos^4(\theta)$ angular flux distribution, where the subscript Kn indicates quantities referred to the Knudsen layer, $\gamma = c_p/c_v$ is the adiabatic constant of ablated species, and m is the particle mass. Beyond the Knudsen layer, the plume can be described as a free-expanding gas with a constant flow velocity.

2. When the emitted particle density exceeds approximately the one corresponding to ablation of 1 ML in 20 ns, the plume undergoes a non-stationary adiabatic expansion outside the Knudsen layer. In this case, the temperature decreases while the flow velocity increases as the plume expands. Beyond the Knudsen layer particles are characterized by a Maxwellian distribution in the center-of-mass frame, moving again with flow velocity u_{Kn}. The Knudsen layer thickness t_{Kn} can be estimated from Monte Carlo simulations and as a first approximation depends primarily on the mean free path λ_l of the ablated species:

$$t_{\mathrm{Kn}} \simeq 19\lambda_l = 19 \cdot 2^{-1/2}(n_{\mathrm{abl}}\sigma)^{-1} \tag{2.20}$$

where n_{abl} is the number density of ablated species and σ their collision cross section. The particles flow velocity within the Knudsen layer is subsonic but becomes supersonic outside it. After the adiabatic stage, the plume enters a free-flight expansion regime characterized by a constant flow velocity.

These processes are schematically illustrated in Figure 2.5.
In the high emitted particle density regime (case 2), the expansion beyond the Knudsen layer can be described as a non-stationary adiabatic process described by gas-dynamic equations. Under vacuum conditions, experimental observations indicate that the expansion is primarily driven by the initial dimensions of the plume, resulting in a strongly directional flow with the maximum velocity oriented along the surface normal. As a consequence, the plume presents an elongated shape extending away from the target surface. After the adiabatic expansion stage, the plume eventually enters a collisionless free-flight regime, in which the flow velocity remains constant and the velocity distribution remains frozen.
In many LIBS experiments external gas is intentionally injected into the measuring chamber to enhance spectral intensity and plasma persistence. When the expanding plasma moves at supersonic speed it compresses the surrounding gas, inducing a series of processes such as plasma deceleration, shockwave formation, and infiltration of gas molecules into the plume [41]. The gas species can have an influence on the spectral signal because of different absorption

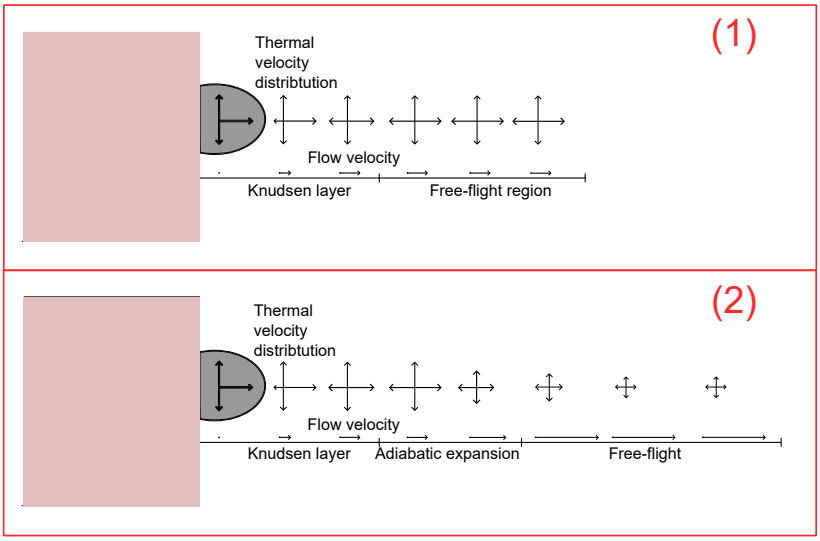

Figure 2.5: Illustration of plume flow velocity and Maxwellian velocity evolution in the different expansion regions for low ablated particle density (1) and high ablated particle density (2) [34].

characteristics with respect to plasma radiation. Moreover, the difference in thermal conductivities implies that axial plasma expansion rate tends to reduce for heavier gases.

The ambient pressure also plays an important role. At low pressures, the plume presents more splitting and sharpening phenomena, with a delay in the transition from linear expansion phase to subsequent plasma deceleration. As pressure increases, the plasma becomes more confined and the transition to deceleration phase occurs earlier. As a consequence, both temporal and spatial evolution of LIBS emission are strongly influenced by the background atmosphere composition and pressure.

During the expansion phase, the laser-induced plasma plume emits electromagnetic radiation over a broad wavelength range, as a consequence of relaxation processes from excited species and continuous interactions between charged particles.

At the early evolution stage, when electron density and temperatures are still high, emission is dominated by continuum radiation, mainly caused by Bremsstrahlung radiation from free-free and free-bound transitions. As the plume expands becoming colder, continuum radiation decreases and discrete spectral lines, originating from electronic transitions of excited neutral atoms and ions, become visible. This part of the spectrum is the most significant, since it contains element-specific information. It is important to underline that depending on the mass of the species inside the plume, spectral emission line can become more

intense for different times during the plume evolution. Finally, at later stages, molecular emission bands caused by molecular recombination and molecular formation process may also be observed.

2.2 State of the art of LIBS in nuclear fusion

LIBS in recent years has emerged as a versatile analytical tool for the characterization and monitoring of PFCs under conditions relevant to magnetic confinement fusion. Thanks to its rapid response, contactless operation, capability for remote analysis, and the robustness in harsh environments, it is considered a strong candidate for live monitoring of first walls and divertor components in large magnetic fusion devices, for example during maintenance phases.
One of the fundamental capabilities of LIBS is elemental identification, which relies on the fact that every element (and its ionization states) emits characteristic spectral lines associated with electronic transitions. By comparing a LIBS spectrum with a database where spectral lines and statistical parameters of each element are contained (such as NIST), the elemental components of the analyzed surface can be identified. Beyond this qualitative analysis, an analytical technique, called Calibration-Free LIBS (CF-LIBS), has been developed to obtain quantitative information on elemental compositions without using calibration curves [42].
CF-LIBS can be applied only assuming chemometric ablation, an optically thin plasma (i.e. not influenced by self-absorption), and Local Thermodynamic Equilibrium (LTE) condition in the actual spatial and temporal observation window [43]. Even if these hypotheses are quite restrictive, this technique has been successfully applied in fusion-relevant studies. For example, Marín Roldán et al. [44] adopted CF-LIBS to quantify the elemental composition of W-based material (specifically, the binary alloy W70Cu30) using both ns and ps laser. The nominal composition given by manufacturer has been retrieved successfully, showing also that LIBS quantification was more precise for the ps laser. CF-LIBS technique can also be used to quantify H/D content in exposed PFCs, as done for example by Veis et al. [45]; in the mentioned work, D concentration percentage in Be/W mixed homogeneous coating has been successfully evaluated, with the results obtained in good agreement with TDS measurements and a depth profile similar to the one recorded using Secondary Ion Mass Spectroscopy (SIMS).
As a second investigation method LIBS can be used for depth profile analysis, recording LIBS spectra for a successive number of laser pulses in the same point; in this way, looking at the intensity variation for a particular element reveals the layer-by-layer composition of the sample. This technique was applied for

example by Mercadier et al. [46] to measure multilayered ITER-like samples, previously calibrated using the Glow Discharge Optical Emission Spectroscopy (GD-OES) diagnostic, employing different wavelengths (different harmonics of Nd:YAG laser) of a ns laser. The results obtained by LIBS showed a good agreement with GD-OES, obtaining the most accurate measurement with a top hat-shaped laser distribution and using the third harmonic ($\lambda = 355\,\text{nm}$); however, a mixing of different layers was observed because of melting, suggesting the use of a very low fluence or the reduction of the laser pulse duration.
LIBS in fusion research can also be used as a complementary post-mortem technique for the validation of other atomic spectroscopy diagnostics, such as TDS, NRA, or Laser-Induced Ablation Quadrupole Mass Spectroscopy (LIA-QMS) [47]. The advantage of LIBS as a local measurement with a tunable depth resolution can be exploited to overcome limitations of other techniques.
Thanks to its versatility and the different possibilities of characterization methods, LIBS has been implemented on different fusion facilities, ranging from large tokamaks to linear plasma devices and laboratory environments. Its applications include fuel-retention studies, erosion-deposition monitoring, and composition analysis of first wall materials. A LIBS system is installed, for example, in the EAST tokamak (Hefei, China) [48], where it was applied as a routine method to analyze the composition of PFCs.
Since direct LIBS measurements during tokamak operations are not always possible, other configurations are currently under investigation to enable remote measurement after shutdown. For instance, Almaviva et al. [49] used a system based on a robotic arm integrating a laser source and optical components, which was used to perform LIBS measurements in different positions of the first wall in the Frascati Tokamak Upgrade (FTU, Rome, Italy) after the end of the 2019 experimental campaign. A similar system, exploiting the remotely controlled MASCOT robotic arm [50, 51], was employed in 2024 inside the JET tokamak to measure T retention on the first wall after the last D-T experimental campaign concluded in 2023.
As mentioned in Section 1.4, LPDs provide a controlled and more accessible environment, often entirely dedicated to PWI experiments. Unlike tokamaks, these facilities offer direct optical access to the target region through optical windows directly mounted on the vacuum vessel or on the exposure chamber. This feature makes LPDs ideal testbeds for in-situ LIBS development.
A first LIBS system on the PSI-2 device was designed by Jiang et al. [52] in 2017. The setup included a Nd:YAG laser with a pulse duration $\tau = 6\,\text{ns}$ and the possibility to operate at four possible wavelengths, connected to the linear device through a 30 m optical path. The diagnostic was used for example to study the

temporal evolution of the D signal shortly after plasma exposure, analyzing the concentration decrease caused by outgassing. The LIBS system was upgraded in 2019 by Jiang et al. [53] introducing a new set of optical units and a dual spectrometer configuration, with one spectrometer optimized for the blue and the other for the red spectral range.
A LIBS system was also integrated on the PISCES-A facility (UC San Diego, US), using a Nd:YAG laser with $\tau = 5\,\text{ns}$ [52]. In 2021 the system was further upgraded [54] by introducing a motorized mirror positioned just before the entrance optical window, allowing faster data acquisition and improved control of the laser spot position on the target surface.
The quantification of hydrogen isotopes retained in fusion-relevant materials represents one of the most crucial applications of LIBS, since future tokamaks such as ITER will be subject to strict limits on the maximum allowable tritium inventory (1 kg in the entire reactor is the current ITER limit [55]). In this context, LIBS enables in-situ and remote detection of hydrogen isotopes. As early as 2011, LIBS was demonstrated to provide reliable results in the detection of a small amount of hydrogen in fusion-relevant samples [56]. Quantitative measurements in this context can be achieved by means of CF-LIBS approach, as demonstrated for example by Veis et al. [45].
In-situ measurements of fuel content in LPDs have also been successfully performed, as shown by Nishijima et al. [54] on the PISCES-A facility. Measurements aimed at determining short term D retention and its concentration evolution during and after plasma exposure were also carried out in-situ by Jiang et al. [57] on the PSI-2 linear device. This experiment successfully detected the presence of fuel during plasma operation, demonstrating the suitability of LIBS for signal detection in harsh experimental conditions.

2.3 State of the art of laser ablation modeling

The physical phenomena leading to laser ablation represent a fundamental stage in the overall LIBS process. The ablation crater shape and depth give information about the spatial distribution of detected elements, determining also the achievable resolution. In addition, heat diffusion through the surface can affect the LIBS signal by causing thermal diffusion of atoms from the material bulk or by producing melted layers with successive ejection of liquid droplets. For these reasons, laser ablation modeling is a useful tool to understand and predict the effect of laser-material interaction, the temporal evolution of heat transport, and the resulting ablation crater morphology.
When a high-intensity EM wave strikes a solid target, the incident energy is first

absorbed by free electrons and subsequently transferred to the atomic lattice through electron-phonon coupling. The characteristic electron-phonon relaxation time reaches a maximum value of ~ 100 ps; therefore, when the laser pulse duration is in the ns regime the two subsystems can be considered in thermal equilibrium, and heat transport can be described by the classical Fourier heat conduction equation. This approach was used, for instance, by Sinha [58] to model laser ablation of thoria (ThO_2), a ceramic oxide material relevant for fission fuel applications. A two-dimensional finite-difference model was developed coupling the heat conduction equation with the Lambert-Beer law to account for finite optical penetration and including latent heat consumption to model phase transitions. Material removal was assumed to occur when the surface temperature exceeded the boiling point, with a vaporization velocity estimated from the Hertz-Knudsen law, so assuming Maxwellian velocity distribution of particles. Sinha [59, 60] subsequently extended the model by incorporating plasma plume shielding and introducing temperature-dependent thermophysical properties, applying the same methodology to other ceramic materials (yttria and alumina). With the upgraded model an improved description of the experimental behavior was obtained.

A similar single-temperature framework was applied by Tao et al. [61], who developed a one-dimensional COMSOL model for ns laser ablation of silicon. Material removal was simulated by a moving boundary with velocity determined by Hertz-Knudsen equation. This approach was extended to a two-dimensional finite-element model by Deng et al. [62], to simulate ns laser ablation of SiC using different laser λ. The results reproduced well the melting threshold fluence showing its increase with λ. Comparable techniques were also used for metals: for example Li et al. [63] modeled ns laser removal of epoxy resin paint film on Al, introducing a material removal mechanism based on thermal stress stripping due to the presence of a surface layer.

When pulse duration decreases to ps and fs timescales, it becomes comparable or shorter than the electron-phonon relaxation time, and the assumption of instantaneous thermal equilibrium no longer holds. In this situation two heat conduction equations are necessary to describe energy absorption by electron population and its transfer to the lattice. This process is therefore described by the Two-Temperature Model (TTM) consisting of two coupled differential equations for electron and lattice temperatures.

COMSOL Multiphysics was used by Wang et al. [64] to develop a two-dimensional TTM for ps laser ablation of stainless steel. Material removal was approached considering the phase-explosion mechanism handled through the deformed geometry module; instantaneous material removal was triggered when the lattice

temperature overcame the critical threshold $0.9 \cdot T_{\text{crit}}$ (T_{crit} being the thermodynamic critical temperature) assuming a mesh deformation velocity equal to the speed of sound in solid. Results showed an approximately linear increase of ablation depth and diameter with the increasing of laser fluence, with general trends very similar to experimental cases.
Subsequent studies have proposed alternative formulations for the ablation criterion. Peng et al. [65] applied a similar TTM for ps and fs laser ablation of stainless steel and Ti_6Al_4V but computing recession velocity from an energy balance at the surface, allowing for sub- and supersonic propagation. The model also introduces separate temperature thresholds for electron and lattice populations, to capture non-equilibrium material removal mechanisms such as spallation and Coulomb explosion. Chen et al. [66] developed a model for fs laser ablation of silicon, identifying the computational ablation surface as the isotherm most similar to the experimental crater profile.
In summary, laser ablation modeling spans from single temperature Fourier-conduction models, suitable for longer pulses, to two-temperature models to capture non-equilibrium effects between electron and lattice subsystems when dealing with ultrashort pulses. Incorporating phase-change dynamics, temperature-dependent properties, and plasma shielding effects refine the model improving the agreement with experimental results. In the present work both ns and ps ablation regimes have been investigated and numerical models have been developed to describe temperature field evolution, energy absorption, and mass removal. Such modeling work can also provide support for the interpretation of LIBS measurements, offering predictive insight about spatial extension of thermal effects and single-pulse ablation crater shape.

2.4 Thesis layout and objectives

The Ph.D project presented in this thesis was carried out within the framework of the PNRR NEFERTARI Project, which aims to enhance the diagnostic capabilities and performance of the RFX-mod2 fusion device in Padova and of the CNR-ISTP facilities in Bari and Milan. The latter was identified as the main location where this work was developed.
The first objective of the project was a conceptual and feasibility study for the development and installation of a LIBS diagnostics on the BiGyM LPD. The selection of suitable components was based on a critical analysis of different LIBS results reported in the literature, combined with some sensitivity analyses aimed at assessing the impact of laser parameters on the diagnostics performance. On the basis of laboratory constraints and the BiGyM layout, a preliminary

conceptual design of the optical path connecting the laser source to the LPD was completed. The outcomes of this activity, together with the specifications of the selected components, are presented in Chapter 3.
The second objective of the thesis concerned the numerical modeling of the laser ablation process using the Finite Element (FE) code COMSOL Multiphysics. The activity focuses on the simulation of laser energy deposition, temperature evolution, and material removal. The modeling was conceived as a support tool for diagnostic applications, allowing the prediction of single-pulse ablation crater characteristics, which define the space resolution of LIBS measurements and are particularly important for retention and depth profile studies. Moreover, by computing the temperature field and its temporal evolution inside the sample, the model allows an evaluation of the extension of thermal effects during the LIBS process, representing the so-called heat-affected zone. This activity was divided into two main parts:

(i) The first part, described in Chapter 4, addresses ns laser ablation modeling, which is currently the most widely adopted approach in fusion-related LIBS experiments. The model solves the Fourier heat conduction equation with temperature-dependent thermophysical properties and includes phase change effects through latent heat consumption. The model was initially validated by comparing the temperature field and its temporal evolution against results of other numerical models available in literature (Section 4.1). Successively, an experimental campaign was performed at the CNR-ISTP Bari laboratories, where silicon and tungsten samples were ablated in low-pressure conditions using a ns laser. The generated ablation craters were examined by different surface analysis techniques to provide experimental data for model validation. The description of the experimental campaign and the validation results, including the implementation of a correction term to account for plasma shielding effects, are discussed in Section 4.2.

(ii) The second part of the modeling work, described in Chapter 5, focuses on ps laser ablation, developed to more closely reproduce the operating conditions of the LIBS diagnostics that will be implemented on BiGyM. In this case, the model employs a two-temperature approach to describe the energy transfer between the electron and lattice subsystems during and after pulse irradiation and the successive material removal. After a first validation phase comparing the temperature field evolution against reference literature results (discussed in Section 5.1) another experimental campaign was carried out at the CNR-ISTP Bari laboratories to obtain data about ps laser ablation craters. The experiments description and

the results of this further validation step are presented in Section 5.2. This activity allowed to explore different modeling approaches through a direct comparison between ns and ps regimes, highlighting the differences in the ablation dynamics.

The final part of this thesis, described in Chapter 6, is dedicated to an experimental in-situ LIBS campaign carried out on the PSI-2 LPD performed during a visiting period at FZJ Jülich (February-May 2025). In this experiment, in-situ LIBS measurements were performed on tungsten (W) and tantalum (Ta) samples before and after the exposure to a D plasma. The goal was the investigation of short- and long-term fuel retention properties. To obtain relevant results, W was chosen as a reference material with a well-known behavior, while Ta was investigated as a potential alternative or proxy of W, since there are only few data about its retention properties under fusion-relevant conditions. The experiment allowed familiarization with LIBS spectra, especially for the less-studied Ta, and with in-situ retention measurements, providing fresh results about comparison of W and Ta outgassing dynamics. In addition to LIBS, complementary post-mortem NRA measurements are presented, providing an independent and quantitative assessment of long-term deuterium retention.
Finally, Chapter 7 summarizes the main conclusions and outlines possible future developments of the work.

3 LIBS instrumentation for BiGyM

The performance of a LIBS diagnostics and its detection capabilities are strongly determined by the characteristics of both the excitation laser and the spectrometer. To support the selection of the most suitable characteristics for laser and spectrometer for the in-situ LIBS on the BiGyM linear device a literature research was carried out.
Section 3.1 discusses on the influence of the main laser parameters on the diagnostics performance, presenting some results from LIBS reference literature and from the analysis of tungsten LIBS spectra; after this study, the specifications of the acquired laser are presented and its characteristics critically motivated. Section 3.2 presents a small theoretical introduction about spectrometers and gratings, successfully explaining the characteristics of the spectrometer that will be used for the LIBS on BiGyM. Finally, Section 3.3 illustrates a technical layout of the optical path designed to couple the laser to the linear device.

3.1 Influence of laser parameters on LIBS performance

Several laser parameters, primarily pulse duration, energy and fluence, wavelength, and repetition rate, affect the ablation efficiency, plasma plume properties, and reproducibility of the emission spectra; these parameters have a strong impact on the performance of a LIBS diagnostics. In this section, the influence of each parameter is examined individually, with the goal of identifying suitable characteristics for a laser system intended for fusion-relevant analyses on a LPD.

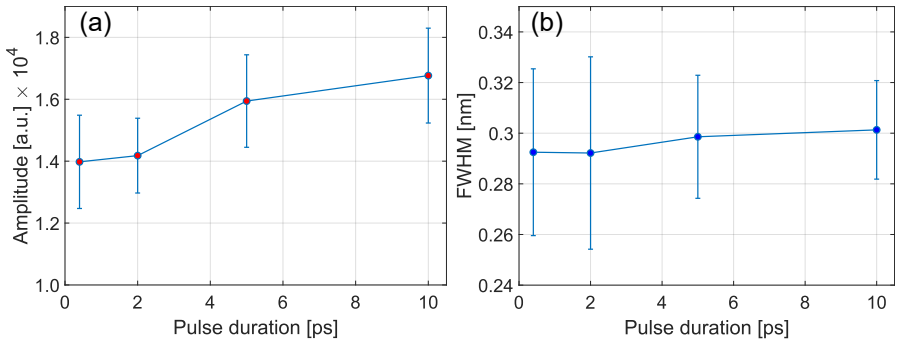

Figure 3.1: Average value over 50 consecutive pulses of amplitude (a) and FWHM (b) of hydrogen peak in W for 4 different values of the laser pulse duration (10 ps, 5 ps, 2 ps and 400 fs).

3.1.1 Pulse duration

Pulse duration τ is one of the most fundamental parameters for LIBS, influencing both the ablation regime and the properties of the resulting plasma plume. As discussed in Section 2.1.3, unlike the ns laser ablation, in the ps regime the electron-phonon relaxation time τ_{e-i} is comparable to τ. As a consequence, the ionic lattice undergoes a limited temperature increase during pulse incidence. Moreover, the thermal diffusion length $l_{\text{th}} \sim 2 \cdot \sqrt{D_{th}\tau}$ is significantly reduced for shorter pulses, leading to increased thermal confinement with a shorter HAZ, limiting the formation of microcracks and regions with melted material [67]. The resulting ablation craters exhibit sharper edges and well-defined ablation geometries. These features are highly advantageous for retention studies, making ps lasers a preferable choice with respect to ns when depth resolution is an important aspect for the analysis.

Another important difference between pulse-duration regimes arises from the laser-plasma interaction. As discussed in Subsection 2.1.3, in the ns regime the plasma generated during the pulse absorbs a significant fraction of laser energy, leading to higher initial plasma T and n; this will produce a generally high intensity emission but also an intense continuum background radiation. Marín Roldán et al. [44] showed, comparing LIBS spectra from WCu samples obtained with a τ of 5 ns and 30 ps, that the shorter pulse typically exhibits a lower intensity signal, because of lower initial plasma T and n, implying also narrower emission lines and an improved Signal to Noise Ratio (SNR).

To study this effect a pulse duration sensitivity analysis was performed by irradiating a tungsten sample with a PHAROS laser characterized by a tunable τ between 400 fs and 10 ps. The targets were irradiated by a series of pulses at 1030 nm with a fluence around 6 J/cm^2, using four different pulse durations.

The spectra were analyzed using an Isoplane 320A spectrometer (spectral resolution of ~ 0.03 nm), with a gate delay of 200 ns and an integration time of 50 ns, optimized to analyze the H_α peak. Figure 3.1 shows the average result over 50 spectra for the net signal amplitude (a) and the FWHM of the hydrogen peak (b) considering different pulse durations; while the former exhibits a significant reduction as the pulse duration decreases, the latter shows a slight downward trend, in agreement with the previously mentioned results.
In conclusion, the choice of a ps laser for in-situ LIBS retention analysis offers significant advantages over ns pulses in terms of depth resolution and peak width, while maintaining a sufficiently high peak intensity.

3.1.2 Pulse energy and fluence

The combination of pulse energy and focal spot size determines the fluence delivered to the target surface, influencing both the ablation regime and the characteristics of resulting plasma.
As widely reported in the literature, the ablation rate does not increase linearly with fluence but follows distinct regimes associated with different material removal mechanisms. An example is presented by irradiation of Mo samples using a ps EKSPLA laser where three different ablation regimes were observed, as shown in Figure 3.2 [68].

- At low fluence, material removal is extremely limited and increases logarithmically with fluence; SEM observations in this regime reveal no evidence of heat-induced structural modification, suggesting that material removal can be dominated by non-thermal ablation mechanisms, for example driven by photomechanical processes.

- By increasing fluence beyond approximately $4\,J/cm^2$, a thermal-dominated regime is observed, where melting and normal evaporation are the primary causes of material removal. This regime is characterized by an approximately linear trend of the ablation depth with fluence. SEM analysis of ablation crater cross section obtained with the Focused Ion Beam (FIB) technique showed a subsurface grain deformation extending a few micrometers below crater bottom, indicative of heat diffusion into the bulk.

- At even higher fluence, above the threshold of $10\,J/cm^2$, a sudden change in energy coupling gives rise to the onset of phase explosion, characterized by a sudden increase of the ablation depth, producing a steeper linear curve in the ablation rate trend with fluence. By SEM observations the presence of re-solidified droplets and ejected particulates around the crater

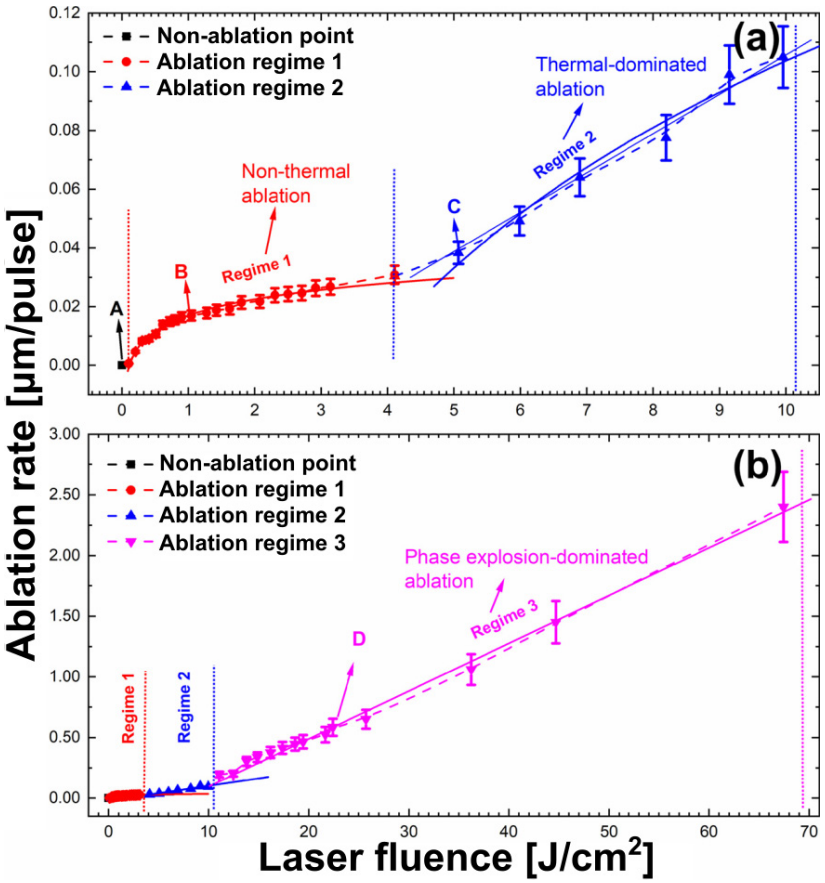

Figure 3.2: Ablation depth per pulse as a function of fluence for Mo, irradiated by a 35 ps Nd:YAG laser at third harmonic (355 nm). In (a) regimes 1 and 2 are highlighted, in (b) all the 3 regimes are present [68].

is observed, confirming the explosive nature of this phenomenon. Another typical feature is the bubble-like structure morphology generated on the crater bottom, creating a rough microstructure on the surface [69].

Fluence threshold between the different regimes usually depends on focusing conditions, pulse duration and material properties: for example phase explosion threshold for a 10 ps laser pulse has been reported to be just above $5\,J/cm^2$ and around $1.5\,J/cm^2$ for gold and aluminum, respectively [70]. For depth profiling and space-resolved retention analyses, working in the low ablation regime is an advantage, because it allows to minimize or avoid thermal effects maintaining a good depth resolution.
Fluence affects not only the ablation regime but also plasma emission features recorded by LIBS. Experiments performed on W samples exploiting the same 35 ps laser cited above showed that the SNR of W spectral lines is fluence-dependent with a non-monotonic behavior [71].
To confirm this fact, another analysis was carried out using the same PHAROS laser and the same tungsten samples discussed in Subsection 3.1.1, keeping the pulse duration fixed at 10 ps and varying the fluence in the interval $4 - 12\,J/cm^2$. 128 consecutive spectra were collected using the same spectrometer settings presented above, computing the average SNR of the H_α line and its relative standard deviation (RSD), computed as:

$$\mathrm{RSD}[\%] = \frac{1}{\overline{\mathrm{SNR}}} \cdot \sqrt{\frac{\sum_{i=1}^{N} (\mathrm{SNR}_i - \overline{\mathrm{SNR}})^2}{N-1}}, \tag{3.1}$$

where $\overline{\mathrm{SNR}}$ is the average SNR and N is the number of measurements (128 in this case). The results of this analysis are shown in Figure 3.3. The RSD, which represents the measurement precision, has a decreasing trend with fluence reaching a stable value above $7\,J/cm^2$, likely caused by the high influence of the dark noise due to the small net signal intensity at low fluences. In contrast, the SNR shows a non-monotonic behavior with fluence, with a peak value around $6\,J/cm^2$. From this plot, it should be reasonable to choose a fluence working point value around $8.5 - 12\,J/cm^2$, which guarantees a good SNR minimizing the RSD.
The considerations done about the ablation regime and the analysis of the signal variation with fluence confirms that for each experiment, depending also on the spectral emission line that need to be studied, the choice of the fluence value operating point is a trade off between the signal optimization and the selection of the desired ablation regime. For fuel retention studies working at very low

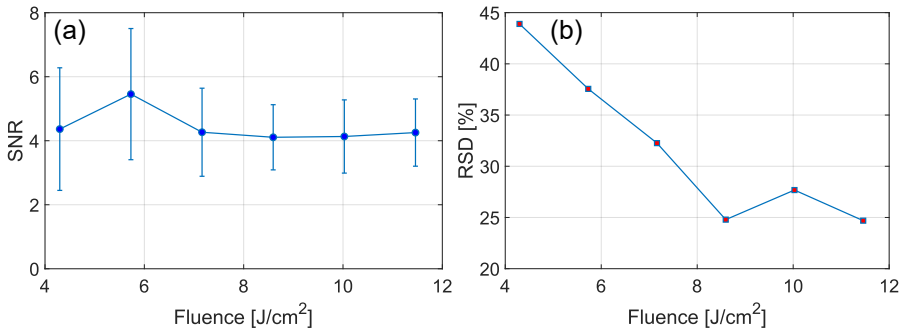

Figure 3.3: SNR (a) and RSD (b) trends for H_α line on tungsten for different fluence values. A gated iCCD was used for these measurements, with a gate delay of 200 ns and an integration time of 50 ns .

fluence, in the first or the beginning of the second ablation regimes, is particularly advantageous especially for depth-resolved analyses.
In conclusion, the availability of a high maximum pulse energy for the laser is always a good choice, since it allows to have more flexibility on the experimental working point.

3.1.3 Wavelength

Modern solid-state lasers, such as Nd:YAG, can operate not only at their characteristic wavelength but also with different wavelengths exploiting nonlinear optics processes. When an intense laser pulse passes through a suitable nonlinear crystal, waves with frequencies that are multiples of the fundamental one are generated. As a result, a single laser source can deliver pulses with different wavelengths (e.g. 1064 nm, 532 nm 355 nm for a Nd:YAG system), although at the expense of a reduced maximum pulse energy, due to the limited efficiency of the nonlinear conversion process. The adoption of higher harmonics can be used to affect both the ablation crater characteristics and the interaction with the induced plasma.
Regarding laser-material interaction, most of the fusion-relevant metals typically exhibit reflectivity that increases with wavelength. As illustrated in Figure 3.4, the reflectivity of W and Mo is significantly higher going from the UV to the NIR wavelength range. As a consequence, shorter wavelengths deposit a larger energy fraction on the target, leading to a higher ablation efficiency with deeper craters for comparable pulse energies; this implies a decrease of the depth resolution and a net increase of the ablated mass and so of the spectral signal. Experiments performed on W-ITER samples irradiated by a ps Nd:YAG laser

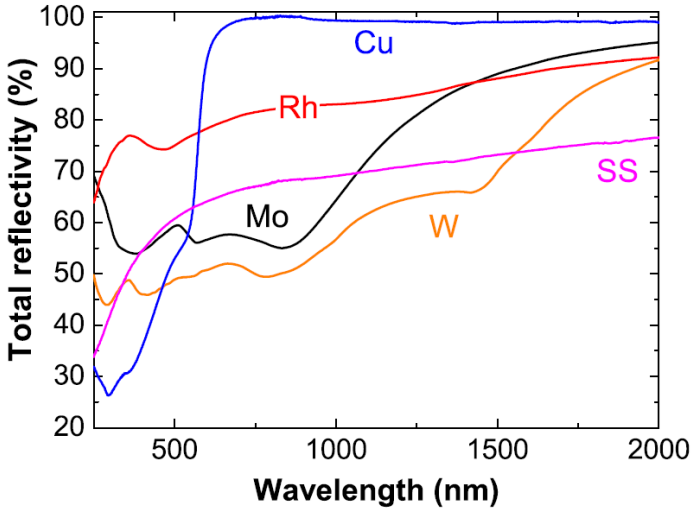

Figure 3.4: Total reflectivity of different metals as a function of wavelength [72].

confirm this trend: using the fundamental harmonic allows a reduction by a factor 3 of the ablation rate with respect to the second harmonic [73].
A second distinct effect arises from laser-plasma interaction. As mentioned in 2.1.4 the efficiency of the IB process, which governs the energy absorbed by the free electrons of the plasma, scales with λ^3. As a result, plasmas generated with longer wavelength pulses are usually characterized by higher electron temperature and density, especially for higher values of fluence. This behavior was observed, for instance, in ps Nd:YAG irradiation experiments of a pure Cu sample using four different harmonics [74]. As illustrated in Figure 3.5 the computed plasma electron temperature increases with pulse E and is higher for longer wavelengths. This aspect, along with the increase of emission intensity for many atomic and ionic lines, leads to an increase of SNR when decreasing the wavelength.
In practice, for standard LIBS applications the use of fundamental harmonic is typically sufficient to obtain reliable and reproducible measurements. It provides good compromise between available energy and depth resolution, making it suitable for large part of the analyses. The use of higher-order harmonics may be necessary to achieve more specific experimental objectives, such as the maximization of the ablated mass or the mitigation of the background continuum emission. In these cases, the possibility of changing the wavelength represents an additional degree of freedom to find the desired experimental conditions rather than being a necessary requirement.

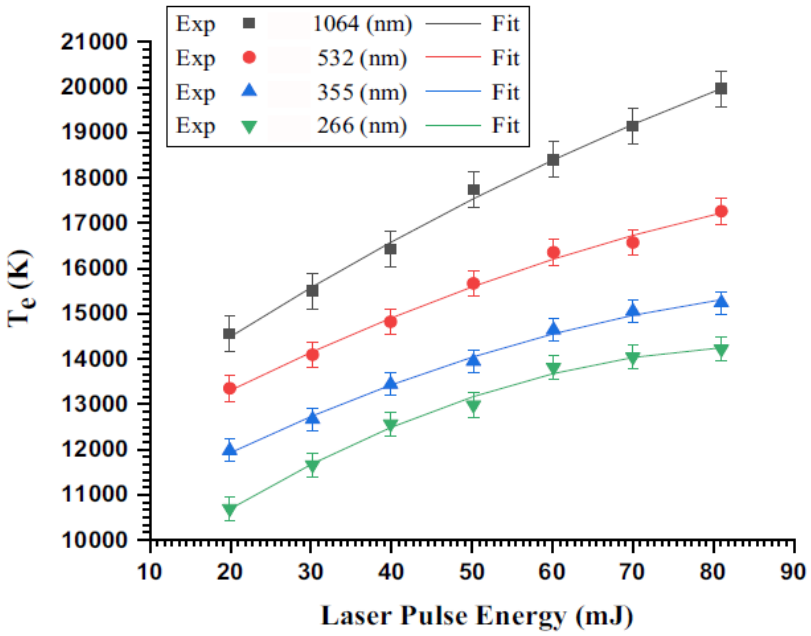

Figure 3.5: The effect of different λ on the plasma electron temperature for Cu [74].

3.1.4 Repetition rate

The influence of repetition rate on LIBS performance is closely connected to the evolution and the lifetime of the plasma plume. If the interval between pulses is too short, residual emitted particles can interact with the arrival laser beam, introducing an undesired influence on ablation and new emission. The independence between two consecutive pulses is assured if the ambient gas state before the second pulse is identical to the one persisting before the first pulse; for this condition to be satisfied the residual vapor and ablated material must be removed from the interaction volume within a short time interval [75].
A simple estimation illustrates the relevant timescales. Considering a 35 ps single laser pulse with $F \approx 4\,\mathrm{J/cm^2}$ irradiating an ITER-W sample, experimental data [68] show that the ablated mass for a 500 µm crater diameter is around 100 ng, corresponding to $3.3 \cdot 10^{14}$ atoms. By exploiting the ideal gas law and assuming the expansion of a plasma plume with $T \approx 15\,000$ K and $p \approx 1$ atm, the volume occupied by the plume can be estimated. Assuming a hemispherical plume, the resulting radius R is around 0.685 mm, corresponding to an atomic density of the plume of $5.1 \cdot 10^{17}\,\mathrm{cm^{-3}}$. This value is much lower than the ambient gas density at atmospheric pressure ($2.5 \cdot 10^{19}\,\mathrm{cm^{-3}}$), indicating that the plasma plume can be efficiently transported away by the surrounding gas flow.
The absence of interaction with the residual ablation cloud is achieved if the

pulse period $T = 1/RR$ exceeds the required time to displace the plume from its initial position by a distance equal to twice its diameter (d_{plume}), defined as the local gas exchange time τ_{ge}:

$$T > \tau_{\mathrm{ge}} = \frac{2d_{\mathrm{plume}}}{v}. \tag{3.2}$$

Here, v represents the flow velocity of the ambient gas, which is practically limited by the speed of sound at room temperature ($\sim 300\,\mathrm{m/s}$). Using the values computed above, $\tau_{\mathrm{ge}} \approx 10\,\mu\mathrm{s}$; so the maximum RR to ensure pulse-to-pulse independence with respect to residual gas is 100 kHz. This value exceeds RR typically employed by lasers for LIBS experiments, where values below 1 kHz represents a practical maximum [75].
In vacuum, the absence of background gas confinement allows the pulse to disappear more rapidly, with typical expansion timescale of the order of few µs, depending on the ablation conditions; also in this case, pulse-to-pulse interactions are negligible for RR commonly adopted for LIBS lasers.
In summary, for repetition rates typically employed in LIBS experiments (up to 1 kHz), pulse-to-pulse interaction has no practical influence on the analysis, whether spectra are acquired individually or cumulated over multiple shots. The residual ablated vapor plume produced by each laser shot dissipates well before the arrival of the subsequent pulse, ensuring that each pulse interacts with a clean gas environment.
It is worth noting that the deliberate exploitation of pulse-to-pulse interactions forms the basis of the Double-Pulse LIBS (DP-LIBS) technique, in which a second laser pulse is fired onto the plasma plume to enhance the emission signal. However, the inter-pulse delay required for this technique is typically in the ns-to-µs range, far shorter than pulse separation time achievable with the above-mentioned repetition rates. However, the implementation and investigation of this configuration is out of the scope of this work.

3.1.5 PL2231A-10 Ekspla laser parameters

The laser acquired for the LIBS diagnostic on BiGyM is the PL2231A-10 EKSPLA, a picosecond Nd:YAG system, specifically designed for high stability and long-term operational reliability. It is characterized by a fully diode-pumped architecture without the use of flashlamps, significantly extending the lifetime of the pumping system. The laser employs a passively mode-locked solid-state oscillator followed by a double-pass and a regenerative amplifier, which ensure excellent temporal and spatial beam quality. These characteristics are reflected

in the pulse-to-pulse energy stability (below 5% standard deviation) and the near-Gaussian beam profile, with a M^2 factor lower than 2.5.

Parameter	**Value**
Nominal wavelength [nm]	1064
Pulse duration [ps]	29 ± 5
Pulse duration stability [%]	± 1
Max pulse energy @ 1064 nm [mJ]	65 (best effort 70)
Pulse repetition rate [Hz]	10
Beam profile	Close to Gaussian (near and far fields)
Typical beam diameter [mm]	~ 7
Beam divergence [mrad]	≤ 0.7
Beam propagation ratio (M^2)	≤ 2.5

Table 3.1: Main specifications of the PL2231A-10 laser chosen for LIBS on BiGyM.

The main laser parameters are summarized in Table 3.1. A picosecond pulse duration (≈ 29 ps) was chosen, as discussed in Subsection 3.1.1 to minimize thermal effects during the interaction with materials, thereby reducing the HAZ and improving crater definition; these aspects, along with the reduced continuum background and the achievement of narrower spectral lines, are advantageous for depth-resolved fuel retention studies.
The system delivers up to $65 - 70$ mJ per pulse at the fundamental wavelength (1064 nm), with the output energy adjustable in steps of approximately 1%. As mentioned in Subsection 3.1.2, the access to higher pulse energies allows flexibility in the available fluence, which is particularly advantageous when it is necessary to find the optimal experimental conditions.
Recalling the discussion of Subsection 3.1.3, operating at the fundamental harmonic is a suitable starting point for routine LIBS analyses. Nevertheless, the system supports the integration of nonlinear crystals allowing, through a future upgrade, operations even with 532 nm or 355 nm.
The system includes additional features, such as low-jitter internal triggering, robust beam-pointing stability, and remote control capabilities, to facilitate synchronization with the spectrometer acquisition and ensure stable operations and in situ measurements. These attributes make the PL2231A-10 laser particularly well-suited for LIBS measurements in LPDs, especially for fuel retention and depth profiling measurements in fusion-relevant materials.

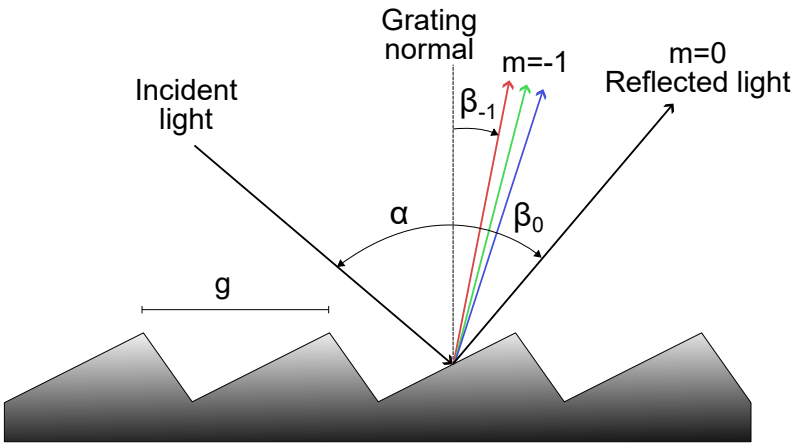

Figure 3.6: Scheme of light spectral decomposition through diffraction grating. Incidence angle α and diffraction angles β_m are indicated.

3.2 Spectrometer

Laser-induced plasmas typically reach electron temperatures of the order of $T_e \approx$ 20 000 K, producing an emission spectrum in the Ultra-Violet (UV) and VISible (VIS) wavelength regions, where most characteristic atomic and ionic transitions are detectable [31]. Optical spectrometers are therefore essential components of a LIBS system, enabling the reconstruction of the emitted spectrum and the identification of chemical species.
The schematic layout of an optical spectrometer generally consists of five key elements:

- an entrance slit, which defines the spatial resolution and limits the collected light;
- a collimating optic (lens or mirror), which transform the divergent entering beam from the slit into a collimated one, essential before performing the light dispersion;
- a dispersive element, typically a prism or a diffraction grating, which separates the polychromatic light into its wavelength components;
- a focusing optic system, which images the dispersed wavelengths onto different positions of the detector;
- a detector, which converts the spatially separated wavelengths into a digital spectrum.

The dispersive element represents the core component of a spectrometer, and the diffraction grating is the most common choice in LIBS, due to the high spectral resolution and broad wavelength coverage.
A diffraction grating consists of a periodic structure of reflective or transmitting elements separated by a certain distance g, which must be comparable to the wavelength of the analyzed light. When illuminated by a polychromatic radiation, it diffracts the incoming beam into different wavelength components according to the grating equation [76]:

$$g(\sin\alpha + \sin\beta_m) = m\lambda \tag{3.3}$$

where α is the incident angle, and β_m is the diffraction angle of order m. Figure 3.6 shows a representation of a diffraction grating scheme; the angles are measured from the normal to the grating surface, and diffraction angles in the same direction of the incident one are considered positive.
Assuming a fixed incidence angle, the angular dispersion D of a spectrum of order m can be calculated differentiating equation (3.3):

$$D = \frac{\mathrm{d}\beta}{\mathrm{d}\lambda} = \frac{m}{g\cos\beta}. \tag{3.4}$$

This parameter quantifies the angular separation, for a spectrum of order m, of two nearby wavelengths. However, in practical spectrometers, what matters is not the angular separation alone but the consequent spatial separation on the detector, called the linear dispersion $D_{\text{lin}} = \mathrm{d}x/\mathrm{d}\lambda$. A parameter often reported in the literature is the reciprocal linear dispersion, also called plate factor P, defined as:

$$P = \frac{1}{D_{\text{lin}}} = \frac{1}{Df} = \frac{g\cos\beta}{mf} \tag{3.5}$$

where f is the focal length of the system. The quantity P directly links the change in wavelength corresponding to a linear distance on the detector. For a detector with N_{pixel} pixels with size p, the covered spectral range at a fixed α can be calculated as [31]:

$$\lambda_{\text{max,min}} = \lambda \pm \frac{P \cdot N_{\text{pixel}} \cdot p}{2}. \tag{3.6}$$

A key aspect of grating performance is its ability to resolve closely spaced spectral lines. Two important quantities commonly used to describe this aspect are the resolving power R and the limit of resolution $\Delta\lambda$. The former is a measure of the spectrometer ability to separate adjacent spectral lines around a certain

wavelength λ and is usually expressed as:

$$R = \frac{\lambda}{\Delta\lambda} = mN, \tag{3.7}$$

where N is the number of grooves illuminated on the surface grating. The second expression in Eq. (3.7) shows that, for a fixed grating length, increasing N leads to a higher resolving power. However, the increase of N implies a higher groove density reducing the parameter g; as a consequence, the spectral range covered by the detector is reduced, in accordance with Equation (3.6), highlighting the intrinsic trade-off between spectral resolution and accessible λ range.
The limit of resolution $\Delta\lambda$ is defined as the minimum wavelength separation for which two spectral lines of equal intensity can be distinguished; it is often evaluated using the Rayleigh criterion, which states that two spectral peaks are resolvable if the intensity maximum of the first one is located at the minimum of the second one. This distance is the definition of the FWHM of a spectral line. While R is primarily determined by the grating characteristics, $\Delta\lambda$ depends on a broader set of factors, including entrance and exit slit widths, imaging aberrations induced by the collimating and focusing optics, image magnification, and the pixel size of the detector.
Diffraction gratings can be produced with different manufacturing techniques with relevant consequences on their performance. Ruled gratings are produced by mechanically engraving grooves onto the surface with a diamond tool, with the help of a precision ruling engine; this type of grating typically offers high efficiency but may suffer from high stray light due to imperfections in ruling process. Holographic gratings, on the other hand, are fabricated exploiting two interfering laser beams onto a photosensitive substrate, generating a sinusoidal structure of grooves. They are usually characterized by lower efficiency, but the high groove density allows for maximizing the resolution.
A further developed design is represented by the blazing configuration, where the grooves are tilted with an angle Θ_{B} to maximize the diffracted intensity for a selected order or wavelength range. Maximum efficiency is reached under Littrow configuration, where the incident and diffracted beams coincide ($\alpha = \beta$); in this case the blazing angle that satisfies the constructive interference for a certain λ can be found by this expression:

$$\Theta_{\mathrm{B}} = \arcsin\frac{m\lambda}{2g}. \tag{3.8}$$

The spectrometer selected for LIBS diagnostics on BiGyM is the IsoPlane 320 (Princeton Instruments), a high-resolution spectrograph based on an optical

design specifically optimized to minimize the chromatic aberrations over the full entrance-slit height, in contrast to conventional Czerny-Turner configuration. Despite its compact footprint and relatively short focal length of 320 mm, the IsoPlane 320 provides high spectral resolution (the nominal value is 0.08 nm with a 1200 g/mm grating) by effectively correcting optical aberrations across the entire field of view. It is equipped with a filter holder wheel for the elimination of peaks at different diffraction orders. Three different reflective gratings can be interchanged, each with different characteristics and optimized for different spectral regimes:

- a 2400 g/mm **holographic grating**, optimized for the visible range, providing high dispersion required for fine-resolution tasks such as the separation of H_α and D_α lines;
- a 1800 g/mm **holographic grating**, optimized for near-UV applications, offering a good compromise between spectral resolution and accessible wavelength range;
- a 1200 g/mm **ruled grating** blazed at 300 nm; it is designed for the same near-UV spectral region but characterized by a lower groove density. Compared to the 1800 g/mm, it provides a broader spectral range at the expense of a reduced resolution.

This set of gratings allows flexible operations across a broad range of wavelengths, enabling both analysis of impurity lines and hydrogen-isotope detection.
Plasma emission is collected through a bundle of 19 optical fibers, which are disposed in a linear vertical configuration on the spectrometer side, to cover the entire entrance slit height maximizing the light collection. The entrance slit width is adjustable, with a minimum of 10 µm: reducing the slit improves the spectral resolution at the cost of a reduced light collection and SNR.
The signal detection is performed using a PMAX intensified CCD camera (iCCD), featuring a 1024×256 pixel array of 26 µm $\times$ 26 µm size each, cooled at -20 °C to minimize dark current. The intensifier is a Gen II (super red) type, with a quantum efficiency (illustrated in Figure 3.7) peaked between $500 - 700$ nm, enhancing sensitivity for H_α and D_α lines. Fiber coupling between intensifier and CCD ensures efficient transmission and compact integration. The iCCD also offers fast gating capability on nanosecond scale, allowing suppression of early-time continuum emission and enabling time-resolved analysis of signal evolution.
Since LIBS signals in the UV region are intrinsically quite intense, the intensifier characteristics allow analyses over a broad region of wavelengths, always with

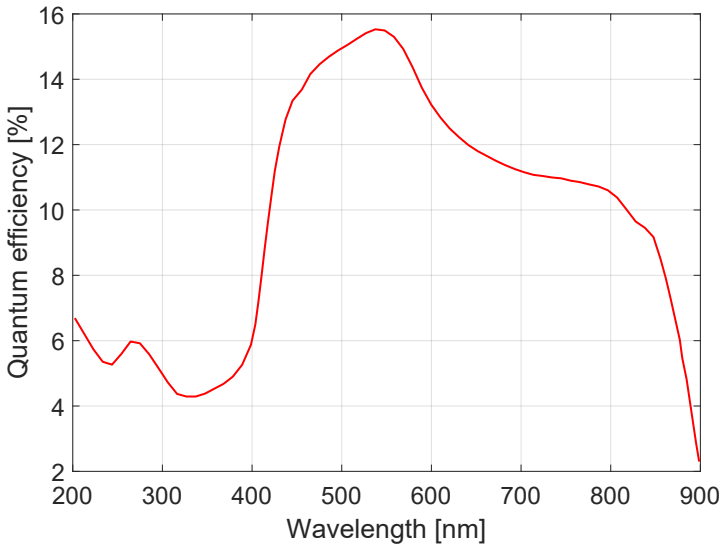

Figure 3.7: Quantum efficiency of the Super Red Gen II intensifier as a function of wavelength.

focusing on retention studies. The combination of compact design, aberration correction, flexible grating design, efficient fiber coupling, and time-gated detection, makes the IsoPlane 320 spectrometer well suited for in-situ LIBS studies on a LPD.

3.3 Optical path design

A dedicated optical path has been designed to connect the laser system to the BiGyM linear device (located in a different room), enabling LIBS measurements on plasma-exposed samples. A technical drawing of the optical path is shown in Figures 3.8 and 3.9, reporting respectively a lateral and a top view of the system. The laser beam is guided by a set of mirrors and is enclosed within safety tubes up to the optical window of the linear device. In the laser room, which is not represented in the drawings, the beam travels a total path of approximately 290 cm and is deflected by two flat mirrors to raise it to a height of 250 cm from the floor. The choice of this beam height was made to avoid obstructions and space interferences around the linear device.
Before entering in the BiGyM pre-chamber, the laser beam is deflected twice: the first time by a fixed mirror and then by a motorized steering mirror. The latter provides two rotational degrees of freedom, allowing remote adjustment of the beam position on the target surface. Overall, the beam propagates over a total distance of approximately 780 cm considering both the laser and the

BiGyM rooms. Along this path, the optical layout includes three flat mirrors, one motorized steering mirror and one focusing lens.
An estimate of the laser beam expansion along the optical path, without considering the presence of the focusing lens, can be obtained using the far-field approximation, according to Equation (2.3). By considering the laser beam diameter and divergence data reported in Table 3.1, the beam diameter after 780 cm of propagation is expected to be approximately 12.5 mm, i.e., about 5.5 mm larger than at the beginning of the optical path.
Overall, the proposed optical layout ensures a stable and robust beam path from the laser system to the target, while complying with safety constraints and spatial limitations of the experimental environment, providing a first idea for the configuration of the in-situ LIBS system on the BiGyM linear device.

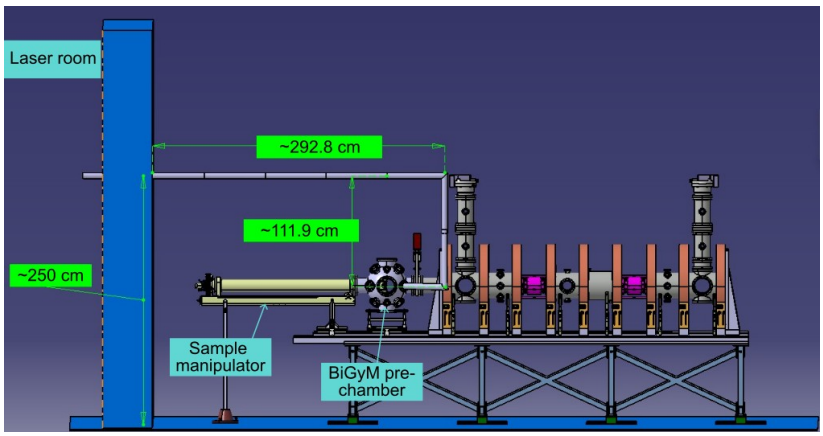

Figure 3.8: Lateral view of the laser optical path in the BiGyM room.

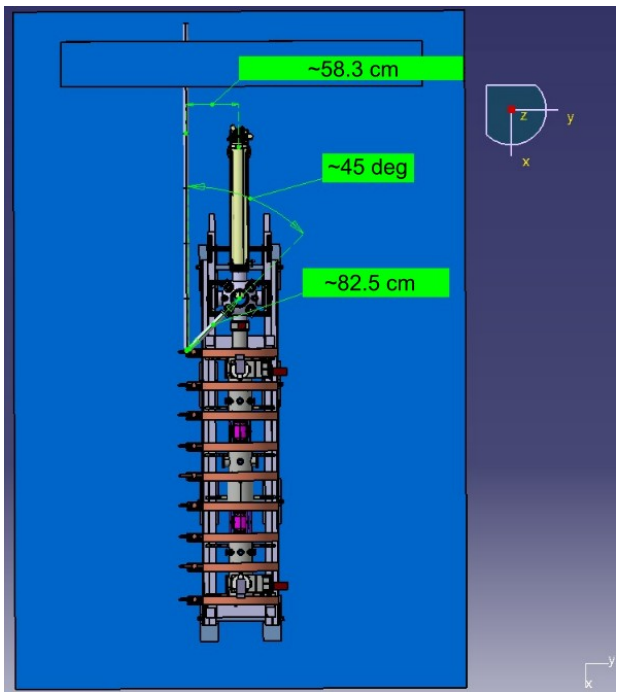

Figure 3.9: Top view of the laser optical path in the BiGyM room.

4 Nanosecond laser ablation modeling

Despite the growing interest in ultrashort-pulse regimes (picosecond and femtosecond), which allow for achieving higher depth resolution when performing retention and depth-resolved measurements, nanosecond lasers remain the reference choice in many experimental setups due to their maturity and flexibility. In the nanosecond regime, the interaction between the laser pulse and the target is dominated by thermal processes. Laser energy deposition leads to significant heat diffusion into the material bulk, inducing melting and mass removal through normal evaporation or, at sufficiently high fluence, phase explosion. These mechanisms strongly influence the ablation rate and the crater morphology, which, in turn, determines the achievable depth resolution of the LIBS measurement. Compared to picosecond irradiation, nanosecond ablation is characterized by a larger HAZ and, consequently, by thermal-induced phenomena like cracks, melt resolidification, and redeposition of ejected material.
In the context of fuel retention and depth-resolved LIBS measurements, a quantitative prediction of crater depth and its lateral extension is essential. In multi-pulse experiments in particular an accurate estimate of ablation rate is required to reconstruct the thickness of the analyzed layer and to correctly interpret the evolution of the spectral signal with pulse number. Moreover, the extended HAZ generated after nanosecond irradiation can directly influence the behavior of retained species, promoting thermal diffusion and outgassing from regions located below the crater bottom, potentially affecting the single-pulse LIBS signal [67].
For these reasons, a computational model capable of describing the laser-matter interaction represents an important support tool for the optimization of LIBS diagnostics. In addition, computing the subsurface temperature field and its

evolution can be useful for the single-pulse LIBS signal correction, for example by comparing isothermal lines with characteristic outgassing temperatures.
This chapter presents the modeling activity developed to simulate nanosecond laser ablation of solid targets using the finite element code COMSOL Multiphysics [77]. The modeling work was structured in a progressive manner and is presented in this chapter accordingly. First, the thermal response of material to laser irradiation is addressed and validated against reference results available from scientific literature (Section 4.1). Subsequently, a complete ablation model including material removal and plasma shielding effect is introduced and validated against experimental data obtained from pulsed irradiation of tungsten and silicon (Section 4.2).
Part of the results presented in this Chapter have been published in a peer-reviewed journal, constituting the core of the article Cipelli et al. [78].

4.1 Foundations of thermal modeling and validation of thermal response

The first part of this section (Subsection 4.1.1) introduces the physical and mathematical foundations of the thermal model used to describe ns laser irradiation of solid targets.
Before introducing the complete ablation model adopted to describe the LIBS crater generation, it is essential to verify the capability of the thermal framework to correctly reproduce the temperature field evolution induced by laser irradiation. For this purpose, the present section focuses exclusively on the heat transfer problem, neglecting mass removal and plasma shielding effect.
For a benchmark of this part, the numerical results of the model were validated against reference results available in the literature. Two representative cases are considered. The first step, presented in Subsection 4.1.2, involved a preliminary validation phase comparing the thermal response of the model with temperature field evolution in alumina under ms irradiation, computed with COMSOL. This choice was made because the longer pulse duration leads to a more manageable numerical evolution, less sensitive to discretization choices, providing a robust and well-controlled benchmark to verify the correct implementation of equations and boundary conditions before extending it to the ns domain. The second validation step, discussed in Subsection 4.1.3, concerns ns laser irradiation of yttria, where the temporal evolution of the maximum surface temperature is compared with results obtained from a 2D finite-difference model. These two cases enabled validation of the thermal response of the computational model

over different pulse durations and numerical implementations, providing a solid basis for the development of the complete ns laser ablation model.

4.1.1 Governing equation and laser heat source definition

In the ns irradiation regime, as mentioned in 2.1.3, laser-matter interaction can be effectively described by a purely thermal approach since the electron-phonon relaxation time τ_{e-i} is shorter than or comparable to the pulse duration. Under this assumption, the absorbed laser energy is rapidly transferred to the lattice, and the temperature evolution within the target $T(\mathbf{r}, t)$ can be described using the classical heat conduction equation:

$$\rho(T)C_p(T)\frac{\partial T}{\partial t} - \nabla \cdot (k(T)\nabla T) = Q, \tag{4.1}$$

where ρ is the mass density, C_p the isobaric specific heat capacity, and k the thermal conductivity of the material. All thermophysical properties are, in general, temperature dependent. Q is the laser heating source term, which can be computed as:

$$Q(\mathbf{r}, t) = (1 - R) \cdot \alpha \exp(-\alpha z) \cdot I_0(\mathbf{r}, t). \tag{4.2}$$

This formulation accounts for the incident laser intensity $I_0(\mathbf{r}, t)$, the surface reflectivity R, and the optical attenuation along the propagation direction z through the Lambert-Beer equation.
In the most common case where the laser spot can be assumed as circular and temporal and spatial distributions can be described by Gaussian functions, the unshielded laser intensity can be written as:

$$I_0(r, t) = \frac{2E}{\pi r_0^2 \tau} \cdot \exp\left[-4\ln 2\left(\frac{t - t_0}{\tau}\right)^2\right] \cdot \exp\left[-2\left(\frac{r}{r_0}\right)^2\right], \tag{4.3}$$

where r_0 is the beam radius (defined according to the adopted Gaussian convention), that can be estimated, for example, from the width of the ablation crater. The multiplicative factor $2E/(\pi r_0^2 \tau)$, which represents the peak intensity, is obtained by the imposition that the integral of $I_0(r, t)$ over time and space equals the pulse energy E.
In this mathematical context, two characteristic lengths determine the spatial scales of the problem: the heat diffusion length l_{th} and the optical absorption depth δ, defined in 3.1.1 and 2.1.4 respectively. The larger of these two lengths provides a first indication of the minimum domain size required to avoid boundary effects on the temperature field evolution.

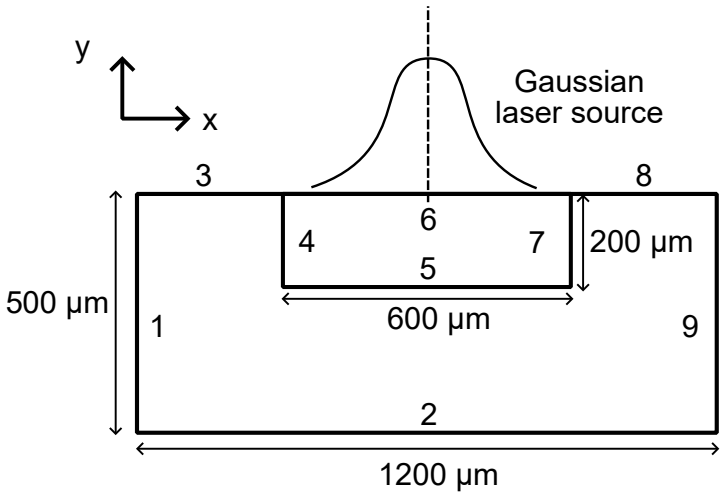

Figure 4.1: Computational domain of the laser ablation model. Each boundary is indicated with a different number [79].

4.1.2 First validation step: millisecond laser ablation of alumina

As a first validation step, the model was benchmarked against the work by Vora et al. [79], who developed simulations for laser irradiation of alumina using a ms pulse. In this comparison, only the thermal part of the reference model was reproduced, i.e., laser incidence and heat transfer in a 2D domain. The coupled part of the model related to fluid flow (for the molten material dynamics description) was not included, since the objective of this step was the validation of the temperature evolution and correct implementation of boundary conditions.

The computational domain adopted in the simulations is shown in Figure 4.1. The author computed a mesh sensitivity analysis, leading to maximum and minimum element sizes of 14 µm and 2 µm respectively. These constraints were applied in the small rectangular domain characterized by the Gaussian laser incidence, while a coarser mesh (typical element size ~ 30 µm) was used elsewhere, resulting in a total number of elements of approximately 2880.

The laser source was implemented as a boundary condition acting on boundary 6, neglecting optical penetration into the material. A simplified rectangular temporal shape of duration τ was employed instead of the standard Gaussian distribution. Heat losses were included on boundaries 1, 3, 6, 8, and 9 through heat convection (heat transfer coefficient $h = 10\,\mathrm{W/m^2K}$) and thermal radiation (with emissivity $\epsilon = 0.7$). The remaining thermophysical properties and laser parameters used are reported in ref. [79].

To account for the energy absorbed or released during phase transitions, the

specific heat was expressed using the following equation:

$$C_p(T) = C_{p,0} + L_m \cdot \delta_m + \frac{L_m}{T_m} \cdot H'(T - T_m, \Delta T) + \\ + L_v \cdot \delta_v + \frac{L_v}{T_v} \cdot H'(T - T_v, \Delta T), \tag{4.4}$$

where $L_{m,v}$ are the latent heat of melting and vaporization, respectively, and $T_{m,v}$ are the melting and vaporization temperatures. In Equation (4.4), $\delta_{m,v} = \exp\{-[(T - T_m)/\Delta T]^2\}/(\Delta T\sqrt{\pi})$ is a Gaussian function with unitary integral and standard deviation equal to ΔT, used to distribute the latent heat consumption over a small temperature interval; $H'(T - T_{m,v}, \Delta T)$ is a smoothed Heaviside function centered around $T_{m,v}$, where ΔT is the amplitude of the smoothed region.

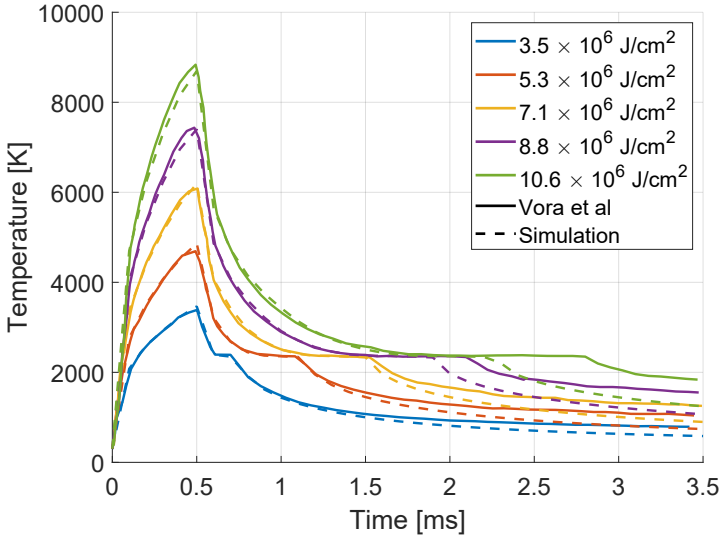

Figure 4.2: Comparison between paper and simulation results for the maximum temperature evolution for different fluence values.

Figure 4.2 compares the temporal evolution of the maximum surface temperature for different fluence values, where solid lines represent reference paper results and dashed lines refer to present simulations. The agreement is qualitatively good, with a discrepancy below 4% on the peak temperature. A more visible difference is observed during the cooling phase, where simulations show a faster decrease than reference results. This behavior is likely associated with differences in the timestep adopted for the numerical method; in the reference work, its value was kept fixed to 0.1 ms, while in present simulations an adaptive time stepping strategy was necessary to avoid convergence issues in the newest COMSOL version.

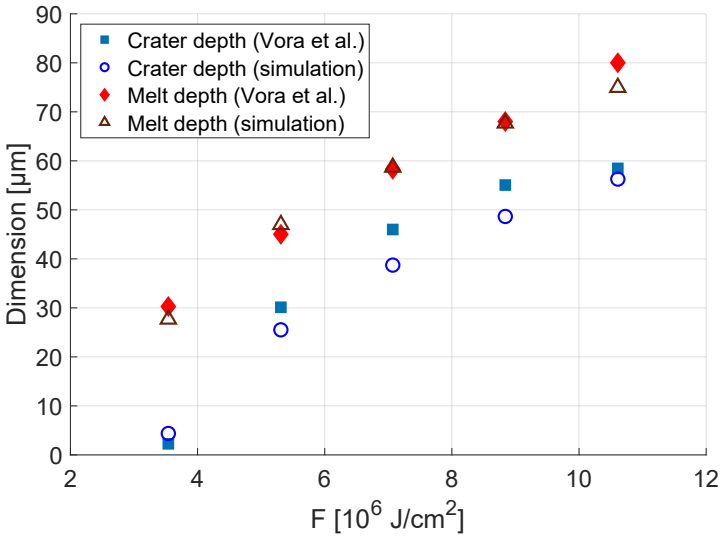

Figure 4.3: Comparison of predicted crater and melted region depths for various laser fluences.

An estimation of the ablation and melting region depths was obtained by considering domain portions associated with temperature values above T_m and T_v, respectively. Figure 4.3 shows the comparison between reference and reproduced values for crater depth and melt depth as a function of fluence. Both the qualitative trends and absolute values are in good agreement, with relative discrepancies below 16% and 9% for crater and melt depth, respectively. The lowest fluence point exhibits a larger relative discrepancy ($\approx 90\%$); however, this is mainly due to the very small absolute value in that condition, as the two results differ only by 2 µm.
Overall, this first benchmark confirms that the numerical implementation of the thermal problem related to laser energy absorption (boundary heating, phase-change treatment, and heat losses) using COMSOL Multiphysics is able to reproduce reference results for temperature evolution and associated melt/ablation crater depth with satisfactory accuracy; this provides a reliable basis for the subsequent validation considering a ns laser pulse, and for the development of a complete ablation model.

4.1.3 Second validation step: nanosecond laser ablation of yttria

As a second validation step, the model was benchmarked against the work by Sinha [59], who developed a finite-difference thermal model to investigate laser ablation of yttria (Y_2O_3), for pulsed laser deposition applications. This case represents a relevant test for the present COMSOL model, since it involves ns

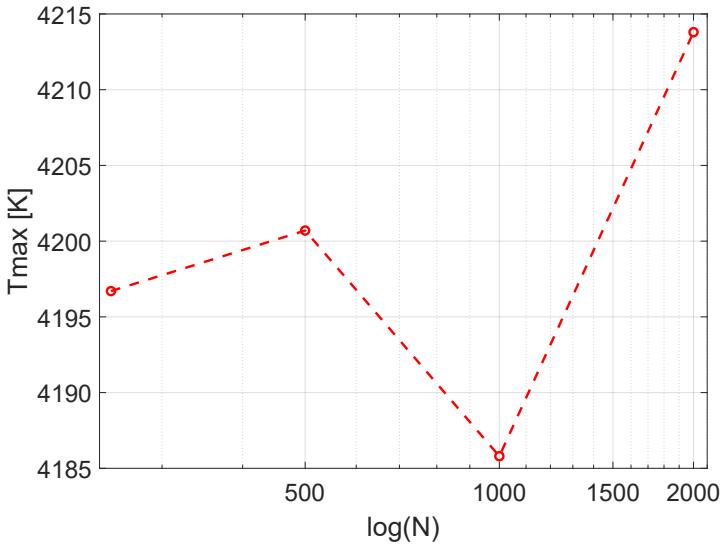

Figure 4.4: Maximum temperature on the surface as a function of vertical mesh size.

laser pulse duration, high surface temperatures, latent heat consumption during phase transition and plasma plume shielding effects, while still allowing for a comparison focused on temperature response.

Validation was carried out by reproducing the temporal evolution of the maximum surface temperature for a space-averaged fluence value of $6\,\mathrm{J/cm^2}$, below the ablation threshold of yttria. Material removal because of ablation was not considered, allowing to isolate the thermal behavior and to verify the consistency between different numerical methods.

The laser pulse was implemented as a volumetric heat source according to equation (4.2), with Gaussian distributions in space ($FWHM = 420\,\mu\mathrm{m}$) and time ($\tau = 5\,\mathrm{ns}$). Solid-liquid phase transition was addressed in COMSOL using the phase change material subnode. This feature allows to include any change in thermophysical properties and the consumption of the latent heat of melting around the boiling point. The latter is considered introducing an apparent heat capacity $C_p = C_{\mathrm{eq}} + C_{\mathrm{L}}$, where C_{eq} is the equivalent heat capacity, dependent on the current phase, and C_{L} represents the latent heat distribution [80]. The remaining thermophysical properties and laser parameters are reported in ref. [59].

The computational domain was rectangular, with a height of $40\,\mu\mathrm{m}$ and a width of $800\,\mu\mathrm{m}$ measured from the center of the laser pulse. In the reference work, a mesh with variable radial element size (ranging from 10 to $50\,\mu\mathrm{m}$) and an extremely fine vertical resolution ($4\,\mathrm{nm}$) was employed. However, such a small vertical mesh size would have resulted in excessively long computational time

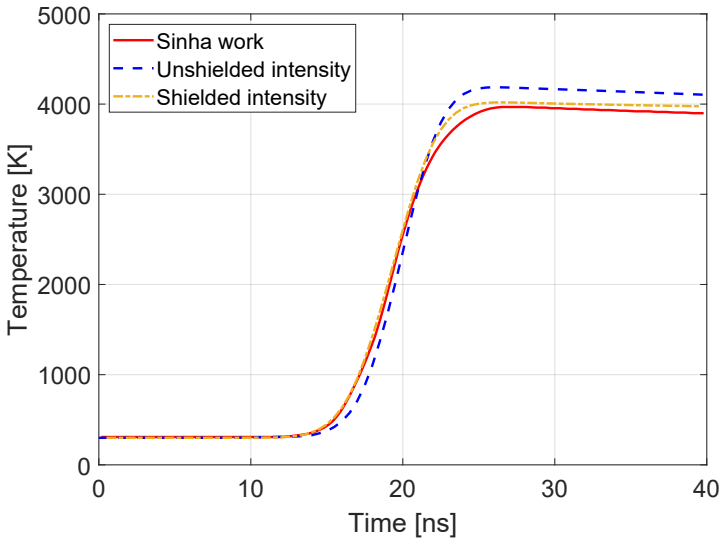

Figure 4.5: Comparison between computed peak temperature evolutions for an incident average fluence of $6\,\mathrm{J/cm^2}$.

for the present COMSOL simulation. For this reason, a sensitivity analysis on the vertical mesh resolution was performed to find a suitable compromise between numerical accuracy and computational efficiency.
The results of the sensitivity analysis is shown in Figure 4.4. Small oscillations around a mean value of approximately 4200 K can be observed, with a maximum amplitude of about 15 K, corresponding to a relative variation of roughly 0.3%. Based on this result, a mesh composed of 1000 vertical elements (40 nm vertical size) was selected.
The temporal evolution of the maximum surface temperature obtained with the selected mesh is illustrated in Figure 4.5 and compared with result from the reference paper. A good agreement is observed even without considering plasma shielding effect, with a relative discrepancy between maximum values around 5.5%. A slight delay in the temperature rise is predicted by the present model with respect to the reference curve, which can be attributed to the absence of plasma shielding effect, implemented instead in the reference paper using an exponential attenuation factor; this modifies the pulse temporal Gaussian shape, shifting the peak forward and reducing the maximum intensity.
To account for this, an artificially modified temporal Gaussian was introduced in the present model. The resulting temperature evolution curve is represented by the yellow dash-dotted curve in Figure 4.5. With this correction, the first part of the curve closely matches the reference result, and the relative difference in maximum values is reduced to $\sim 1.3\%$.

This second validation step confirms that the COMSOL thermal model is able to reproduce temperature evolution reported in literature also considering ns pulses, ensuring consistent results across different numerical models. This provides further robustness for the thermal model prior to the introduction of material removal and an effective equation to take into account plasma shielding.

4.2 Nanosecond laser ablation model and validation for tungsten and silicon

This section presents the complete two-dimensional model developed for ns laser ablation and its validation against experimental results obtained for tungsten and silicon samples. The model, whose details are described in Subsection 4.2.1, is designed to simulate laser-matter interaction in vacuum conditions for a single laser pulse of ns duration and over a broad range of fluence values, spanning from the ablation threshold up to several tens of J/cm^2. Unlike the previous validation steps, the model introduced here includes material removal mechanisms using a dynamical mesh deformation, which is discussed in Subsection 4.2.2.
Although the dynamics of vaporized material and plasma generation are not explicitly modeled, the shielding effect of the plasma plume is taken into account by introducing an exponential attenuation factor, discussed in Subsection 4.2.3.
After the underlying assumptions and governing equations were introduced, the details about the experimental activity concerning ns laser ablation of tungsten and silicon are presented in Subsection 4.2.4, while validation results are discussed in Subsections 4.2.5 and 4.2.6 for tungsten and silicon respectively.

4.2.1 Model assumptions and boundary conditions

Since a fully comprehensive description of all the physical processes involved in laser ablation would be extremely complex and computationally demanding, some simplifying assumptions were introduced in order to retain only the most relevant aspects for the present study.

1) Because an exact experimental measurement of the laser beam profile was not available, a circular Gaussian spatial distribution was assumed. Consequently, the model was developed in a 2D axisymmetric geometry using cylindrical coordinates (r, z).

2) Heat dissipation via natural convection was neglected due to vacuum conditions under which the laser ablation experiments were performed.

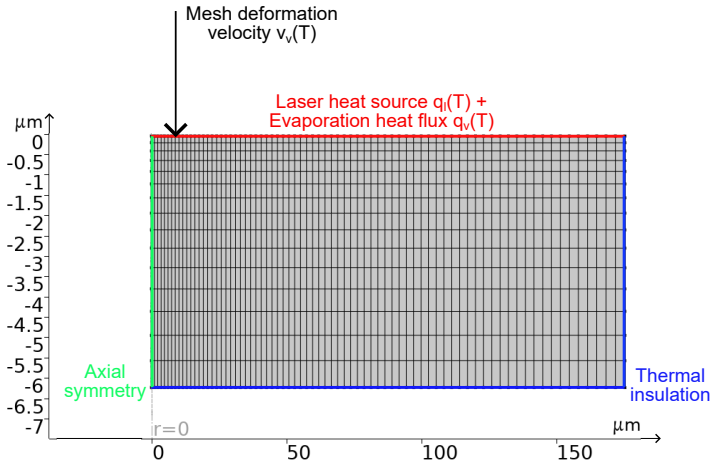

Figure 4.6: 2D mesh used in the simulations. Boundary conditions applied are highlighted with different colors. The domain was approximately 5 µm high and 150 µm wide.

3) Heat losses via thermal radiation were also neglected. Considering a maximum temperature of the order of 10 000 K, the radiated power estimated using Stefan-Boltzmann law ($q_{\mathrm{rad}} = \sigma \cdot T^4$, with σ Stefan-Boltzmann constant) is $\sim 5.67 \cdot 10^4\,\mathrm{W/cm^2}$, which is four orders of magnitude lower than the characteristic space-averaged laser intensity employed in these simulations $\sim 4.6 \cdot 10^8\,\mathrm{W/cm^2}$ (considering pulse energy of 1 mJ, pulse duration of 10 ns, and a spot diameter of $\sim 150\,\mu\mathrm{m}$). For this reason, radiative heat losses can be considered negligible in comparison to laser heating.

4) Considering room-temperature thermophysical properties of W and Si, the computed thermal diffusion length $l_{\mathrm{th}} \approx 3\,\mu\mathrm{m}$, while the optical absorption lengths $l_{\alpha,\mathrm{Si}} \approx 0.013\,\mu\mathrm{m}$ for a wide temperature interval [81] and $l_{\alpha,\mathrm{W}} \approx 0.023\,\mu\mathrm{m}$ [82], which are significantly smaller than l_{th}. As a consequence, the laser heat source was implemented as a superficial heat flux q_{l}, neglecting volumetric absorption effects [83].

5) Temperature dependence of density, isobaric heat capacity, thermal conductivity, and surface reflectivity was incorporated in the model using data available in literature. The corresponding values and references are reported in Tables 4.1 and 4.2.

6) The solid-liquid phase transition was included exploiting the phase change material subnode in COMSOL, as discussed in Subsection 4.1.3.

A schematic representation of the computational domain with boundary condition is shown in Figure 4.6. The total domain has a height of approximately

6 µm and a width around 150 µm. The mesh, chosen after a sensitivity analysis, consists of 1125 rectangular elements, with 15 elements along the vertical direction and 75 elements along the horizontal direction. To improve resolution in the region characterized by higher laser power and temperature gradients, a non-uniform mesh was employed, with element size ratios of 1:3 in the radial direction and 1:4 in the vertical direction. As a result, the bottom-right element is 3 times wider and 4 times higher than the top-left element.
Material removal due to ablation was simulated exploiting the deformed geometry module, by applying a downward deformation velocity on the upper surface; its mathematical expression depends on the ablation regime assumed, and is discussed in Subsection 4.2.2. In this configuration, the term Q in (4.1) is set to zero, since the laser energy deposition is introduced as a boundary heat flux acting on the upper surface (highlighted in red in Figure 4.6):

$$q_l(r, z = 0, t) = (1 - R(T)) \cdot I_0(r, t), \tag{4.5}$$

where $I_0(r, t)$ is given by Equation (4.3). In addition, an evaporation cooling flux $q_v(T)$ was included to account for the energy losses associated with vaporization:

$$q_v(T) \approx \rho(T) v_v(T) L_v, \tag{4.6}$$

where $v_v(T)$ is the surface deformation velocity.
Finally, due to assumptions 1), 2), and 3), right and bottom boundaries of the domain can be considered thermally insulated, while an axial symmetry boundary condition is applied along the left boundary.

4.2.2 Material removal mechanisms

Within the ns laser ablation modeling framework, two primary mechanisms are relevant for material removal: normal evaporation and phase explosion, as previously discussed in 2.1.5. The dominant removal mechanism depends on laser parameters, material thermophysical properties, and focusing conditions (which determine the fluence delivered to the target [84]).
In the present model the dominant phenomenon is selected according to the experimental scenario under investigation. This choice directly determines the mathematical expression adopted for the mesh deformation velocity $v_v(T)$. In the following paragraphs, the two approaches implemented in the model are explained.

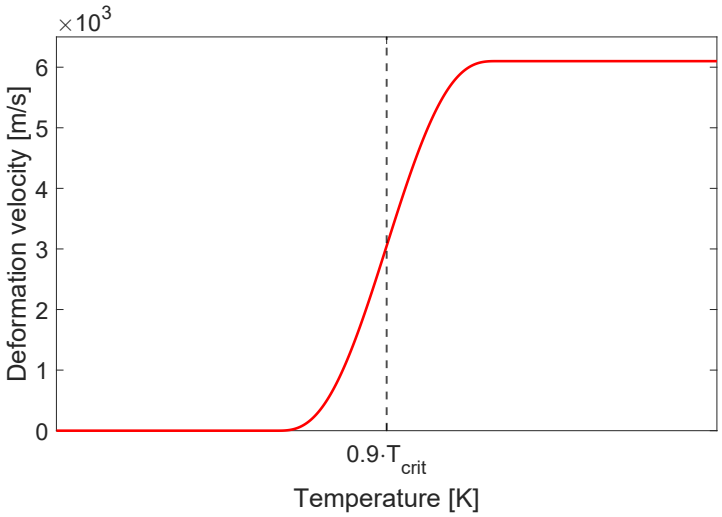

Figure 4.7: Deformation velocity as a function of temperature for the phase explosion regime.

Normal evaporation

For ns laser pulses, normal evaporation is expected to dominate below a characteristic fluence threshold, typically of the order of several J/cm^2, although the exact value depends on the material properties and irradiation conditions. In this regime, surface recession is driven by thermal evaporation process; the deformation velocity can be computed using the Hertz-Knudsen equation:

$$v_v = \frac{p_{\mathrm{sat}}(T)}{\rho(T)} \cdot \sqrt{\frac{M}{2\pi R_{\mathrm{g}} T}}, \tag{4.7}$$

where M is the molar mass of the material and R_{g} is the universal gas constant. The saturation vapor pressure $p_{\mathrm{sat}}(T)$ is calculated using the Clausius-Clapeyron relation:

$$p_{\mathrm{sat}}(T) = p_{\mathrm{atm}} \cdot \exp\left[\frac{M L_v}{R_{\mathrm{g}}}\left(\frac{1}{T_v} - \frac{1}{T}\right)\right], \tag{4.8}$$

where p_{atm} is the atmospheric pressure.
In the simulations, this expression is applied as long as the surface temperature is below the threshold for phase explosion.

Phase explosion

When the incident fluence exceeds the threshold associated with normal evaporation, phase explosion becomes the dominant material removal mechanism. In this regime, the material reaches a metastable superheated state and explosive boiling occurs as a consequence of a sudden increase in the homogeneous nucleation when the temperature approaches the thermodynamic critical temperature T_{crit}.
In the present model, phase explosion was assumed to occur when the surface temperature approaches approximately $0.9 \cdot T_{\text{crit}}$. To simulate the violent and rapid nature of material removal in this regime, the deformation velocity was implemented as a continuous function of temperature, rapidly increasing from zero to the speed of sound in solids ($\approx 6100\,\text{m/s}$) when $T \approx 0.9 \cdot T_{\text{crit}}$ [64]. The deformation velocity function is illustrated in Figure 4.7.
This phenomenological approach allows reproducing the sharp increase of ablation rate observed experimentally at high fluence values, maintaining numerical stability and compatibility with the dynamic mesh deformation strategy adopted.

4.2.3 Plasma shielding

Considering laser intensity attenuation due to plasma shielding is fundamental to correctly quantify the energy delivered to the sample. The explicit simulation of vaporized material and plasma dynamics was out of the scope of this work; however, the shielding effect was included by introducing a shielded intensity $I(r,t)$ (instead of the unshielded $I_0(r,t)$) as the boundary condition on the upper surface.
The shielded intensity is computed as [60]:

$$I(r,t) = I_0(r,t) \cdot \exp\left[-\Lambda(r,t)\right], \tag{4.9}$$

where $\Lambda(r,t)$ is the optical thickness of the plume. This quantity can be expressed as a function of the ablation depth Δz and the fraction of energy density absorbed by the plume E_{a} [85]:

$$\Lambda(r,t) = a\Delta z(r,t) + bE_{\text{a}}(r,t), \tag{4.10}$$

where a and b are time-independent coefficients treated as fitting parameters.
The energy density absorbed by the plume can be expressed as a function of I_0 and Λ [85] and then substituted into Equation (4.10). By differentiating Equations (4.9) and (4.10) and solving the resulting system for I, it is possible to derive

a differential equation governing the temporal evolution of the shielded intensity. Considering that the radial dependencies are embedded in the boundary conditions, the problem can be reduced to an ODE for $I(t)$. By explicitly writing the temporal Gaussian dependence as $G(t)$, the equation can be written as:

$$\frac{1}{I}\frac{\mathrm{d}I}{\mathrm{d}t} = \frac{1}{G}\frac{\mathrm{d}G}{dt} - a\frac{\mathrm{d}\Delta z}{\mathrm{d}t} - b\left(\frac{2E}{\pi r_0^2 \tau}G - I\right). \tag{4.11}$$

This equation was implemented in COMSOL and coupled with the heat transfer problem in order to compute the shielded laser intensity at each time instant.
In the present model, the coefficients a and b are tuned by fitting experimental data and simulation results for the volume ablated by the laser; experimentally, this volume was computed from crater measurement as the numerical integral of the crater shape, while in COMSOL it can be directly evaluated at the end of each simulation. The fitting procedure was carried out in two steps. First, one data point close to the lowest energy available energy was matched by imposing $b = 0$ and determining a suitable value for a. Then, the second coefficient b was obtained by applying the same fitting procedure to one data point near the highest energy value [85]. Finally, the coefficients determined with this procedure were used for simulations across the entire energy range.

4.2.4 Experimental

Laser ablation experiments were carried out on tungsten and silicon samples. Tungsten samples had a square surface with lateral dimensions of 12 mm $\times$ 12 mm and a thickness of 1 mm. They were mechanically polished on both sides, reaching a surface roughness of $R_a \approx 200$ nm. Silicon samples were obtained from a monocrystalline wafer, N-doped with antimony and oriented along the $\langle 100 \rangle$ crystallographic direction. They had the same lateral dimensions as tungsten, but with a lower thickness (380 µm) and a significantly lower surface roughness ($R_a \leq 1$ nm).
The experimental layout is illustrated in Figure 4.8(a). A Quanta System Nd:YAG laser was used, emitting pulses with a duration of 10 ns at a wavelength of 1064 nm. The optical path consisted of three mirrors, a variable attenuator used to regulate the pulse energy delivered to the sample, and a converging lens with focal length $f = 250$ mm. Since the laser operated at a fixed repetition rate of 10 Hz, a fast mechanical shutter was employed to actively control the number of laser pulses impinging on each position.
The samples were placed in a low-pressure chamber, evacuated down to a pressure of approximately 10^{-2} mbar in order to minimize redeposition of vaporized material. A photograph of the final part of the optical path, including the me-

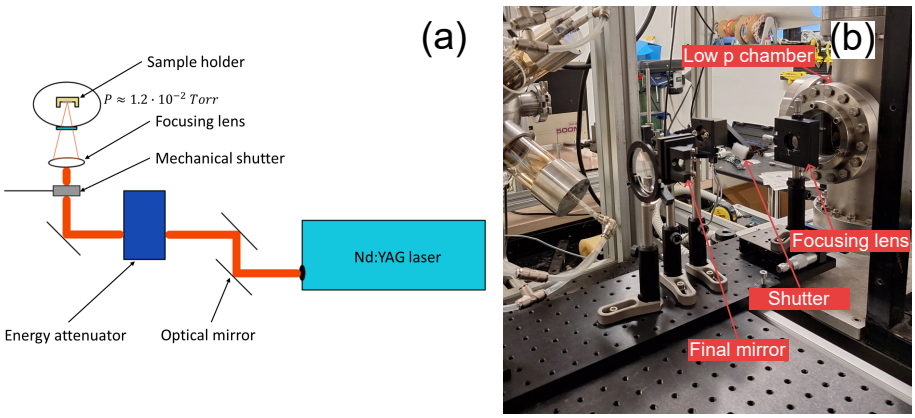

Figure 4.8: Experimental layout and optical path (a); picture of the focusing setup (b).

chanical shutter and the vacuum chamber, is illustrated in Figure 4.8(b). The pulse energy was measured using a power meter positioned immediately before the optical chamber; consequently, the actual energy delivered to the sample surface was reduced by approximately 10% due to optical losses.
The sample was mounted on a movable translation stage, allowing motion in the plane orthogonal to the beam propagation direction and enabling the generation of multiple craters on the same surface. The laser spot diameter on the sample was estimated from the width of the silicon craters, yielding values in the range $140\,\mu m - 200\,\mu m$. However, since differences in crater shape were observed, especially between tungsten and silicon irradiation, this parameter is discussed in more detail in the following sections.
The experimental campaign was divided into two separated parts. The first campaign focused on W irradiation at low pulse energies, ranging from 0.4 mJ to 2 mJ, in order to achieve shallow ablation depths. Due to the high surface roughness and high ablation threshold of W, craters were generated using 10 consecutive pulses. The average crater depth and ablated volume per pulse were obtained by dividing the total measured values by the number of pulses. The second experimental campaign was carried out on Si, using pulse energies from 4 mJ to 20 mJ, with the objective of exploring a broader range of fluence to assess and extend the range of validity of the model. Due to the lower roughness and ablation threshold of Si, which allow for easily detectable craters, single-pulse measurements were performed. This fact allowed a more direct comparison with the numerical model, which explicitly describes single-pulse laser-material interaction.
Ablation crater morphology was first inspected by optical microscopy and SEM (Hi-res SEM, Tescan mod. MIRA III, Brno, Czech Republic) operating at an

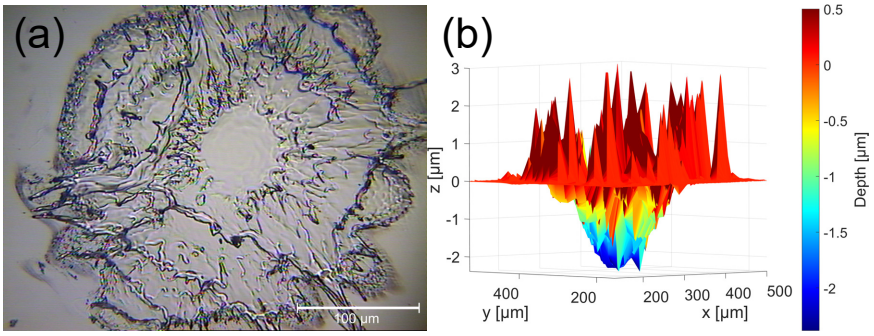

Figure 4.9: Optical microscope image (a) and 3D reconstruction from surface profiler (b) of single-pulse crater on silicon ($E = 20\,\text{mJ}$).

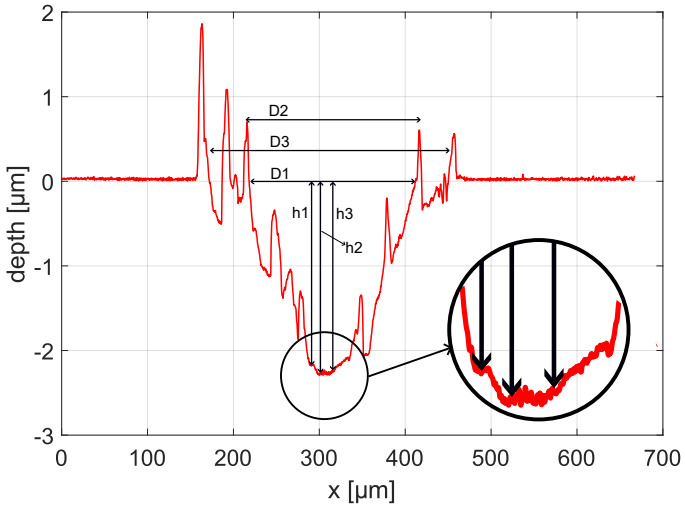

Figure 4.10: 2D central slice of the 3D reconstruction shown in Figure 4.9. The different distances considered for depth (hi) and diameter (Di) are indicated.

accelerating voltage of 20 kV. A full 3D surface reconstruction of the craters was obtained using a surface profiler (KLA-Tencor P-15, Milpitas, California, USA), featuring a vertical resolution of approximately 10 nm. The 3D profiles were generated by acquiring a series of 30 horizontal 2D line scans, spaced by $10 - 20\,\mu\text{m}$. Each scan was performed with a probe speed of $50\,\mu\text{m/s}$ and a sampling rate of 500 Hz, resulting in a lateral spatial resolution of $0.25\,\mu\text{m}$. An example of an optical microscope image and corresponding 3D crater reconstruction on Si sample irradiated at $E = 20\,\text{mJ}$ is shown in Figure 4.9.

The experimental ablated volume was calculated through a numerical integration procedure, obtaining a maximum relative uncertainty of 0.37% for W and 0.04% for Si. For a reliable estimation of the maximum crater depth, the horizon-

tal 2D scan passing through the crater center was considered. The depth value was computed as the average between the lowest point (h2) and the two nearest local minima (h1 and h3) [71], as represented in Figure 4.10.
To estimate the average crater diameter and its associated uncertainty, three different width definitions were considered from the central scan, as illustrated in Figure 4.10. The first estimation D1 was defined taking as edges the intersection points between crater profile and the $z = 0$ line. The second diameter D2 was obtained using the local maxima adjacent to intersection points. Finally, the third diameter D3 included secondary depression when their depth is sufficiently significant. These definitions allow a consistent and robust characterization of crater geometry for different fluence conditions.

4.2.5 Results for tungsten ablation

Finite element simulations were first performed considering tungsten as the irradiated material. Tungsten is one of the most relevant PFCs for fusion applications and is characterized by high melting temperature and ablation threshold under ns irradiation. The experiments were focused on low pulse energies, from 0.4 mJ to 2 mJ, with increasing steps of 0.4 mJ.
Figure 4.11 shows SEM images of tungsten ablation craters, where (a) and (b) represent the crater obtained at the lowest energy considered, while (c) and (d) represent the crater obtained at the highest energy.
At the lowest energy (Figure 4.11a), the crater appears as a small and approximately circular depression, indicating that only the central high-intensity region of the laser spot exceeded the ablation threshold. At the highest energy (Figure 4.11c), a larger modified area is observed, characterized by the presence of ripple-like rings extending from the center. The crater shape becomes more elliptical, suggesting a deviation from the ideal circular Gaussian profile.
High-magnification images reveal additional morphological features. At the lowest energy (Figure 4.11b), the crater surface exhibits the presence of small secondary depressions, which may originate from metal vapor release during melting or from shrinking effect associated with density differences between solid and liquid phases [86]. At the highest energy (4.11d), the morphology is different, showing recrystallization traces in the crater middle, accompanied by cracks and resolidified material near the border. However, in both images, there is no evidence of elongated droplets or particulate ejection typically associated with phase explosion. Based on these observations, normal evaporation was assumed as the dominant material removal mechanism for W in the investigated energy range.
The Thermophysical and optical properties of W are reported in Table 4.1. When

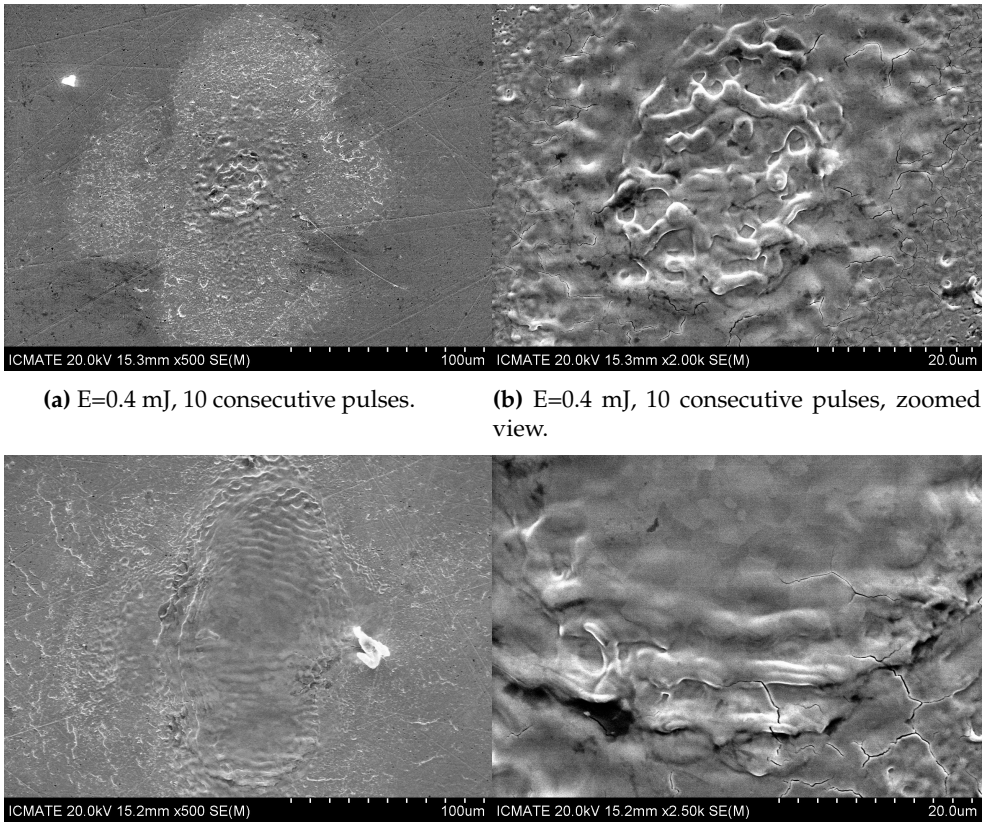

(a) E=0.4 mJ, 10 consecutive pulses.

(b) E=0.4 mJ, 10 consecutive pulses, zoomed view.

(c) E=2 mJ, 10 consecutive pulses.

(d) E=2 mJ, 10 consecutive pulses, zoomed view.

Figure 4.11: Images of ablation craters on W obtained with SEM.

data were not available over the full temperature range of interest, properties were kept constant beyond the available limits in order to avoid unphysical behavior. In particular, the surface reflectivity R was interpolated up to 3683 K and then fixed at a constant value for higher temperatures.

Simulations were performed assuming a laser pulse duration of $\tau = 10\,\text{ns}$, with peak intensity occurring after $t_0 = 20\,\text{ns}$, to ensure that the full temporal evolution of the pulse is included. In order to account for optical losses in the experimental setup, a 10% reduction of the nominal pulse energy was applied in all simulations.

Due to the elliptical shape of experimental craters, an additional assumption was required to preserve the axial symmetry of the numerical model. As shown in the top-view reconstruction presented in Figure 4.12, the ablation crater generated at $E = 2\,\text{mJ}$ is composed of a circular central spot accompanied by two smaller secondary depressions located above and below the main crater. This shape may

Parameter	Value	validity range
L_m [kJ/mol]	52.3	
L_v [kJ/mol]	824	
T_m [K]	3695	
T_v [K]	6203	
T_{crit} [K]	16000	
ρ [kg/m^3]	$19.25 - 2.626 \cdot 10^{-4} \cdot (T - T_0) - 3.060 \cdot 10^{-9} \cdot (T - T_0)^2 - 9.519 \cdot 10^{-14} \cdot (T - T_0)^3$	$300\,\text{K} < T \leq T_m$
	$16.27 - 7.679 \cdot 10^{-4} \cdot (T - T_m) - 8.091 \cdot 10^{-8} \cdot (T - T_m)^2$	$T_m < T \leq 6000\,\text{K}$
C_p [J/(mol · K)]	$21.87 + 8.07 \cdot 10^{-3} \cdot T - 3.76 \cdot 10^{-6} \cdot T^2 + 1.08 \cdot 10^{-9} \cdot T^3 + 1.41 \cdot 10^{7} \cdot T^{-2}$	$300\,\text{K} < T \leq 3080\,\text{K}$
	$2.022 + 1.315 \cdot 10^{-3} \cdot T$	$3080\,\text{K} < T \leq T_m$
	51.3	$T_m < T \leq 6000\,\text{K}$
k [W/(m · K)]	$149.4 - 45.47 \cdot 10^{-3} \cdot T + 13.19 \cdot 10^{-6} \cdot T^2 - 1.484 \cdot 10^{-9} \cdot T^3 + 3.866 \cdot 10^{-13} \cdot T^{-2}$	$300\,\text{K} < T \leq T_m$
	$66.6212 + 0.02086 \cdot (T - T_m) - 3.7585 \cdot 10^{-6} \cdot (T - T_m)^2$	$T_m < T \leq 6000\,\text{K}$
R	0.607	$T = 400\,\text{K}$
	0.617	$T = 1000\,\text{K}$
	0.632	$T = 2000\,\text{K}$
	0.647	$T = 3000\,\text{K}$
	0.657	$T = 3683\,\text{K}$

Table 4.1: Thermophysical and optical properties of W used in the simulations [87, 88, 89, 90, 91].

have been caused by a slight misalignment of the optical path and the non-ideal Gaussian distribution, an effect amplified by the high ablation threshold of W. Assuming that crater shape is similar to the actual pulse spatial distribution only the central crater was considered for comparison with simulations.
The effective energy fraction of laser energy contributing to the central crater generation was estimated as:

$$E_{\text{fraction}} = \frac{V_{\text{central crater}}}{V_{\text{total crater}}} \cdot E_{\text{total}}, \tag{4.12}$$

where $V_{\text{central crater}}$ and $V_{\text{total crater}}$ are the volumes of the central and total crater, respectively. This analysis resulted in an effective energy fraction of approximately 0.55. Accordingly, a Gaussian distribution with $D = 2 \cdot r_0$ of 80 µm was

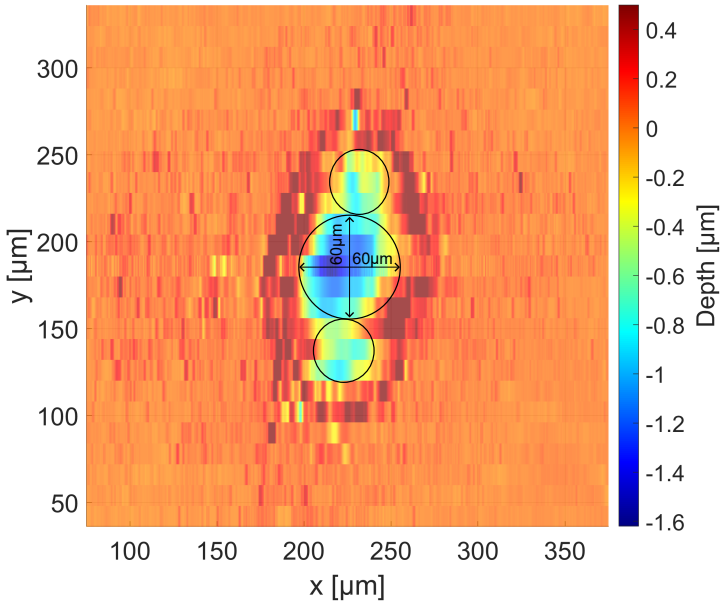

Figure 4.12: Top view of 2 mJ tungsten crater produced by 10 pulses reconstructed using surface profiler.

assumed in the simulations; this value is slightly larger than the measured crater size, accounting for the fact that the ablation threshold of W corresponds to an intensity higher than that at $r = r_0$ for low intensity conditions. With these assumptions, a fluence range of $\sim 4 - 20\,\mathrm{J/cm^2}$ was considered.
Figure 4.13 illustrates the temporal evolution of the maximum surface temperature for all the energy values. Peak temperatures range from 11 000 K to 14 000 K, exceeding the boiling temperature but remaining below the phase explosion threshold ($0.9 \cdot T_{crit} \approx 14\,400$ K). This confirms the consistency of the normal evaporation approach for W under the investigated conditions.
Figure 4.14 compares the experimental and simulated ablated volumes as a function of pulse energy, considering the central crater only. Due to the very low relative uncertainty (maximum value of 0.37%) error bars are not visible in the plot. As discussed in Subsection 4.2.3 plasma shielding coefficients a and b were determined fitting two experimental data points, one near the lowest energy (0.8 mJ) and one near the highest energy (2 mJ), resulting in the values $a = 85\,000\,\mathrm{cm^{-1}}$ and $b = 0.09\,\mathrm{cm^2/J}$. The model reproduces the overall trend of ablated volume with energy, with a maximum relative discrepancy of 48% at 1.2 mJ. The underestimation observed for higher energies may indicate a slight overestimation of plasma shielding effect.

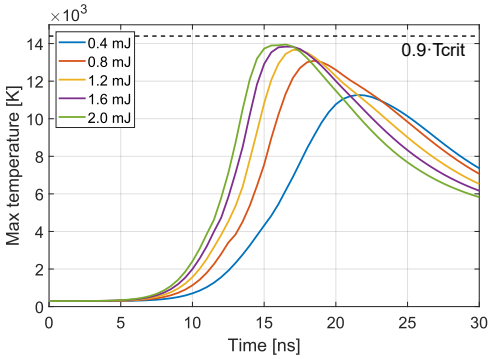

Figure 4.13: Evolution of maximum surface temperature for the different values of the total pulse energy. The phase explosion threshold is indicated with a dashed line.

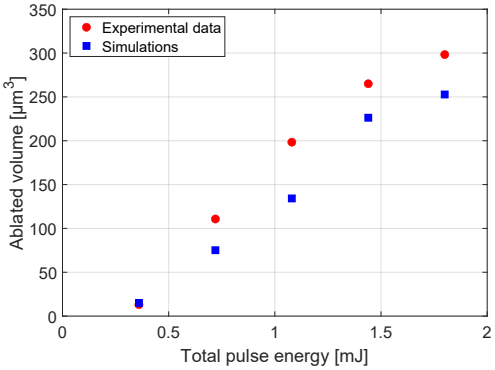

Figure 4.14: Comparison between computational and experimental results for the ablated volume of tungsten.

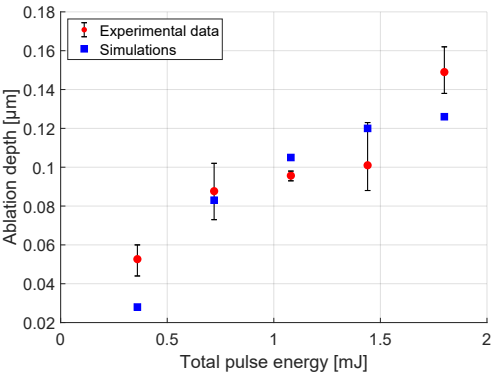

Figure 4.15: Comparison between computational and experimental results for the ablation rate of tungsten.

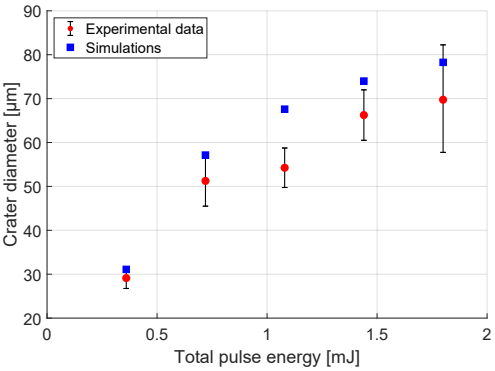

Figure 4.16: Comparison between computational and experimental results for the ablation crater diameter of tungsten.

Figure 4.15 shows the comparison between experimental and simulated ablation depth. A good agreement is obtained for most of the energy values, with a relative discrepancy below 20% except for the lowest energy case, where the discrepancy is approximately 47%; despite this, the corresponding absolute difference is the smallest compared to the other points, being $\sim$ 20 nm. This confirms that the model is able to predict depth of single-pulse ablation crater. Figure 4.16 presents the comparison between the computed crater diameter and the experimental one, considering the central region only. Although the computed values slightly overestimate the experimental measurements, the overall trend is well reproduced with a relative discrepancy always below 25%. This result further confirms the validity of the modeling assumptions adopted for W

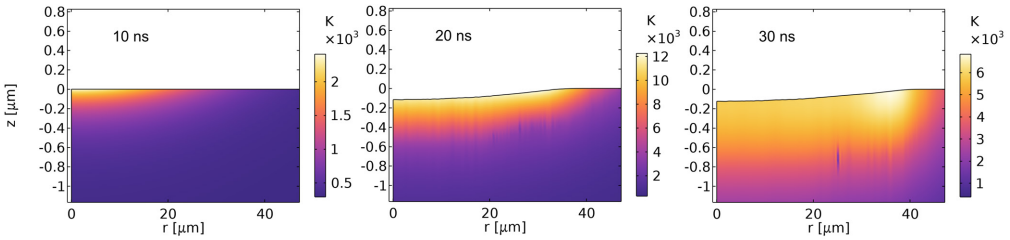

Figure 4.17: Temperature and domain evolution for $E = 2$ mJ. The simulation domain, due to the axial symmetry assumption, represents only half of the ablation crater. The temperature scale is reported in the colorbar on the right.

in the investigated conditions.
Finally, Figure 4.17 shows the temperature field evolution over a significant portion of the computational domain for the maximum energy value ($E = 2$ mJ). Three different time instants are reported: 10 ns, 20 ns, and 30 ns, corresponding respectively to $t_0 - \tau$, t, and $t_0 + \tau$. At 10 ns, the temperature rise has already started, but ablation and melting have not yet occurred. At 20 ns, corresponding to the laser intensity peak, surface recession becomes significant, with the maximum temperature exceeding the boiling point. At the final time instant, the material has entered the cooling phase: while the heat is still diffusing into the bulk, the temperature field highlights the high spatial extension of the HAZ. Although material removal has almost ceased, the molten region is extending down to ~ 0.8 µm, corresponding to nearly 700 nm below the crater bottom.
As a final remark, it is important to underline that heat diffusion time estimated as $t_{diff} \sim l_{th}^2/(4 \cdot D_{th})$ is ~ 5 ms in this case; this value is about twenty times shorter than the laser pulse period $1/RR = 100$ ms. For this reason, thermal influence between two consecutive pulses can be safely neglected.

4.2.6 Results for silicon ablation

A further set of simulations was performed considering silicon irradiation, with pulse energy ranging from 4 mJ to 20 mJ in steps of 2 mJ. Silicon was selected not only for its low surface roughness, which facilitates accurate crater characterization, but also because of its different thermophysical properties compared to tungsten, especially T_m and T_v. This makes silicon an effective test material to further assess the applicability and robustness of the model.
Figure 4.18 shows SEM images of a single-pulse crater obtained for the lowest energy available (4 mJ). In the low-magnification image (Figure 4.18a) an irregular but approximately circular shape can be observed, characterized by pronounced and irregular rims. In the high-magnification image (Figure 4.18b) details of the crater edge reveal the presence of re-solidified droplets and ejected particulates.

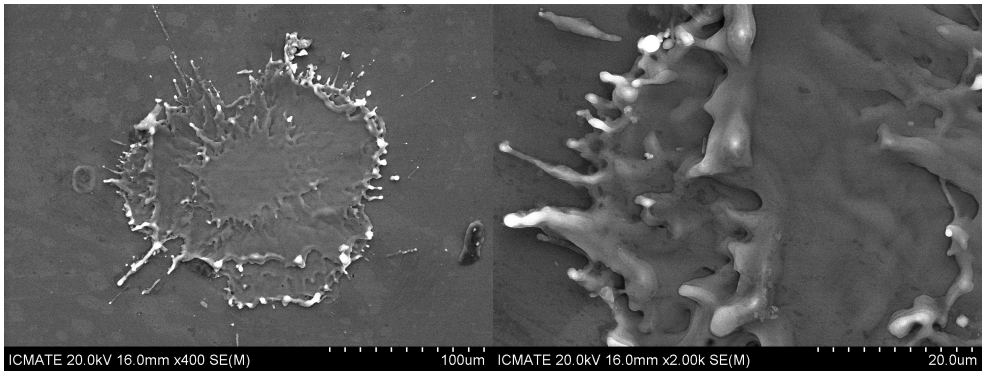

(a) $E = 4\,\text{mJ}$, single pulse. **(b)** $E = 4\,\text{mJ}$, single pulse, zoomed view.

Figure 4.18: Images of an ablation crater on Si obtained with SEM.

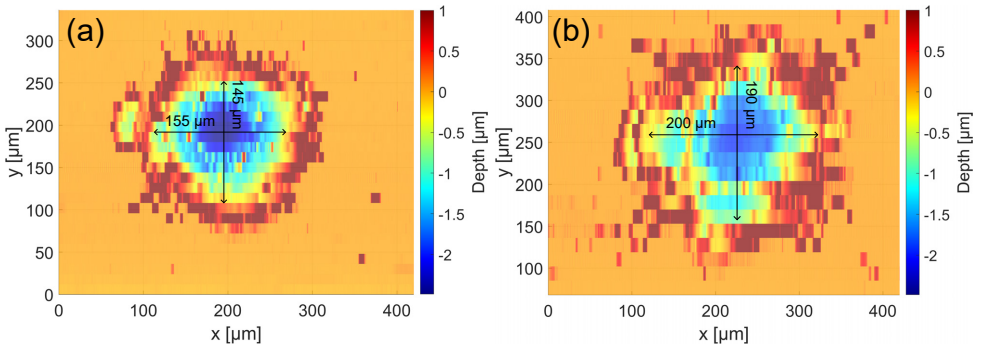

Figure 4.19: Top view of single-pulse ablation craters on silicon for $E = 10\,\text{mJ}$ (a) and 12 mJ (b).

The crater morphology differs markedly from that observed for W and indicates a more violent material removal process. Based on these observations, phase explosion was assumed as the dominant material removal mechanism for Si under the investigated conditions.

The thermophysical and optical properties of Si adopted in the simulations are reported in Table 4.2. The same laser parameters used for W simulations were retained, with the exception of the pulse energy range. As in the W case, a 10% energy reduction of the nominal pulse energy was applied to account for losses due to the optical window.

To estimate the laser spot diameter, the crater shape was analyzed for all the energy values. Microscopy observations and surface profiler reconstructions confirmed that all the Si craters are approximately circular over the entire energy range, so the central crater assumption used for W was not required. However, a noticeable size difference was observed when comparing craters produced at energies below and above 10 mJ. This effect can be observed from Figure

Parameter	Value	Validity range
L_m [J/kg]	$1.41 \cdot 10^6$	
L_v [J/kg]	$1.36 \cdot 10^7$	
T_m [K]	1687	
T_v [K]	3538	
T_{crit} [K]	5160	
ρ [kg/m^3]	2320	$T \leq T_m$
	2520	$T > T_m$
C_p [J/(mol · K)]	$694 \cdot \exp(2.375 \cdot 10^{-4} \cdot T)$	$T \leq T_m$
	1050	$T > T_m$
k [W/(m · K)]	$1.52 \cdot 10^5 \cdot T^{-1.226}$	$T \leq 1200\,\text{K}$
	$898 \cdot T^{-0.52}$	$1200\,\text{K} < T \leq T_m$
	$50 + 0.029 \cdot (T - T_m)$	$T \geq T_m$
R	$0.3 + 5 \cdot 10^{-5} \cdot (T - 300)$	$T \leq T_m$
	0.79	$T > T_m$

Table 4.2: Thermophysical properties of silicon used in the simulations [92, 93, 94, 61].

4.19, where top-view reconstructions of craters obtained at 10 mJ and 12 mJ are compared, showing an increase in diameter of nearly 50 µm considering the higher energy value. This discrepancy was likely caused by a small displacement of the converging lens during the experimental campaign, resulting in a broader spot size for energies above 12 mJ. To account for this effect, two different sets of simulations were performed: the first assuming a constant laser spot diameter of 200 µm over the entire energy range, corresponding to a fluence range of $\sim 12 - 60\,\text{J/cm}^2$; the second set assumed a smaller spot size of 140 µm for $E \leq 10$ mJ, leading to a fluence range of $\sim 25 - 60\,\text{J/cm}^2$.

Figure 4.20 shows the temporal evolution of the maximum surface temperature for the lowest energy analyzed ($E = 4$ mJ) and assuming a spot diameter $D = 200$ µm; results obtained using normal evaporation and phase explosion approaches are compared. In the phase explosion case, the temperature always remains below the threshold value of $0.9 \cdot T_{crit}$ (4644 K), whereas this limit is exceeded using normal evaporation approach. This confirms that the phase explosion approach provides a more physically consistent description of Si ablation under these irradiation conditions.

Figure 4.21 compares the experimental and simulated results for the ablated volume, highlighting the two sets of simulations with different colors and indicators. As for W, experimental uncertainties are very small and error bars are not visible in the plot. Plasma shielding coefficients were evaluated using the fitting procedure described in 4.2.3. For the simulations with $D = 200$ µm, the fitted

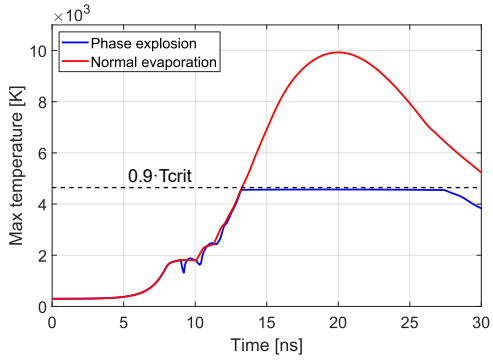

Figure 4.20: Evolution of maximum surface temperature for $E = 4\,\text{mJ}$ for the two material removal mechanisms. The same settings for the plasma shielding have been considered. The phase explosion threshold is indicated with a dashed line.

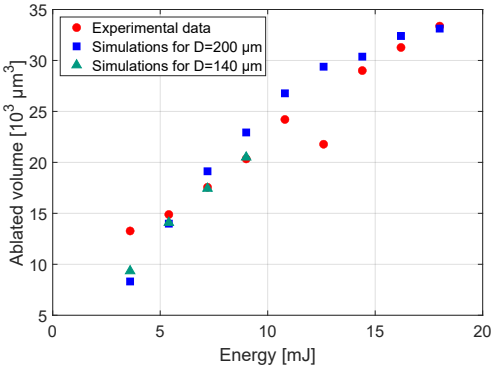

Figure 4.21: Comparison between computational and experimental results for the ablated volume of silicon.

values were $a = 2600\,\text{cm}^{-1}$ and $b = 0.0425\,\text{cm}^2/\text{J}$. Due to the higher fluence for the same energy associated with the smaller spot diameter, coefficients were tuned separately for the $D = 140\,\mu\text{m}$ case, obtaining the values $a = 4500\,\text{cm}^{-1}$ and $b = 0.013\,\text{cm}^2/\text{J}$. These values are much lower than those obtained for W, reflecting the different ablation velocities and temporal intensity profiles.

Simulations performed using $D = 200\,\mu\text{m}$ show good agreement considering the ablated volumes, particularly at higher energies ($\geq 12\,\text{mJ}$). At lower energies, agreement improves significantly when the smaller spot diameter ($140\,\mu\text{m}$) is used, with simulated points moving closer to experimental data.

Figure 4.22 illustrates the comparison between experimental and simulated ablation depth as a function of pulse energy. When a constant spot diameter of $200\,\mu\text{m}$ is assumed, numerical results reproduce experimental depth with a discrepancy below 20% only for the last five energy values (above 10 mJ), while a big underestimation is observed for the lower energies. The experimental data exhibit a non-monotonic behavior, with a decrease in ablation depth above 10 mJ. This trend cannot be reproduced adopting a constant spot size for all the energies, but is consistent with a diameter reduction below 12 mJ. Indeed, when a D of $140\,\mu\text{m}$ is adopted for energies up to 10 mJ, the corresponding increase in fluence leads to higher simulated ablation depths improving the agreement with experimental results. As a consequence, the relative discrepancy for the lower energies is reduced from a maximum value around 55% to below 25%.

Figures 4.23 shows the comparison between experimental and simulated crater diameter. These results further confirm the improved agreement when a smaller

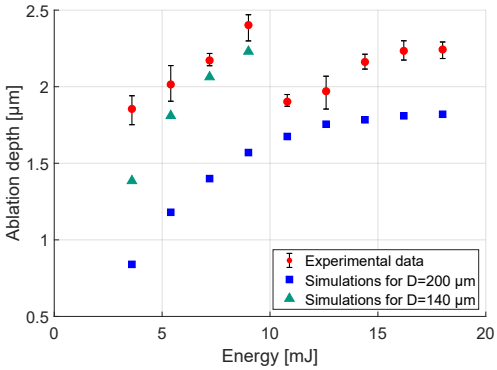

Figure 4.22: Comparison between computational and experimental results for the ablation rate of silicon. An anomalous decrease of the experimental depth can be observed above 10 mJ.

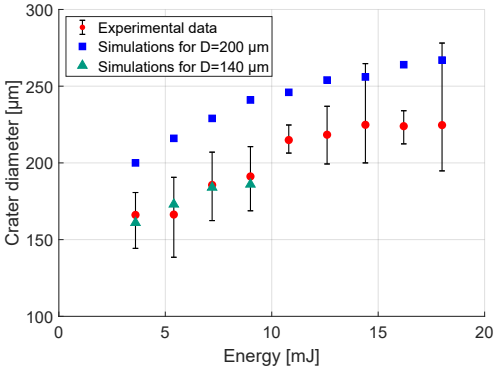

Figure 4.23: Comparison between computational and experimental results for the ablation crater diameter of silicon.

spot diameter is considered for $E \leq 10$ mJ: the relative discrepancy decreases from $20-25\%$ down to 5% when $D = 140$ μm is used and the overall trend with laser pulse energy is correctly reproduced. These results support the interpretation that a small variation in focusing conditions can affect the ablation behavior and must be taken into account for a consistent comparison with experiments.
Finally, Figure 4.24 shows the simulated geometry and T field evolution for the lowest and the highest energy values (4 mJ (a) and 20 mJ (b)), assuming a D of 140 μm and of 200 μm, respectively. The same three time instants shown in Subsection 4.2.5 were considered. In both cases similar considerations apply: at $t = 10$ ns material removal has not yet started, although the maximum temperature has already exceeded the melting point for both energies. At $t = 20$ ns, the formation of the crater becomes evident, with the maximum surface temperature remaining below the imposed phase explosion threshold (4644 K). At the final time instant $t = 30$ ns, the craters are fully developed and the surface temperature begins to decrease because of the heat diffusion into the bulk.
As in the W case, the extent of thermal diffusion can be evaluated from the final temperature field by examining the depth of the molten region. Values of approximately 580 nm and 490 nm below the crater bottom are obtained for 20 mJ and 4 mJ, respectively. Due to the lower thermal conductivity of Si, the HAZ is more confined compared to W, resulting in a reduced subsurface thermal extension. It is important to underline that good agreement for ablation crater characteristics was obtained for both tungsten and silicon across a broad fluence range, ensuring the flexibility of the model and its potential applicability to other fusion-relevant materials.

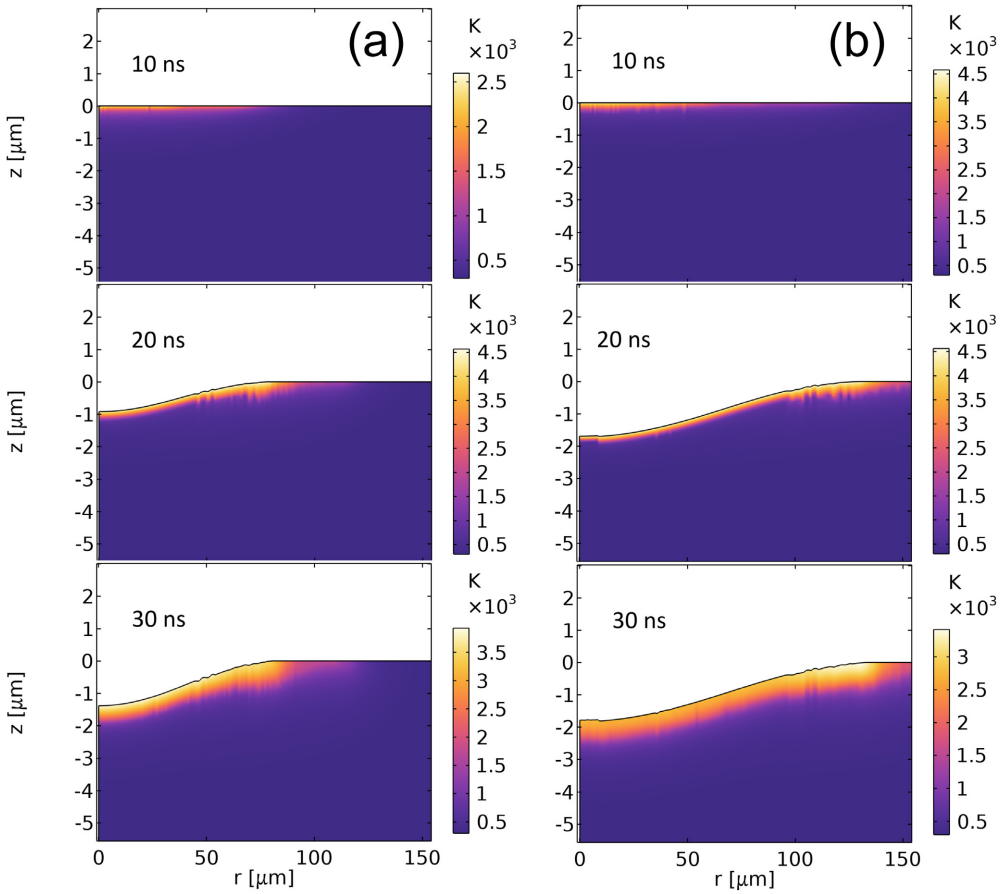

Figure 4.24: Temperature and domain evolution for $E = 4\,\text{mJ}$ (a) and $E = 20\,\text{mJ}$ (b). Each simulation, due to the axial symmetry assumption, shows only half of the ablation crater. The temperature scale is reported in the colorbar on the right.

5 Picosecond laser ablation modeling

In preparation for the LIBS diagnostics that will be installed on the BiGyM linear device, the modeling activity was extended to the ultrashort-pulse regime, considering laser pulses with picosecond duration. In this regime, laser-matter interaction cannot be accurately described using a single-temperature thermal model. Instead, a separate description for electron and lattice heating dynamics is necessary, which is provided by the Two-Temperature Model (TTM).
Section 5.1 is devoted to the introduction of the TTM equations and to the validation of the numerical implementation with the reference results regarding only thermal response available in the literature. In Section 5.2 a complete ablation model for picosecond laser irradiation is introduced. The model includes material removal mechanism and phase transition, and it is validated against experimental results obtained from pulsed laser irradiation of tungsten.

5.1 Two-Temperature Model equations and first validation step

Following a structure similar to that adopted for Chapter 4, the first part of this Section (Subsection 5.1.1) introduces the mathematical formulation used to describe separate heating dynamics for the electron and lattice subsystems. Before implementing the complete ablation model, which includes phase transitions and material removal to simulate crater formation, a preliminary validation of the pure thermal response of the computational model was required.
This validation step was performed by comparing the simulated temperature evolution against reference results reported in the literature for ultrafast laser irradiation of a copper film. The outcome of this benchmark is presented in

Subsection 5.1.2. After validation in the ps regime, the same numerical implementation was applied to a pulse with 10 ns duration, in order to highlight the transition from non-equilibrium electron-lattice heating dynamics to the classical single-temperature behavior.

5.1.1 Governing equations

During ps laser irradiation, pulse energy is initially absorbed by the electron subsystem and subsequently transferred to the lattice through electron-phonon interactions. Since the characteristic electron-phonon relaxation time τ_{e-i} is usually of the order of a few ps, a description based on a single temperature field is no longer adequate. In this framework, the temperature evolution of the material is described by a system of two coupled heat conduction equations [64]:

$$\begin{aligned} C_e \frac{\partial T_e}{\partial t} &= \nabla \cdot (k_e \nabla T_e) - G(T_e - T_l) + Q \\ C_l \frac{\partial T_l}{\partial t} &= \nabla \cdot (k_l \nabla T_l) + G(T_e - T_l) \end{aligned} \tag{5.1}$$

where the subscripts e and l refer to electron and lattice subsystems, respectively. $C_{e,l}$ indicate the volumetric heat capacities [J/(m^{3}K)], $k_{e,l}$ the thermal conductivities, and G the electron-lattice coupling factor [W/(m^{3}K)], which quantifies the strength of energy exchange between the two populations. The laser source term Q can be computed as a volumetric heat source acting on electron subsystem using Equation (4.2). When Gaussian spatial and temporal profiles are assumed, the laser intensity distribution $I_0(r,t)$ can be expressed using Equation (4.3).
For the lattice subsystem, the volumetric heat capacity C_l was computed from the isobaric specific heat C_p[J/(kg K)] as $C_l = C_p \cdot \rho$, where ρ is the mass density. The electron heat capacity and thermal conductivity are usually approximated using linear temperature-dependent expressions [65]:

$$\begin{aligned} C_e &= C_{e0} \cdot T_e \\ k_e &= k_{e0} \cdot \frac{T_e}{T_l}, \end{aligned} \tag{5.2}$$

where C_{e0} and k_{e0} are material-dependent constants. The lattice thermal conductivity k_l typically has a lower magnitude than k_e and therefore plays a less dominant role during ultrafast laser heating. On the other hand, the coupling factor G is known to exhibit a more complex temperature dependence and may significantly deviate from linear behavior especially for higher laser intensities. Temperature-dependent expressions for G can be derived from theoretical models, as discussed in ref. [65].

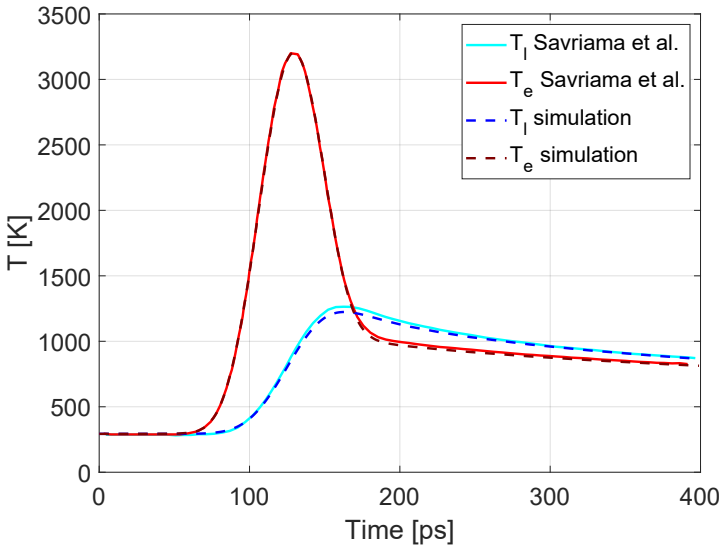

Figure 5.1: Comparison between electron and lattice surface temperature temporal evolution for $F = 190\,\mathrm{mJ/cm^2}$, $\tau = 42\,\mathrm{ps}$.

5.1.2 Model validation with reference results

As a first validation step, the TTM model implementation in COMSOL was benchmarked against the work of Savriama and Semmar [95], who investigated the role of thermal phenomena during the formation of Laser-Induced Periodic Surface Structures (LIPSS) on copper. In the reference study Cu was irradiated with an ultraviolet laser (266 nm, fourth harmonic), with a Gaussian temporal profile characterized by a pulse duration of 42 ps and centered at 146 ps. The laser beam was assumed to exhibit an ideal Gaussian spatial profile, implemented as a volumetric heat source term Q. The fluence was set to approximately $190\,\mathrm{mJ/cm^2}$, i.e., just below the single-shot melting threshold. Since the laser spot size was about three orders of magnitude larger than the optical penetration depth in Cu, the problem was reduced to a 1D model, focusing only on the temperature evolution along the depth direction.
The computational geometry consisted of a 1D Cu domain with a length of 1 µm, intended to mimic a copper film deposited on a substrate. The mesh was defined by the author using a uniform element size of 5 nm. Heat losses by convection and radiation were neglected, as their contributions are negligible compared with the laser power density. Except for k_e and C_e, which were described by the linear relations in (5.2), the other thermophysical properties and the optical absorption coefficient were assumed constant with respect to $T_{e,l}$.
Figure 5.1 compares the temporal evolution on the surface ($x = 0$) obtained in the present simulations with the results reported by Savriama and Semmar

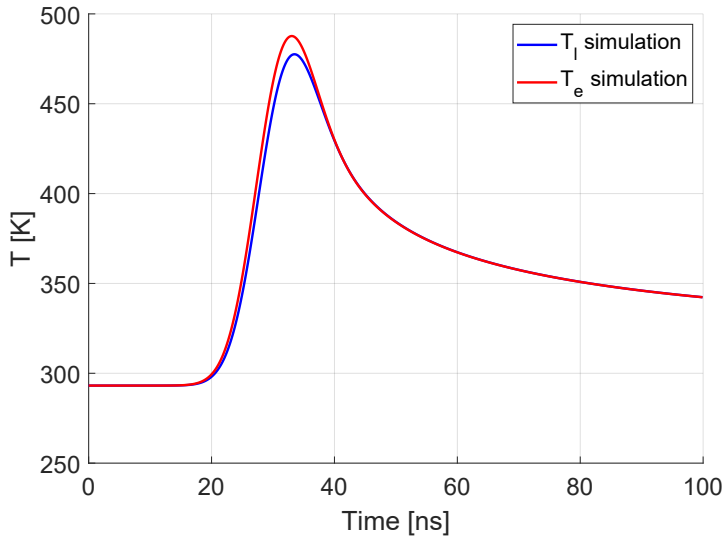

Figure 5.2: Electron and lattice surface temperature evolution for $F = 190\,\mathrm{mJ/cm^2}$, $\tau = 10\,\mathrm{ns}$.

[95]. A pronounced non-equilibrium behavior is observed: T_e rises rapidly and reaches a peak value around 3200 K shortly after the peak arrival time (around $\sim 146\,\mathrm{ps} + 50\,\mathrm{ps}$), whereas T_l increases more gradually reaching a peak value of around 1220 K, which is below the melting temperature of Cu. Moreover, the lattice peak occurs with a delay of roughly 40 ps with respect to the T_e peak. This behavior is consistent with the fact that the characteristic electron-phonon relaxation time in Cu is around 3 ps and is not negligible compared to pulse duration, leading to a temporal shift in temperature peaks of the order of τ.
To highlight the difference between ultrashort and short pulses, the same simulation was repeated by increasing the pulse duration to 10 ns while keeping the same fluence. The computed surface temperature evolution is shown in Figure 5.2. In this case, the computational domain was extended to 10 µm, to account for the larger thermal diffusion length. As expected, T_e and T_l are almost identical over the entire time window. This is coherent with theoretical predictions, confirming that energy transfer from electron-to-lattice is instantaneous for the ns time scale; in this case the temperature evolution can be accurately described using a single heat conduction equation.
In conclusion, this benchmark confirms that the TTM implementation in COMSOL correctly reproduces (i) the non-equilibrium electron-lattice dynamics in ps regime, allowing a detailed analysis of the temperature field evolution, and the convergence (ii) towards the classical single temperature behavior for ns pulses.

5.2 Picosecond laser ablation model and validation for tungsten

In this section, the two-dimensional model developed to simulate picosecond laser ablation is presented. The model is designed to simulate laser-material interaction under low-pressure conditions for a single laser pulse with ps duration.
The main modeling assumptions, the computational domain, and the boundary conditions are introduced in Subsection 5.2.1. The material removal mechanism, which differs from those adopted for ns irradiation, is discussed in Subsection 5.2.2.
Subsequently, the model was validated against experimental results from laser ablation of tungsten samples, using pulses at 1030 nm with 10 ps duration, and an incident fluence varying approximately from $4\,\mathrm{J/cm^2}$ to $12\,\mathrm{J/cm^2}$. The experimental setup and diagnostic techniques are described in Subsection 5.2.3 while modeling results and comparison with experimental data are presented in Subsection 5.2.4.

5.2.1 Model assumptions, geometry and boundary conditions

Based on the ns ablation model described in Chapter 4, some simplifying hypotheses were modified to account for the ultrashort pulse duration and an additional hypothesis regarding the importance of plasma shielding was added. Modified assumptions with respect to the ns model are marked with an asterisk (*).

1*) A measurement of the laser spatial profile was provided by the laser manufacturer. According to the datasheet, the beam exhibits a near-Gaussian profile with an ellipticity $\epsilon = w_{\mathrm{minor}}/w_{\mathrm{major}} \approx 0.95$. For this reason, the model was developed again using a 2D axisymmetric geometry in cylindrical coordinates (r, z).

4*) Due to the laser pulse duration of 10 ps, the thermal diffusion length is significantly reduced for tungsten ($l_{\mathrm{th}} \approx 0.055\,\mu\mathrm{m}$), becoming comparable to the optical penetration length ($l_\alpha \approx 0.023\,\mu\mathrm{m}$). As a consequence, laser heating was implemented as a volumetric heat source Q, rather than as a surface heat flux.

7) Similarly to the ns simulations, vapor ejection and plasma generation were not explicitly included in the model to limit computational complexity. As discussed in Subsection 2.1.3, plasma formation predominantly occurs

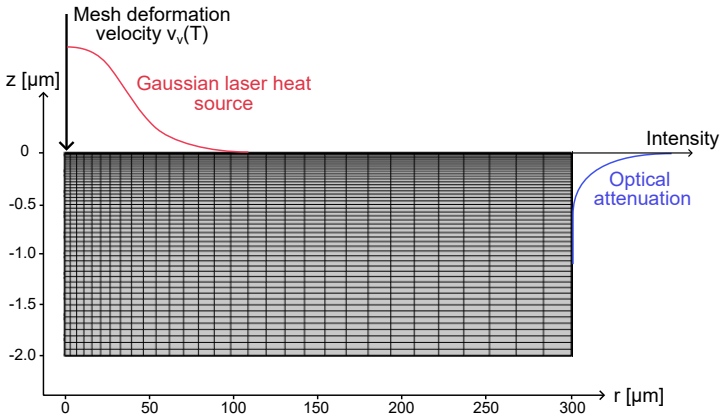

Figure 5.3: Computational domain with the rectangular mesh used for ps simulations.

after the end of the laser pulse resulting in a weak laser-plasma interaction, and a minor shielding effect may arise due to air breakdown. However, since the experiments were performed in a low pressure environment ($p \sim 1$ mbar), this contribution is expected to be small. For this reason, plasma shielding was assumed to be negligible.

A schematic representation of the computational domain and the adopted mesh is illustrated in Figure 5.3. The computational domain extends 2 µm in the axial direction and 300 µm in the radial direction, representing the right half of the target due to the axial symmetry. Given the reduced thermal diffusion length compared to the ns case, a finer mesh was adopted in the z direction. The mesh consists of a total of 1500 rectangular elements, with 50 elements in the z direction and 30 along the r direction, both characterized by size ratios of 1:5. This choice was made after a mesh sensitivity analysis.
Boundary conditions were identical to those adopted for ns model and described in Subsection 4.2.1. The only difference concerns the laser heat source, which in this case was introduced as a volumetric heat source term Q inside the heat transfer equations. The laser source was modeled using Gaussian distribution in space and time, including the optical attenuation through the Lambert-Beer law, as expressed in Equation (4.2).

5.2.2 Material removal mechanism

In the ps laser ablation regime, for the fluence range considered in this study, material removal is predominantly governed by thermal processes, with phase explosion generally identified as the dominant mechanism. In the present work,

ablation was modeled using the deformed geometry module in COMSOL, which allows for the dynamic recession of the upper boundary during the simulation. In contrast to the approach adopted for phase explosion in ns irradiation (Subsection 4.2.2), a different simulation strategy was employed. The deformation velocity $v_v(T)$ was determined from an energy balance at the upper surface of the target, expressed as [65]:

$$v_v(T) = \frac{q_v(T)}{\rho(T) \cdot L_v}. \tag{5.3}$$

The vaporization heat flux $q_v(T)$ was computed as:

$$q_v(T) = h(T) \cdot (T - 0.9 \cdot T_{\text{crit}}), \tag{5.4}$$

where $h(T)$ is an effective heat transfer coefficient, implemented as a ramp function that becomes active when the temperature exceeds $0.9 \cdot T_{\text{crit}}$. In the simulations a very steep slope (of the order of 10^9) was used to ensure rapid activation of ablative heat flux once the phase explosion threshold is reached.
With this formulation, when the local superficial temperature exceeds $0.9 \cdot T_{\text{crit}}$ a high magnitude heat sink is applied on the upper boundary to simulate energy loss due to ablation, while a corresponding deformation velocity is generated. This ensures instantaneous material removal for surface regions exceeding the phase explosion temperature threshold.
Compared to the approach discussed in Subsection 4.2.2, this method offers improved numerical robustness regarding instantaneous material removal even in cases of extremely high heat rates. In such conditions (for ultra-short pulse duration), the use of a deformation velocity limited by the speed of sound c_s may be insufficient to remove material rapidly enough, potentially leading to regions with unrealistic surface temperatures. The present formulation avoids this issue while remaining compatible with the dynamic mesh deformation framework.

5.2.3 Experimental

Laser ablation experiments were performed on small tungsten samples, characterized by a square surface of approximately 12 mm $\times$ 12 mm and a thickness of about 1 mm. The samples were mechanically polished on both surfaces and characterized by a surface roughness of $R_a \approx 500$ nm.
A schematic view of the experimental layout is shown in Figure 5.4. A PHAROS laser was used to generate laser pulses at a wavelength of 1030 nm with a maximum pulse energy of 4 mJ. The pulse duration of the laser system was tunable in a range 400 fs $-$ 10 ps. For this work it was set to 10 ps. Both the pulse energy

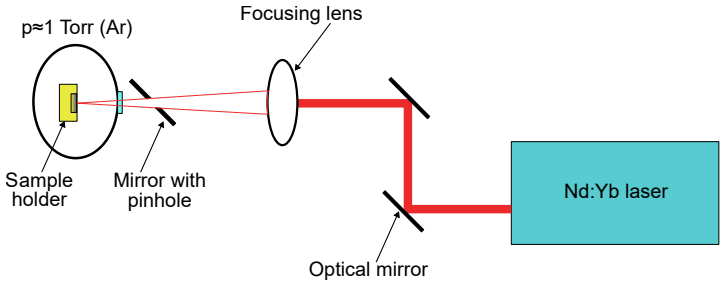

Figure 5.4: Sketch of the laser beam optical path used for the experiment.

and the number of pulses delivered to each crater were controlled through the laser software interface.

The optical path consisted of two mirrors placed immediately after the laser aperture for beam alignment, followed by a converging lens ($f = 50\,\text{cm}$) for focalization of the beam onto the target surface. After the lens, the beam passed through a mirror with a central pinhole, used to deflect plasma light emission towards a collection system composed of an additional lens and an optical fiber. This fiber was connected to an optical spectrometer, enabling the acquisition of LIBS spectra.

The samples were placed inside a low-pressure chamber in an argon atmosphere at $p \sim 1\,\text{mbar}$. The laser spot size on the sample surface was estimated from the size of the craters, yielding a radius of approximately $100\,\mu\text{m}$. The samples were mounted on a movable translation stage, allowing the position to be adjusted in the plane orthogonal to the laser propagation direction.

The experimental campaign was carried out by varying the pulse energy from 1.5 mJ to 4 mJ in steps of 0.5 mJ, corresponding to a fluence range of approximately $\sim 4 - 12\,\text{J/cm}^2$. Craters were generated using 64 consecutive pulses, in order to obtain sufficiently deep and easily measurable features.

Initial inspection of ablation craters was performed using an optical microscope (VHX-S770E Keyence, Osaka, Japan) in order to qualitatively assess the morphology and surface modifications. Full 3D crater reconstructions were subsequently obtained using an optical profiler (VR-6200 Keyence, Osaka, Japan) based on the Structured Light 3D scanning algorithm and characterized by a vertical resolution of approximately $2.5\,\mu\text{m}$. Each scan, using the maximum available magnification of the instrument, allowed the reconstruction of a region of about $\sim 1400\,\mu\text{m} \times 1900\,\mu\text{m}$, with a discrete sampling resolution of $1.8490\,\mu\text{m}$ along both x and y directions.

An example of a 3D crater reconstruction for $E = 4\,\text{mJ}$ is illustrated in Figure 5.5(a). For the quantitative analysis of crater morphology a MATLAB routine was developed. The algorithm used first identifies the crater area and its bound-

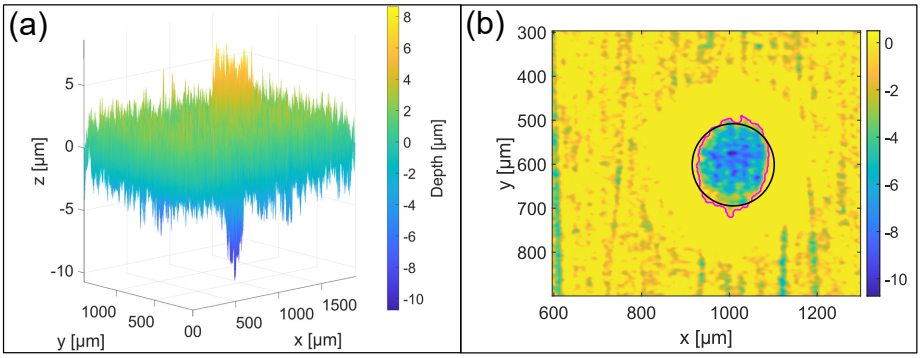

Figure 5.5: 3D reconstruction of ablation crater on W ($E = 4\,\text{mJ}$, 64 pulses) (a) and circular fitting of crater boundaries (b).

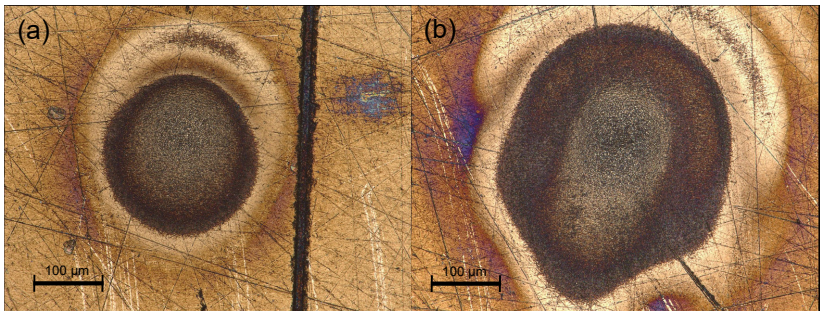

Figure 5.6: Microscope images of ablation craters on tungsten generated with $E = 1.5\,\text{mJ}$ (a) and $E = 4\,\text{mJ}$ (b).

aries using functions from the Image Processing Toolbox [96]. Then, the crater depth was estimated as the average height of all points located below the 5^{th} percentile of height distribution. The crater diameter was then computed by fitting the detected boundary points with a circle via a linear least-squares fitting procedure. An example of fitting result is reported in Figure 5.5(b).

5.2.4 Validation against tungsten experimental data

This Subsection presents the results of experimental observations and FE simulations on tungsten.

Figure 5.6 reports low-magnification images of ablation craters generated from the lowest (a) and the highest (b) pulse energies employed. At low energy, the crater exhibits an almost perfectly circular shape, whereas at high energy it becomes noticeably elongated, likely as a consequence of increased lateral ablation because of the higher incident fluence. Three distinct regions can be observed around the craters: (i) a central gray region corresponding to the main depression, (ii) a darker gray annular region associated with redeposition

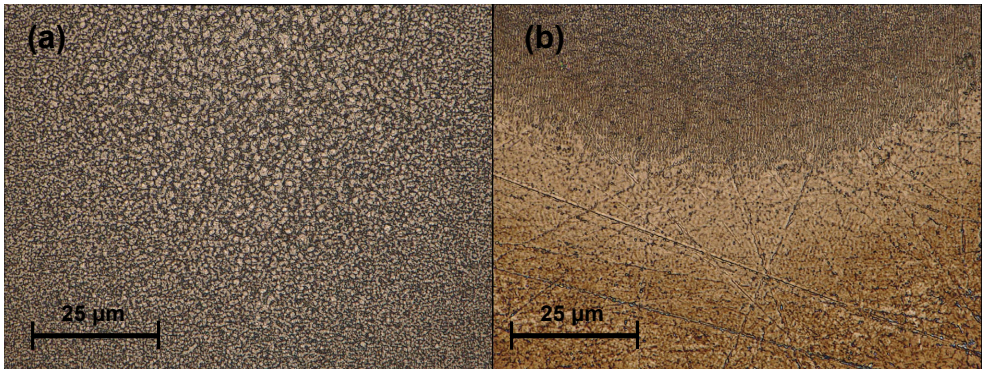

(a) $E = 1.5\,\mathrm{mJ}$, crater middle. **(b)** $E = 1.5\,\mathrm{mJ}$, crater border.

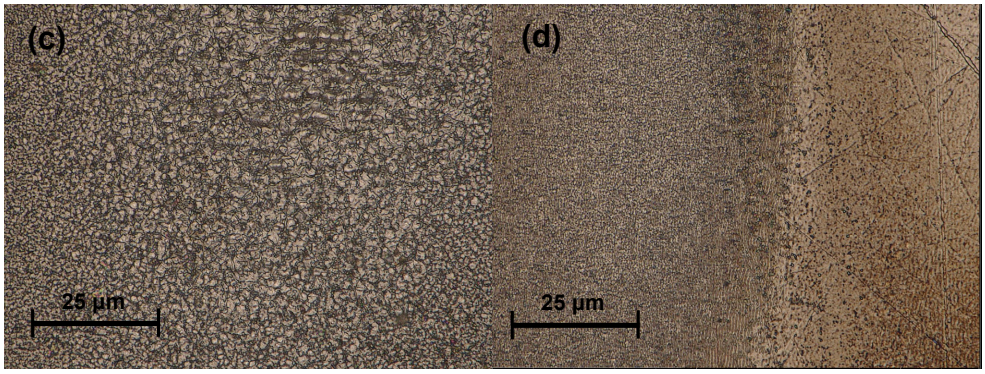

(c) $E = 4\,\mathrm{mJ}$, crater middle. **(d)** $E = 4\,\mathrm{mJ}$, crater border.

Figure 5.7: Microscope images with higher magnification of ablation craters on W.

of material, and (iii) an external yellow region linked to heat-induced surface modifications and possibly oxide formation.

Figure 5.7 shows higher-magnification microscope images. Panels (a) and (b) correspond to zoomed views of the crater middle and boundary between regions (ii) and (iii) for the lowest energy case, while panels (c) and (d) show the same regions for the highest energy case. In the central regions (a) and (c), a granular texture is visible at the bottom of the crater, accompanied by bubble-like structures with characteristic sizes around 5 µm. Similar morphologies have been reported in the literature for conditions where the melt layer undergoes rapid overheating close to liquid-gas spinodal, i.e., in regimes compatible with phase explosion [69]. Along the crater boundaries (b) and (d), several small resolidified droplets can be observed, with characteristic dimensions of approximately 1 µm. Moreover, surface scratches, likely originating from the mechanical polishing, are visible in both energy conditions.

For numerical simulations, the same tungsten material properties listed in Table

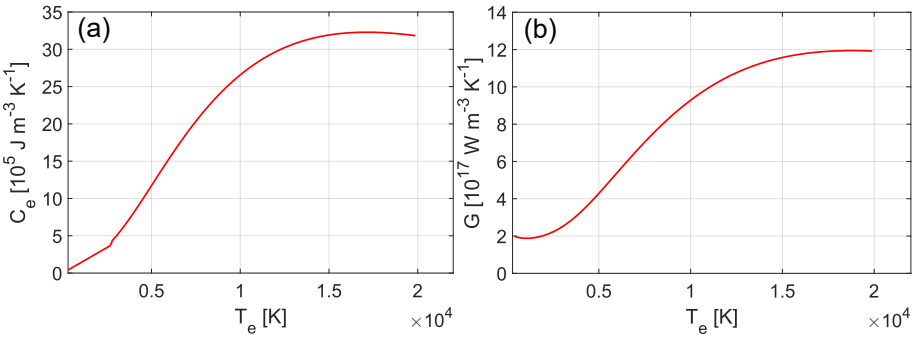

Figure 5.8: Electron heat capacity C_e (a) and electron-lattice coupling constant G (b) as a function of T_e [97].

4.1 were used for the lattice subsystem. For the electron subsystem, a linear temperature-dependent electron thermal conductivity $k_e(T_e)$ was adopted (Equation (5.2)) using a $k_{e0} = 170\,\mathrm{W/mK}$ [98]. Temperature-dependent relations for the electron heat capacity $C_e(T_e)$ and the electron-lattice coupling parameter $G(T_e)$ were taken from the work of Lin et al. [97], who derived these quantities from first-principles electronic structure calculations. The adopted functions are presented in Figure 5.8, where it can be observed that they are characterized by deviations from simple linear trends. Outside the represented temperature ranges, constant extrapolations were applied.

Since the laser energy primarily couples to the electron system, the reflectivity $R(T_e)$ presented in Table 4.1 was adopted. A constant absorption coefficient $\alpha = 4.4 \cdot 10^7\,\mathrm{m}^{-1}$ was assumed [82]. The laser pulse duration was set to $\tau = 10\,\mathrm{ps}$, with peak arrival time at $t_0 = 20\,\mathrm{ps}$. Pulse energies were varied from 1.5 mJ to 4 mJ in steps of 0.5 mJ. Since during the experiments laser energy was directly monitored from the laser software, an attenuation factor of 16% ($\approx 4\%$ per optical element) was applied to the nominal energy value. A laser radius of 110 µm was used, which was determined from a preliminary sensitivity analysis over r_0, and yielded good agreement with experimental crater depths and the crater radius trend.

Figure 5.9 shows the temporal evolution of the maximum surface T_e and T_l for $E = 1.5\,\mathrm{mJ}$ (a) and $E = 4\,\mathrm{mJ}$ (b). In both cases, T_e exhibits a rapid rise and reaches its maximum shortly after the temporal peak of the laser pulse ($t_0 = 20\,\mathrm{ps}$). Conversely, the T_l increase is slightly delayed because of the energy transfer from electron to lattice.

For both energies, T_l reaches a plateau around 14 400 K, corresponding to the assumed threshold for phase explosion ($0.9 \cdot T_{\mathrm{crit}}$), confirming that this regime dominates material removal in these experimental conditions. The saturation ob-

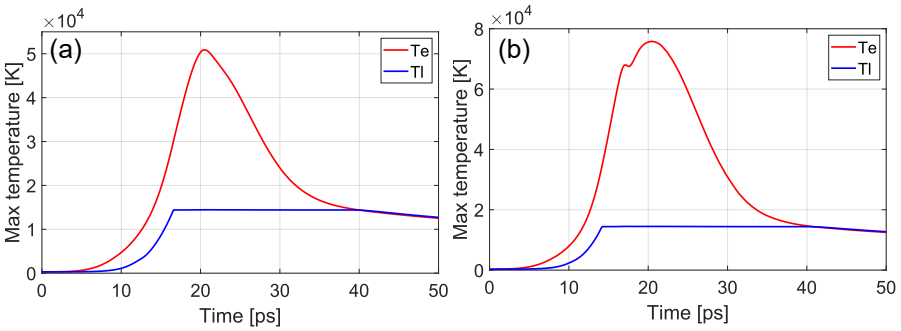

Figure 5.9: Temperature evolutions for the maximum electron and lattice temperatures for the lowest (a) and the highest (b) energy used.

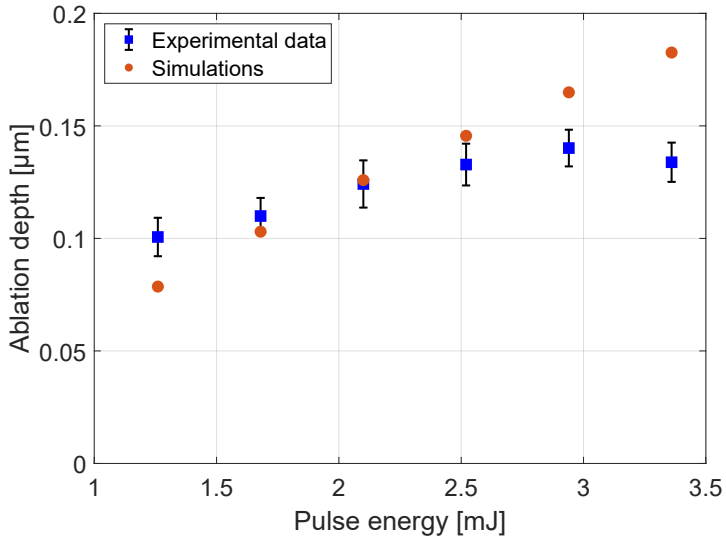

Figure 5.10: Comparison of computed and measured ablation depth as a function of laser pulse energy (including optical losses).

served in simulations is a direct consequence of the onset of ablation mechanism, which introduces an effective heat sink at the surface. The thermal equilibrium between the two subsystems is established after ~ 40 ps; beyond this time, both temperatures start to decrease as heat diffusion in the bulk becomes dominant. The small dip observed for T_e in Figure 5.9(b) around $t = 17$ ps is attributed to a numerical artifact arising from a combination of the strong ablative heat sink and the dynamic mesh deformation.

Figure 5.10 compares the experimentally measured and simulated ablation depth per pulse for the different laser pulse energies. To ensure consistency with the algorithm used for experimental depth calculation, the simulated crater depth was computed from the COMSOL deformed geometry as an average between

points on the upper boundary B for $z < 0.95 \cdot z_{\min}$:

$$\overline{z} = \frac{\displaystyle\int_{B(z<0.95\cdot z_{\min})} z(r)\, dr}{\displaystyle\int_{B(z<0.95\cdot z_{\min})} dr}. \tag{5.5}$$

A very good agreement was obtained over most of the investigated energy range, with relative discrepancies below 20%, except for the highest energy point, where the deviation increases up to 38%; excluding this last point, the model and the experiment exhibit a consistent increasing trend.

At the highest experimental energy, a slight reduction in the measured ablation depth is observed, leading to a slope change in the linear dependence. This effect can be explained by a combination of geometrical and hydrodynamic factors. Since the craters are generated by 64 consecutive pulses, the cumulative depth (exceeding 10 µm) leads to an evolution of crater morphology. As a consequence, the laser energy is distributed over a larger effective area because of the steepening of the lateral walls; this geometric effect leads to a reduction of the local fluence compared to a flatter surface, thereby decreasing the ablation efficiency at the crater bottom. Additionally, a large ablation depth can lead to a hydrodynamic confinement effect, where the vaporized material above the crater can limit the efficient ejection of underlying layers [99]. These effects are not explicitly included in the present model and may explain the larger discrepancy at the highest energy. However, additional measurements in this specific fluence range would be necessary to confirm the reproducibility of the observed trend, and further analysis would be required to validate the proposed hypotheses.

Figure 5.11 presents the comparison between the simulated and experimentally measured crater diameters. The experimental trend with pulse energy is well reproduced by the model. Although simulated craters are slightly wider than the experimental ones, the relative discrepancy remains below 25% across the entire energy range.

Finally, Figure 5.12 shows the temporal evolution of the lattice temperature field and deformed geometry for the lowest (a) and the highest (b) pulse energies. Four different time instants are reported: $t = 10, 20, 40, 50$ ps, corresponding respectively to $t_0 - \tau$, t_0 (temporal Gaussian peak), $t_0 + 2\tau$ (thermal equilibrium between the two subsystems) and $t_0 + 3\tau$ (end of the simulation).

At $t = 10$ ps, the surface temperature is below both the boiling point and the phase explosion threshold, and no material removal is observed. At $t = 20$ ps, the surface temperature reaches approximately 14 400 K and material removal becomes evident. At this stage, temperatures locally exceeding the phase ex-

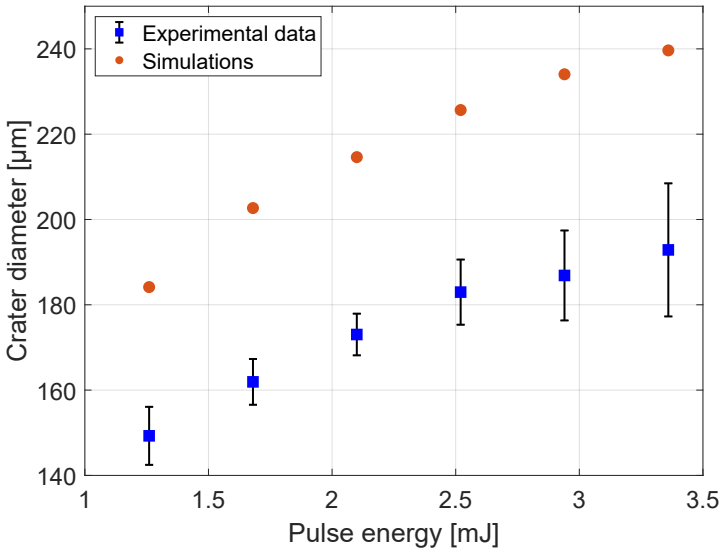

Figure 5.11: Comparison of computed and measured crater radius as a function of laser pulse energy (including optical losses).

plosion threshold are visible. This is a numerical artifact originating from the combination of volumetric laser heating and an ablative heat flux implemented as a superficial heat sink, which leads to the formation of a very thin, transient subsurface layer experiencing overheating. This layer persists for approximately 15 ps before being eliminated by material removal and heat diffusion. Although this is a pure numerical effect, this region may correspond to a finite layer of metastable superheated material where the onset of thermodynamic instabilities characteristic of phase explosion could occur.

At the subsequent time instant, $t = 40$ ps, the crater is almost fully developed for both energies, and the superheated layer has disappeared. At the final time instant, $t = 50$ ps, the system enters the cooling phase: surface recession has ceased, while heat diffusion into the bulk is still ongoing, with the temperature reduced down to a value around 12 800 K for both energies. The surface recession at the end of the simulation does not show significant variation with respect to $t = 40$ ps. As expected, the crater generated at $E = 4$ mJ is deeper and wider than that obtained at $E = 1.5$ mJ.

Considering the investigated fluence range, the material removal mechanism is still governed by thermal effects with the ablation driven by the temperature increase and the subsequent onset of phase explosion. As a consequence, the near-surface region is characterized by steep temperature gradients, which promotes heat conduction and lead to the formation of a HAZ, as also suggested by the microscope observations of the craters.

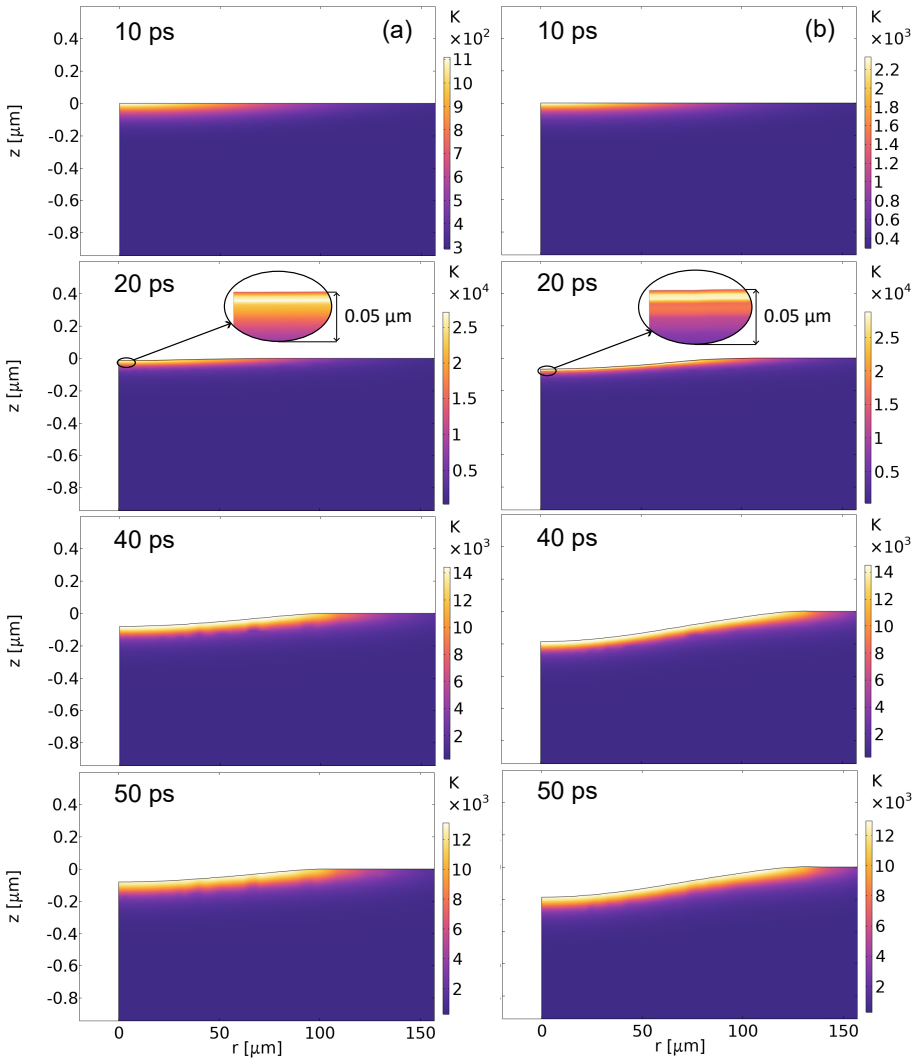

Figure 5.12: Temperature and domain evolution for $E = 1.5\,\mathrm{mJ}$ (a) and $E = 4\,\mathrm{mJ}$ (b).

By analyzing the temperature field at the final time instant, the extent of the molten region (defined by $T > T_m$) can be estimated. This region extends down to approximately $\sim$ 185 nm and $\sim$ 285 nm for 1.5 mJ and 4 mJ, respectively, corresponding to nearly 100 nm below the final crater depth. These results confirm that, under the investigated conditions, ps laser ablation leads to a more localized energy deposition, with a reduced thermal diffusion into the bulk material compared to the ns regime. This behavior is consistent with the shorter pulse duration and the delayed electrons to lattice energy transfer, as described by the TTM.

6 In-situ LIBS investigation of short-term deuterium retention in tungsten and tantalum

Retention of hydrogen isotopes in PFCs represents a key issue in PWI studies for magnetic fusion devices, with direct implications for fuel recycling, safety constraints, economy, and tritium inventory management.
Depending on the time scale under consideration, the concept of retention refers to different physical processes and observables. Long-term retention typically describes the amount of hydrogen isotopes remaining trapped in materials for days, weeks, or longer after plasma exposure; this contribution is commonly investigated using post-mortem techniques such as TDS, Residual Gas Analysis (RGA), and NRA.
Conversely, short-term retention refers to the fraction of implanted fuel that is released from the near-surface region in the minutes to hours following plasma termination. This transient desorption phase, often referred to as outgassing, can account for a significant fraction of the total retained fuel and therefore plays an important role in determining the effective tritium balance in a fusion device [57].
The investigation of short-term retention requires diagnostics capable of monitoring the fuel content during and immediately after plasma exposure, while minimally perturbing experimental conditions. In this context, LIBS offers several advantages, including the possibility of in-situ and in-vacuum operations, the elimination of sample handling between exposure and experiment, and a temporal resolution compatible with characteristic fuel release timescales.
In an LPD, LIBS measurements can be performed during plasma operation without significant interference for the signal, since the intense and localized atomic emissions from the laser-induced plasma plume are easily distinguishable from the background plasma radiation.
In the present work, an in-situ LIBS diagnostic installed on the PSI-2 linear device

was employed to investigate the short-term deuterium retention behavior of tungsten and tantalum (Ta) samples exposed to deuterium plasma. Tungsten was selected as reference material due to its well-established retention properties and its relevance for ITER and future fusion reactors, while tantalum was included as a complementary material that can be considered a proxy of tungsten with promising thermomechanical properties and very limited experimental data available on hydrogen isotope behavior.
LIBS spectra were acquired at different time instants during and after plasma exposure, as well as at different radial positions on the sample surface. The analysis focused on the temporal evolution of the Balmer D_α emission line, whose integrated intensity was used as a qualitative indicator of deuterium content in the near-surface region probed by laser ablation. Since an absolute calibration for deuterium concentration was not performed, the results are discussed in terms of signal intensity evolution, with the aim of identifying characteristic trends and timescales of the desorption process.
The chapter is organized as follows. Section 6.1 describes the experimental setup, plasma exposure conditions and measurement methodology adopted for in-situ experiment. Section 6.2 presents the data analysis procedure and discusses the short-term retention behavior of the two materials based on LIBS measurements. Finally, Section 6.3 reports and discusses complementary post-mortem NRA measurements performed a few days after the experiment, providing an independent and quantitative assessment of long-term deuterium retention and a complementary perspective to the LIBS results.

6.1 Experimental layout, procedure and methodologies

The experimental activity presented in this chapter was carried out using in-situ LIBS on the PSI-2 linear plasma device. This Section describes the experimental layout, the plasma exposure conditions and the measurement procedure adopted before, during and after plasma exposure.
The LIBS diagnostics installed on PSI-2 is based on a nanosecond INNOLAS Nd:YAG laser operating at a wavelength of 1064 nm, with a pulse duration of 8.3 ns. The laser beam is guided from the laser laboratory to the linear device stage by a set of mirrors enclosed in safety optical tubes, for a total optical path length of around 30 m. Measurements presented in this chapter were performed using a pulse energy of approximately 360 mJ, measured upstream of the linear device optical window.
A motorized steering mirror is installed just outside the PSI-2 optical window, allowing remote adjustment of the beam position on the sample surface. The

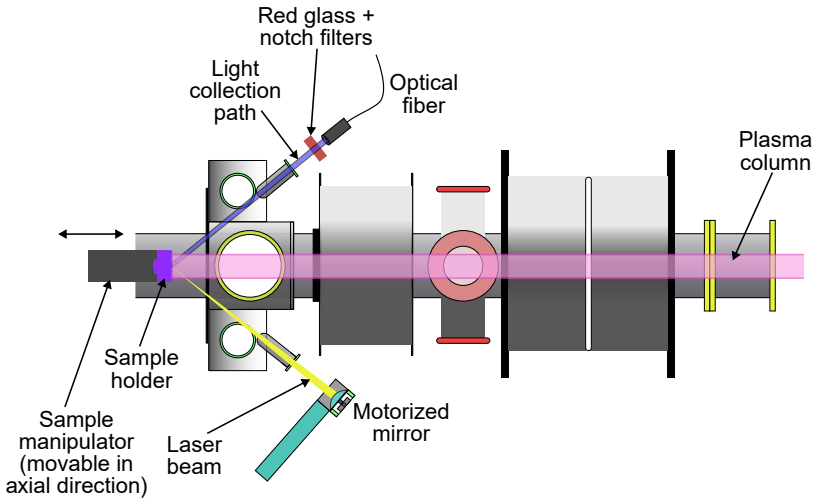

Figure 6.1: Top view of PSI-2 linear device with schematic illustration of laser beam path and collection optics [57].

laser beam is focused on the target using a converging lens, resulting in a spot diameter on the sample surface of approximately 700 µm, as estimated from post-mortem crater size measurement.

Optical emission from laser-induced plasma is collected using a lens ($f = 70$ mm) and transported through a 35 m optical fiber to a spectrometer located in the laser room. A scheme of the laser injection and light collection geometry on the linear device is illustrated in Figure 6.1.

A red glass filter and two notch filters centered at 1064 nm are placed in front of the collection optics. The former is used to suppress overlapping diffraction orders in the spectrometer, while the latter are employed to attenuate reflected laser radiation at the fundamental wavelength.

The spectrometer is a Littrow-type system equipped with a 1200 grooves/mm grating and a collimating doublet with a focal length of 750 mm. The detector is an AVT Pike-032b CCD camera coupled to a Micro-Channel Plate (MCP) for signal enhancement. The acquisition start is triggered with an adjustable delay relative to the laser pulse, that can be tuned to maximize SNR for the spectral line of interest.

Plasma exposure was performed on the PSI-2 linear device [18], which operates in steady-state conditions producing a plasma column with a diameter of approximately 6 cm using a high-current arc discharge. In PSI-2, samples are mounted on a target holder, capable of accommodating up to 8 specimens simultaneously. The sample holder can be negatively biased with respect to the plasma potential, so that the incident ion energy is defined by the potential

difference between the bias voltage and the plasma potential.
Plasma parameters were monitored during the experiment using a reciprocating Langmuir probe. In addition, the temperature of the samples was measured locally using a thermocouple embedded in the sample holder and an infrared thermocamera, which also allowed the detection of temperature differences among the exposed samples.
The experimental campaign focused on W and Ta samples, selected to investigate and compare short- and long-term deuterium retention under identical exposure conditions. While W is currently considered the best candidate material for PFC in tokamaks, Ta was included as a complementary material. The latter has attracted interest due to its superior resistance to helium-induced surface morphology modifications and high melting point [100]; however, experimental studies indicate that Ta exhibits a strong interaction with hydrogen isotopes and potentially less favorable retention properties compared to W [101]. Despite this, experimental data on hydrogen isotope retention in Ta remain scarce, particularly for the short-term retention component in fusion-relevant environments.
The W samples were double-forged polycrystalline plates supplied by Plansee and representative of ITER first-wall grade material. The Ta samples were polycrystalline plates with a nominal purity of 99.95%, produced by molten material and supplied by MaTeck. All samples had surface dimensions of approximately 10 mm $\times$ 10 mm and were mechanically polished and annealed at 1273 K for 1 hour prior to plasma exposure.
Before plasma exposure, preliminary LIBS measurements were performed to assess the presence of residual hydrogen in the samples and to generate dedicated ablation craters for post-mortem evaluation of the ablation rate. Additional measurements were dedicated to the optimization of the spectrometer delay time to maximize the SNR for hydrogen isotope lines.

Exposure parameter	**Value**
Ion flux Γ [$\mathrm{m^{-2}\ s^{-1}}$]	$2.9 \cdot 10^{21}$
Exposure time t [min]	~ 190
Fluence F_{ions} [$\mathrm{m^{-2}}$]	$3.3 \cdot 10^{25}$
Bias voltage V_{bias} [V]	-95
Ion energy E_{ions} [eV]	~ 80
Deuterium gas puffing Φ_{D} [sccm]	100
Cathode current I_{cathode} [A]	100
Average sample temperature T_{samples} [°C]	~ 250

Table 6.1: Plasma exposure parameters used during the PSI-2 experiment.

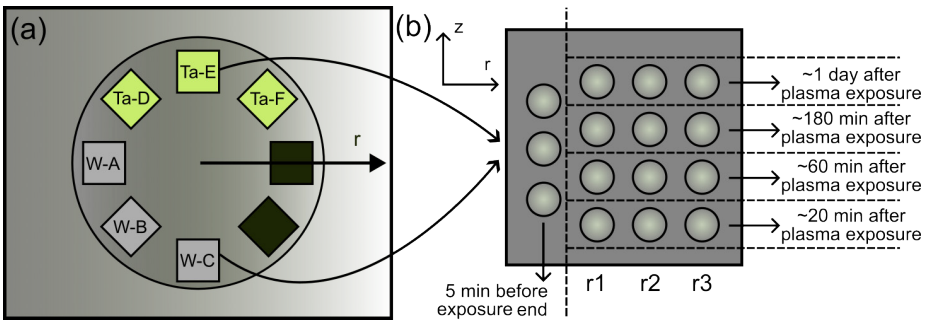

Figure 6.2: PSI-2 target holder with sample arrangement (a) and crater pattern on the samples analyzed with LIBS (samples E and C) (b).

The plasma exposure parameters are summarized in Table 6.1. The samples were exposed to a D plasma for approximately three hours, reaching a total ion fluence of about $3.3 \cdot 10^{25}\,\mathrm{m}^{-2}$. During exposure, the surface temperature of the sample was maintained around 250 °C to limit thermal outgassing and was continuously monitored by a thermocouple. However, IR thermographic measurements revealed a temperature difference between samples of up to ± 40 °C.
In-situ LIBS measurements were carried out both during and after plasma exposure. A scheme of the sample holder containing the exposed samples is shown in Figure 6.2(a), where samples are labeled from A to F. Some trial measurements were performed on samples A and D once thermal stabilization was reached at the beginning of the exposure (after approximately 5 minutes), to assess the correct functioning of the diagnostics and the visibility of D signal.
For subsequent measurements, samples C and E were selected because they exhibited very similar surface temperatures according to thermocamera measurements. Samples B and F were not subjected to LIBS measurements for potential post-mortem analysis of clean surfaces. The crater pattern used on samples C and E is illustrated in Figure 6.2(b). Measurements performed 5 minutes before the end of the plasma were carried out at the same radial position, while measurements at later times (20 min, 1 hour, 3 hours, and 1 day after plasma exposure) were performed along different radial coordinates to account for the radial dependence of plasma flux in PSI-2. For each measurement location, a limited number of laser pulses was used to minimize modifications of the near-surface region.
In addition to LIBS measurements, the exposed samples were selected for post-mortem NRA analysis, which is presented and discussed in Section 6.3.

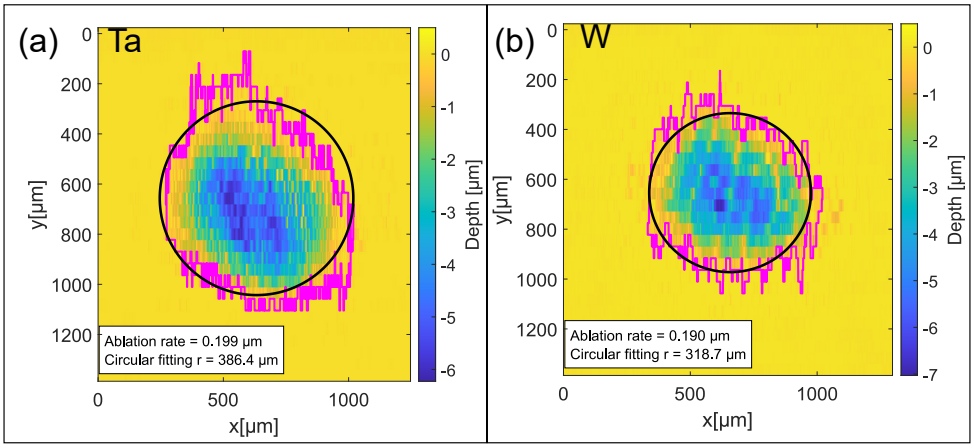

Figure 6.3: Top view of ablation crater reconstructions on Ta (a) and W (b), measured by mechanical surface profiler. The estimated ablation rate and crater diameter are reported in the plots.

6.2 Spectra analysis and outgassing curve reconstruction

The results obtained from in-situ LIBS measurements performed on tungsten and tantalum samples exposed to PSI-2 deuterium plasma are presented and discussed in this section. The analysis is organized around three main steps: (i) characterization of ablation craters and estimation of ablation rates, (ii) optimization of the spectrometer delay time to maximize the hydrogen-isotope signal quality, and (iii) development of a robust data analysis procedure for fitting and extracting the integrated D_α intensity, then used to reconstruct the temporal evolution of deuterium outgassing after the plasma exposure.

As a first step, the ablation craters generated on the two samples were analyzed. The two craters analyzed below were produced prior to plasma exposure using approximately 30 consecutive laser pulses to enable a post-mortem evaluation of the ablation rate and of the effective beam spot size. Figure 6.3 shows reconstructions of representative craters produced on Ta (a) and W (b), obtained using the mechanical surface profiler described in Subsection 4.2.4. The ablation rates were estimated by dividing the total crater depth by the number of pulses (28 for Ta and 30 for W). A circular fitting of the crater boundary provides an estimate of the beam spot radius of 386.4 µm for Ta and 318.7 µm for W, corresponding to a spot size diameter in the range $\sim 620 - 760$ µm.

To optimize the LIBS signal acquisition for hydrogen isotopes, a gate delay scan was performed before plasma exposure. In this study, the SNR of the H_α line measured from non-annealed samples was evaluated as a function of the delay between laser pulse and spectrometer acquisition. The delay time was varied

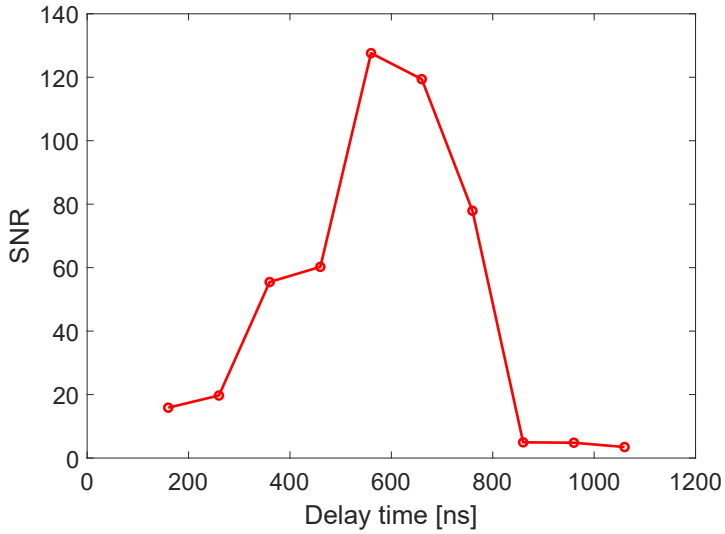

Figure 6.4: SNR of H_α line measured on Ta as a function of spectrometer delay time.

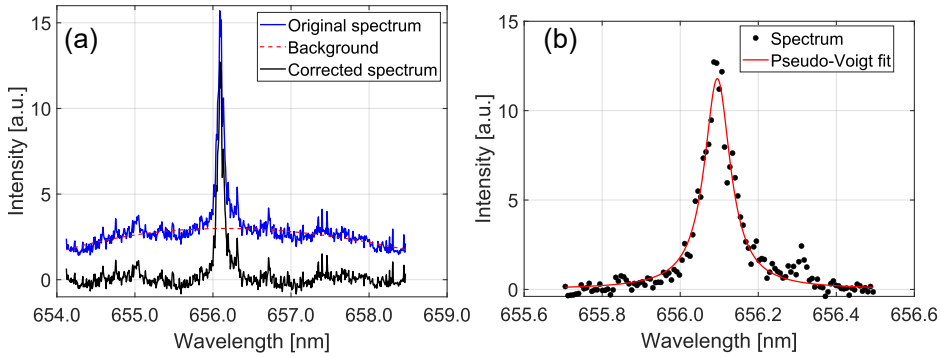

Figure 6.5: Representative LIBS spectrum for W 5 minutes before the end of the plasma exposure (a); Pseudo-Voigt fit of the D_α spectral line (b).

from 60 ns (minimum accessible value) up to 1060 ns, in steps of 100 ns. Since the hydrogen line was readily detectable on W over a relatively wide delay interval (approximately 360 ns − 660 ns), the optimization was performed focusing on Ta. The resulting SNR trend with delay time is shown in Figure 6.4, where a clear maximum is observed at 560 ns. Based on this result and given the generally cleaner detection on W, the value of 560 ns was adopted throughout the experiment.

The first part of the spectral analysis focused on tungsten. All the spectra were calibrated in wavelength using a deuterium lamp measurement to maximize the accuracy in the 656 nm − 656.3 nm range. Figure 6.5(a) reports a representative W spectrum acquired 5 minutes before the end of the exposure, shown before

and after the background correction. A strong D_α emission line can be clearly observed at approximately 656.1 nm.
Since no intense W spectral lines are present in the immediate vicinity of the D_α wavelength, a direct fitting of the peak was possible. In this work, spectral lines were fitted using a pseudo-Voigt function, i.e. a weighted combination of Lorentzian and Gaussian contributions:

$$V(\eta, w) = A \cdot \left\{ \eta \cdot \frac{1}{1 + 4(\frac{x-x_0}{w})^2} + (1-\eta) \cdot \exp\left[-4\ln(2) \frac{(x-x_0)^2}{w^2} \right] \right\}, \quad (6.1)$$

where A is the amplitude, η is the weighting factor and w represents the FWHM (shared by the two components). The function can also be parametrized in terms of its integrated $Area$, by observing that:

$$Area = A \cdot \frac{w}{2} \left[\eta\pi + (1-\eta)\sqrt{\frac{\pi}{\ln 2}}. \right] \quad (6.2)$$

Using the area instead of the amplitude as a fit parameter is convenient because it allows direct extraction of confidence intervals for the integrated peak intensity, which can be used as error bars in the subsequent outgassing analysis. An example of pseudo-Voigt fitting of the D_α line is shown in Figure 6.5(b).
Based on the integrated D_α intensity extracted from individual craters, the temporal evolution of tungsten outgassing signal was then reconstructed. In this analysis, only the first spectrum acquired at each crater location was considered for the reconstruction of the outgassing signal. It is important to underline that each laser pulse induces local heating, so the measured D signal does not originate exclusively from the nominal ablated layer ($\approx$ 190 nm), but may also include a contribution from a slightly deeper subsurface region.
The temporal evolution of the integrated D_α signal is illustrated in Figure 6.6. An uncertainty of $\pm$5 min was assigned to the measurement time. The data points corresponding to time instants after the end of the plasma exposure were obtained by averaging measurements performed at three different radial positions on the sample surface, in order to mitigate the effect of radial non-uniformity of the plasma flux in PSI-2.
The resulting trend shows a slight increase of the D_α signal between the first measurement point and the one acquired at the end of the exposure. This behavior is not attributed to an actual increase of retained D during the exposure, but can be likely related to the fact that the first data point was obtained from a preliminary measurement performed on a different W sample. This was necessary to preserve surface area on the primary target for the crater matrix

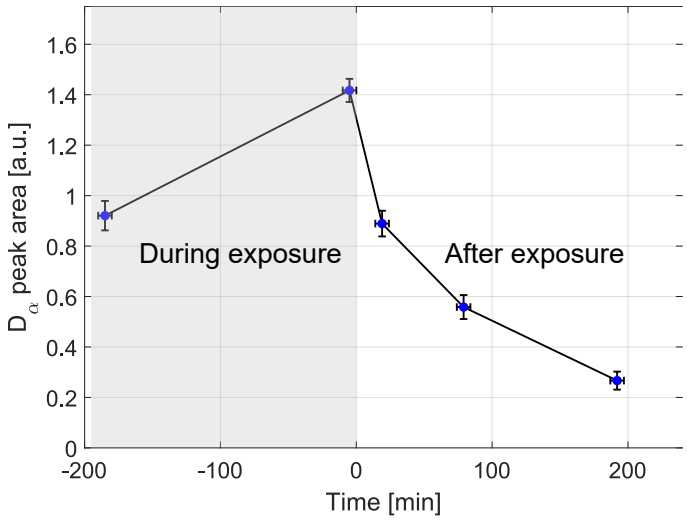

Figure 6.6: Temporal evolution of the integrated D_α emission signal during and after plasma exposure for W. The first data point ($t = -185$ min) originates from a preliminary measurement performed on a different sample.

necessary for the subsequent time-resolved measurement (illustrated in Figure 6.2) avoiding any ablation overlap. This auxiliary sample, although exposed to the same plasma conditions, was characterized by a slightly higher surface temperature ($\Delta T \approx +40$ °C) as indicated by the thermocamera measurement. It is reported in the literature that an elevated surface temperature can enhance hydrogen isotope mobility and promote outgassing from the near-surface region, reducing the detectable signal [102].

After plasma termination, a clear decrease of the D_α signal can be observed, indicating a progressive deuterium release from the near-surface region. The decay trend is compatible with a power-law behavior of the form $A \cdot t^{-\alpha}$, commonly reported in literature to describe hydrogen outgassing fluxes from metals [53]. A tentative fit, including also the data point acquired the day after plasma exposure (after almost 20 hours after the end of the exposure), is shown in Figure 6.7. Although the limited number of data points and their scatter restrict the analysis to a qualitative level, the extracted value for the exponent $\alpha = 0.436 \pm 0.28$ is compatible with values reported in the literature [102].

The analysis of Ta spectra required a more complex procedure compared to W, due to the presence of some quite intense emission lines in the spectral region surrounding the D_α wavelength.

A representative LIBS spectrum acquired from the bulk of an annealed, non-exposed Ta sample is shown in Figure 6.8(a). The main emission peaks were

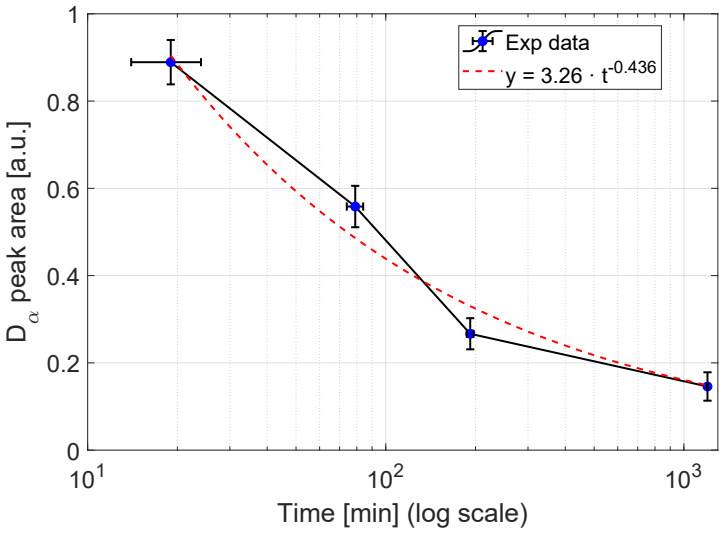

Figure 6.7: Tentative power-law fit of the post-exposure D_α decay for W, including data point acquired 20 hours after the end of the exposure.

identified using the NIST atomic spectra database and are highlighted with colored markers [103]. In addition to the expected Ta transitions, a spectral feature centered around 655.97 nm (indicated by a red bar in the plot) was systematically observed with an approximately constant relative intensity. This line cannot be attributed to a Ta transition according to the NIST database; the associated wavelength is compatible with an intense Cu II transition, suggesting a possible impurity contribution related to sample manufacturing. A definitive identification of this line would require a complementary dedicated analysis, which is beyond the scope of the present work.

During plasma exposure, the two emission lines indicated with B and C in Figure 6.8(b) were found to significantly interfere with the D_α wavelength region, making a direct fit of the deuterium peak unreliable. To address this issue, a dedicated fitting and subtraction procedure was used:

(i) After background subtraction, the brightest Ta emission line (A) was fitted using a pseudo-Voigt profile.

(ii) Assuming that the intensity ratio between lines A/B and A/C remains approximately constant across different measurements, the B and C lines were reconstructed using pseudo-Voigt functions with the same line-shape parameters (w and η) as peak A, while scaling amplitude proportionally.

(iii) The reconstructed B and C contributions were then subtracted from the

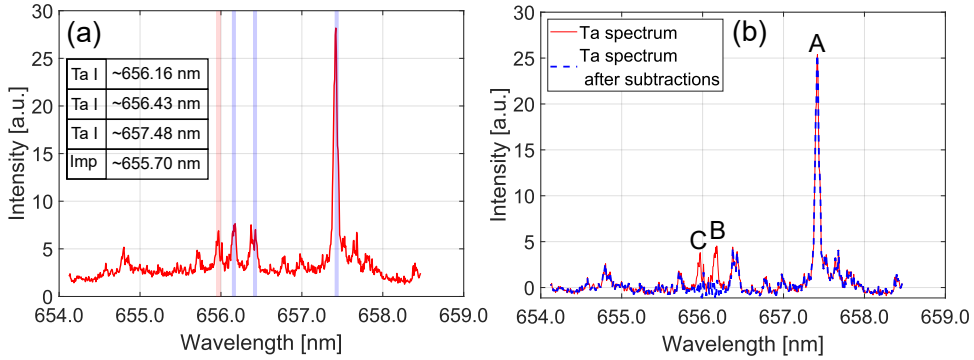

Figure 6.8: LIBS spectrum from the bulk of an annealed, non-exposed, Ta sample (a); Identified Ta emission lines are marked in blue [103], while "Imp", marked in red indicates a possible impurity line. Same spectrum after subtractions of lines B and C (b).

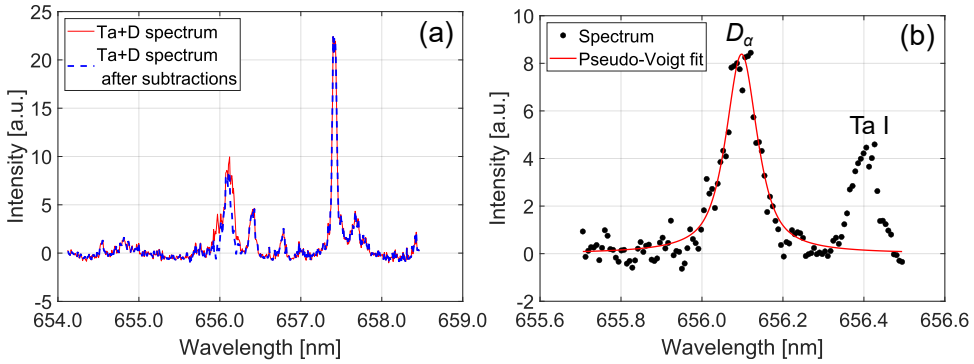

Figure 6.9: LIBS spectrum from a Ta sample acquired 5 min before exposure end, shown before and after the subtraction of peaks B and C (a). Pseudo-Voigt fit of the isolated D_α peak (b).

original spectrum, as illustrated for example on a Ta bulk spectrum in Figure 6.8(b).

This procedure enabled the isolation of the D_α peak in spectra acquired from exposed Ta samples, as illustrated in Figure 6.9(a) for a signal acquired 5 minutes before the end of the plasma. The resulting isolated peak could be then fitted using a pseudo-Voigt function following the same procedure used for W, as shown in Figure 6.9(b), where an acceptable result was obtained.
This procedure allows a reliable reconstruction of D_α peak only when the deuterium signal remains sufficiently intense. As outgassing progresses and the deuterium signal decreases, the fitting becomes increasingly sensitive to noise and to residual uncertainties from the subtraction procedure. For this reason, data points corresponding to late times (specifically, the central radial position

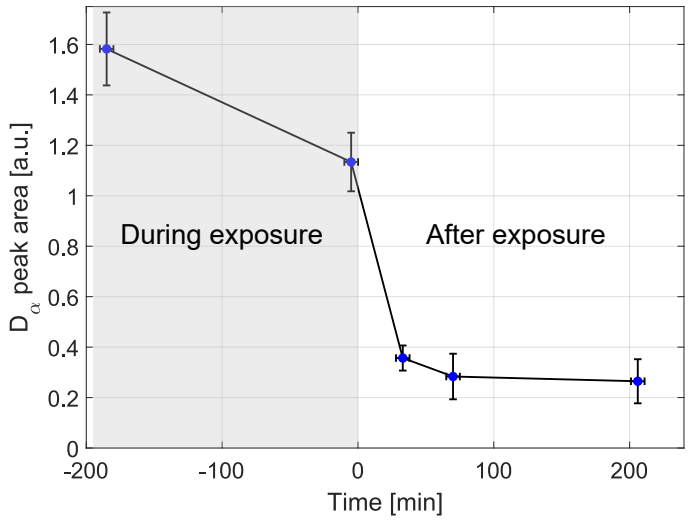

Figure 6.10: Temporal evolution of the integrated D_α emission signal during and after plasma exposure for Ta. The first data point ($t = -185$ min) was acquired from a preliminary measurement performed on a different sample.

at $t = +180$ min and all the measurements performed one day after plasma exposure) were excluded from the analysis.
Despite these limitations, a temporal evolution curve for the D_α signal for Ta was reconstructed using the same averaging procedure adopted for W. The resulting outgassing curve is illustrated in Figure 6.10.
Similarly to W, a difference in signal level is observed between the first data point ($t = -185$ min) and the measurement acquired at the end of plasma exposure. Again, this is likely caused by the fact that the first data point originates from a preliminary measurement performed on a different Ta sample, following the same experimental strategy adopted for W.
After plasma termination, a general decay of D signal is observed, indicating deuterium release from the near-surface region. However, due to the limited number of reliable data points and the increased uncertainty associated with fitting procedure, it is not possible to robustly determine whether decay follows a power-law trend.
A direct comparison between the normalized outgassing curves reconstructed for W and Ta is illustrated in Figure 6.11. The plot suggests that Ta may exhibit a slightly faster initial decrease of the D_α in the early post-exposure phase ($0 - 150$ min), while retaining a higher relative signal at longer times. Nevertheless, it is important to underline that this observation should be regarded as indicative only, due to the qualitative nature of the non-calibrated LIBS signal, and the

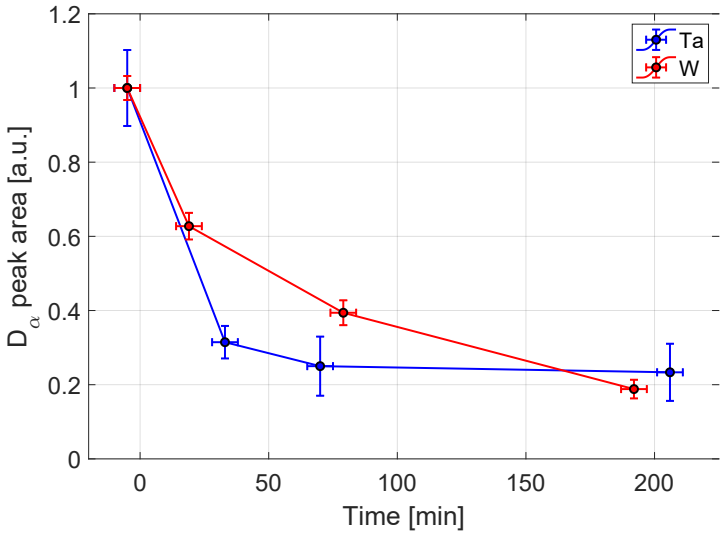

Figure 6.11: Comparison between normalized outgassing curves for W and Ta.

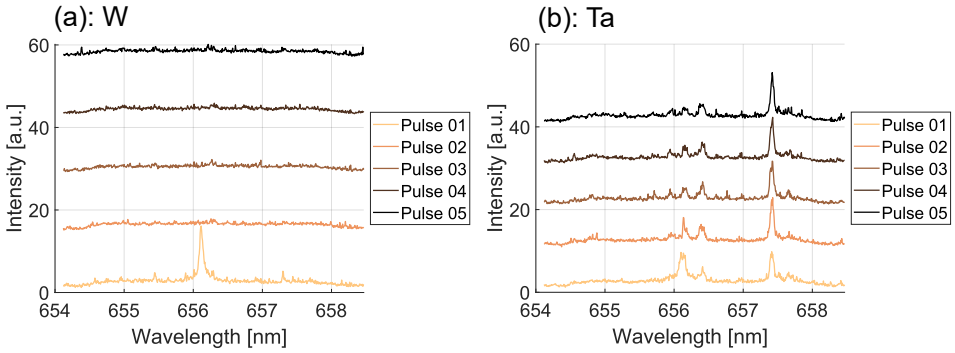

Figure 6.12: Evolution of LIBS signal over successive laser pulses on the same crater for W (a) and Ta (b). The measurements were acquired $\approx$ 20 min after the exposure end.

spectral overlap issues specific to tantalum.
The complementary NRA results, which will be presented in the next Section, will be essential in giving reliable information about the absolute retention for the two materials, providing a quantitative reference for the D content.
Additional insights can be gained by examining the evolution of D_α signal over successive laser pulses on the same crater, as shown in Figure 6.12. Both measurements were acquired at similar times, approximately 20 min after the exposure, and from the same radial position. While the D signal on W almost completely disappears after the first pulse, a residual D_α contribution remains detectable on Ta even after the second pulse. This behavior suggests a possible deeper or more spatially distributed D population compared to the W case.

For future investigation, the observation of the D_β line (visible at 486.0 nm) could be advantageous, as it would avoid the spectral overlap with tantalum emission lines observed in this experiment, allowing a cleaner procedure for the fitting of deuterium peak.

6.3 Results of NRA measurements

NRA measurements provide a complementary and quantitative assessment of deuterium retention, enabling the investigation of both the regions inside the LIBS ablation crater and the surrounding areas. The measurements presented in this section were performed using a ^{3}He ion beam with an energy of 2950 keV. Under these conditions, the average depth range for tungsten and tantalum reached approximately 3.3 µm, significantly larger than the depth affected by single pulse LIBS ablation.

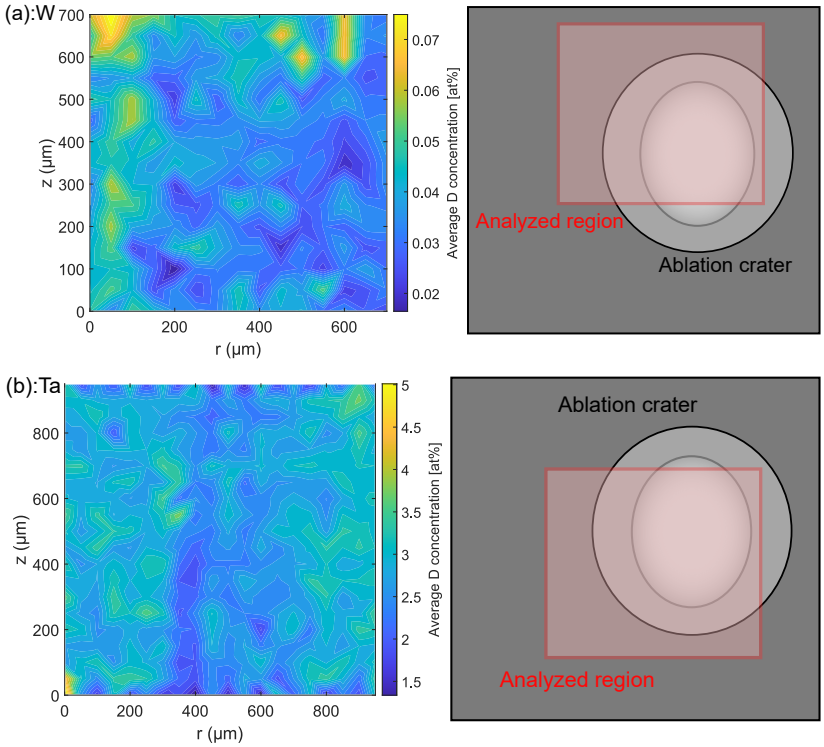

Figure 6.13: Two-dimensional maps of depth-averaged D concentration obtained by NRA for W (a) and Ta (b). The analyzed region relative to LIBS crater is schematically indicated next to each map.

Two-dimensional maps representing the depth-averaged D concentration were obtained for samples exposed to plasma and previously analyzed by LIBS (sam-

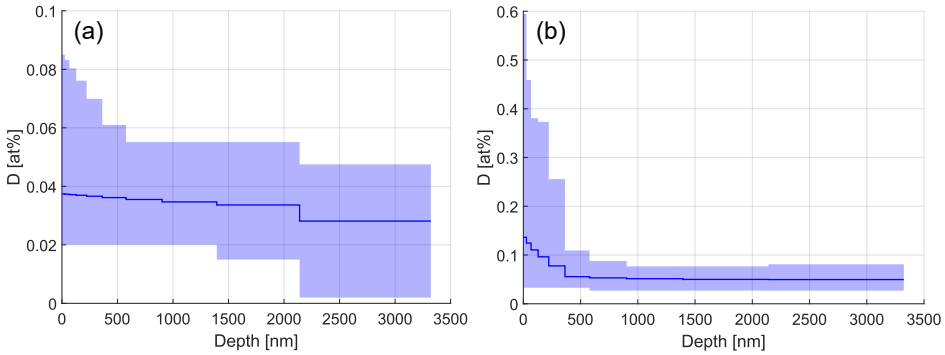

Figure 6.14: Depth profiles of D concentration in W for regions located inside (a) and outside (b) the ablation crater. The blue solid line represents the average value, while the shaded areas indicate the minimum and maximum ranges.

ples C and E). The resulting maps are represented in Figure 6.13(a) for W and (b) for Ta. In each case, the region analyzed around the LIBS crater is indicated schematically next to the concentration map.

A first clear result emerging from NRA data is that the average D concentration in Ta is significantly higher than in W, when considering the same exposure conditions and an average depth range of approximately 3.3 µm. This finding is consistent with the strong interaction between hydrogen isotopes and Ta reported in the literature. The derived spatial distribution from the NRA maps indicates a non-uniform D concentration in the vicinity of the LIBS crater for both the materials. Such non-uniformity may arise from multiple factors such as the non-uniform plasma flux profile of PSI-2, local temperature variations, or modifications of the near-surface region induced by repeated ablations.

For W, the spatial distribution of D concentration shows features that can be qualitatively related to LIBS crater geometry. Regions with higher concentrations are visible, particularly across the upper-left diagonal of the image, where the crater footprint is clearly distinguishable. In contrast, for Ta, the correspondence between concentration map and crater geometry is less evident.

To further explore this analysis, average depth profiles of D concentration were extracted for selected regions, one located outside and the other inside the ablation crater. The results for W are shown in Figure 6.14, where the average concentration has been plotted for two regions with an approximate area of 150 µm $\times$ 150 µm: the first one (a) represents the inside of the LIBS crater (center-right of the concentration map), while the second one (b) represents the outside part (top left of concentration map). The region inside the crater shows a decreasing concentration with depth from about 0.04% to approximately 0.03% at larger depths, while the region outside the crater displays a higher near-surface

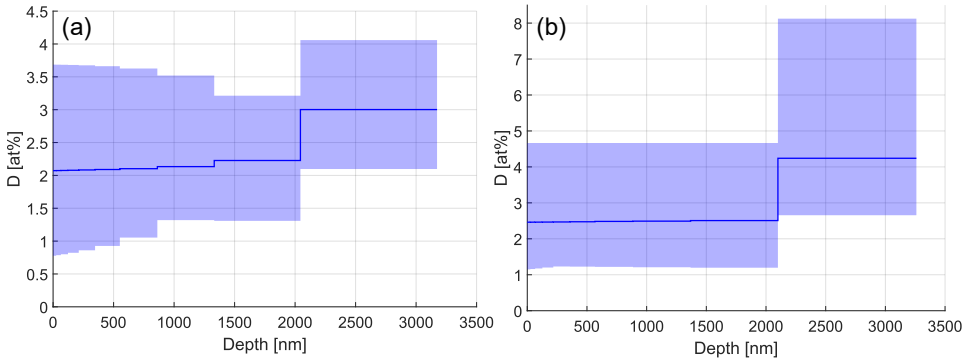

Figure 6.15: Depth profiles of D concentration in Ta for regions located inside (a) and outside (b) the ablation crater. The blue solid line represents the average value, while the shaded areas indicate the minimum and maximum ranges.

concentration, around 0.1%, decreasing towards a bulk value of approximately 0.05%. It should be noted that the region outside the crater is characterized by a very large local concentration variability, with some measurement spots characterized by significantly higher D content, which strongly influences the average depth profile.

Similar plots were computed for Ta and are shown in Figure 6.15 for regions of comparable size to the ones considered for W; the first one (a) represents the inside of the crater (around the middle of concentration map) and the second one represents the outside part (bottom left of the mapping) (b). In this case, the average D concentration is found to be one to two orders of magnitude higher than in W. Within the crater region the D concentration increases with depth from approximately 2% up to about 3%, while outside the crater it increases from nearly 2.5% up to approximately 4%.

A key difference between W and Ta emerges from the depth dependence of NRA profiles. While W exhibits a decreasing concentration with depth, Ta shows an increase of average D concentration in the bulk. This behavior suggests a strong contribution from subsurface and bulk retention mechanisms in Ta, with D trapped at depths extending beyond regions directly affected by ablation.

In conclusion, the NRA results confirm that tantalum retains a substantially larger amount of D than tungsten under the same plasma exposure conditions. This outcome provides a quantitative reference for the plasma exposure experiment, with respect to the in-situ LIBS measurements, where the qualitative D_α signal from tantalum was more difficult to detect due to spectral overlap and consequent uncertainties. The combined use of in-situ LIBS and post-mortem NRA therefore proves to be a valuable approach to study both short-term retention dynamics and long-term contributions; this highlights the importance

of employing complementary diagnostics for a comprehensive assessment of hydrogen isotope interaction with PFCs.

7 Conclusions and perspectives

The initial motivation of this thesis was the investigation and conceptual design of an in-situ LIBS as a diagnostic tool for fusion-relevant plasma-material interaction studies for the BiGyM linear device. This early-stage design phase was combined with a numerical investigation of the laser ablation process, developed to support the interpretation of LIBS measurements, and with an experimental study to investigate short- and long-term retention on plasma-exposed tungsten and tantalum samples, developed during a research period at FZJ (Jülich). This thesis integrates diagnostics design, numerical modeling, and experimental activities in order to build a coherent framework to support the future application of LIBS on BiGyM.

In nuclear fusion research, LPDs are widely used as testbeds to reproduce the high particle fluxes and fluences expected in the most critical regions of tokamaks. Thanks to their accessibility, flexibility and cost-effective design, LPDs allow precise control of plasma parameters and excellent reproducibility of experimental conditions, making them particularly suitable for PWI investigations. Within this framework, LIBS has emerged as a promising diagnostic technique for monitoring surface composition and hydrogen isotope retention in PFCs after plasma exposure because of its inherent advantages, such as the absence of sample preparation requirements, the capability to operate in harsh environments, and the possibility to perform remote and in-situ measurements.

The GyM LPD is currently operating at CNR-ISTP Milan within the EUROfusion consortium and it is extensively used for PWI experiments. Its upgraded version, BiGyM, will feature some significant improvements, including the installation of a new plasma source capable of reaching divertor-relevant particle fluxes ($\Gamma_i \leq 10^{23}\,\mathrm{m}^{-2}\,\mathrm{s}^{-1}$), a new sample exposure system, and the integration of advanced diagnostics, among which a picosecond LIBS system. Therefore, the

first part of this thesis focused on the conceptual design and feasibility assessment of a LIBS diagnostic for fusion-relevant studies to be installed on BiGyM, with particular focus on fuel retention. The analysis of reference studies published in the literature and of simple LIBS spectra from fusion-relevant samples allowed to select laser and spectroscopic components for the implementation of the diagnostics.

The chosen laser is a 29 ps Nd:YAG EKSPLA system operating at 1064 nm, with a maximum pulse energy of 70 mJ. For the spectroscopic instrumentation, an IsoPlane 320 spectrometer (Princeton Instruments) was selected due to its compact design and high spectral resolution, achieved through an optical layout that minimizes chromatic aberrations. The spectrometer will be coupled to a PMAX Intensified CCD camera, equipped with a Gen II (super red) intensifier, characterized by a maximum quantum efficiency in the $500-700$ nm wavelength range. This choice allows enhancing sensitivity for hydrogen isotope detection, preserving a good performance in the UV region. Since the laser source is located in a different room from the BiGyM device, a dedicated optical path of approximately 8 m was designed, including fixed mirrors, a motorized steering mirror for beam positioning on the target, and a focusing lens.

A substantial contribution of this thesis is represented by the development of a numerical model of the laser ablation process using the COMSOL Multiphysics finite element software. This activity was conceived as a support tool for LIBS diagnostics: an accurate prediction of the ablation depth and crater geometry is essential for depth-resolved multi-pulse LIBS analyses while the computation of the temperature evolution inside the target allows estimating the spatial extent of thermally induced effects. This aspect is particularly relevant for single-pulse LIBS retention measurements, since heat diffusion during and after the laser pulse can promote thermally-induced phenomena such as hydrogen isotope diffusion and outgassing, potentially capturing signal from layers below the crater bottom.

Since ns lasers are still the most widely adopted technology for LIBS in fusion research, the modeling activity initially focused on this temporal regime. The developed model solves the heat conduction equation including temperature-dependent thermophysical properties, phase change transition, dynamic mesh deformation for material removal, and a semi-empirical approach to describe plasma shielding, accounting for a substantial reduction of the laser energy effectively reaching the target surface. After a preliminary validation against reference results available in the literature, the model was quantitatively validated through comparison with experimental ablation data obtained from irradiation of samples in a low-pressure environment ($p \approx 10^{-2}$ mbar) using a Nd:YAG laser

working at 1064 nm with 10 ns pulses.
Two different materials were investigated: tungsten, the most relevant candidate as PFC for present and future tokamaks and silicon, selected for its markedly different thermophysical properties and lower melting and boiling temperatures. For tungsten, in the fluence range $\sim 4 - 20\,\mathrm{J/cm^2}$, the model showed good agreement with experiments after introducing an additional assumption about the effective laser spot diameter, considering only the central circular region of the ablation crater. Under these conditions, the maximum relative discrepancy for ablation depth remained below 20% (with one isolated outlier), while the crater diameter was reproduced with a maximum discrepancy within 24%. For silicon, two sets of simulations were combined to take into account an experimentally observed variation of the spot diameter, leading to two distinct fluence ranges ($\sim 25 - 60\,\mathrm{J/cm^2}$ for $E \leq 10\,\mathrm{mJ}$ and $\sim 35 - 60\,\mathrm{J/cm^2}$ for $E \geq 12\,\mathrm{mJ}$). In this case, the maximum relative discrepancy was below 25% for ablation depth and below 19% for crater diameter. These results demonstrated that the model is capable of reliably predicting geometrical features of ablation craters for materials with very different properties and over a broad range of fluence. Moreover, the computation of the temperature field evolution enables the estimation of the HAZ extent. For example, at the maximum investigated fluence, the molten region extends down to depths of several hundreds of nanometers below the crater bottom, reaching approximately 700 nm for tungsten and 600 nm for silicon at about 10 ns after pulse termination.
In preparation for the LIBS activity foreseen on BiGyM, the modeling framework was extended to simulate ps pulse regime. In this case, a Two-Temperature Model (TTM) was adopted to separately describe the heating dynamics of electrons and lattice subsystems, while plasma shielding was neglected due to the short pulse duration. The model was validated against laser irradiation experiments performed on tungsten, in a low-pressure argon atmosphere, using a 1030 nm laser with 10 ps pulses. The energy ranged from 1.5 to 4 mJ, corresponding to a fluence range of approximately $4 - 12\,\mathrm{J/cm^2}$. The simulated ablation depth showed good agreement with experimental data, with relative discrepancies below 20% over most of the investigated energy range. A larger deviation occurs at the highest energy point, reaching nearly 38%, where a change of the experimental trend – likely caused by reduced effective intensity at the crater bottom or enhanced redeposition – is observed. The crater diameter trend with pulse energy is also well reproduced, with discrepancies always below 25%. The analysis of the post-pulse temperature field indicated a much more confined thermal impact compared to the ns case, with the molten region extending to about 100 nm below the crater bottom after 30 ps from laser pulse arrival.

Taken together, the modeling results obtained in both the nanosecond and picosecond regimes demonstrate a solid predictive capability for crater geometry, particularly in terms of depth and diameter trends with fluence, which are essential for defining the spatial and depth resolution of LIBS measurements. Beyond geometric considerations, the capability to estimate the temperature field evolution and the HAZ represents a key added value of the modeling approach. In future studies, the thermal outputs obtained could be coupled with a reaction-diffusion model to simulate temperature-driven transport processes of hydrogen isotopes during laser ablation [104], thereby supporting the interpretation of single-pulse LIBS retention results.

As possible future developments, the model could be extended from two to three dimensions to account for the ellipticity of the laser spot, introducing, when experimental measurements are available, the actual spatial distribution of the laser intensity. A further improvement could consist in including, even in a simplified form, gas-dynamics equations, incorporating an additional term that accounts for redeposition and a formulation to estimate the ionization degree, with the ultimate goal of developing a predictive capability for the plasma plume parameters. Another relevant extension would be the simulation of multiple successive pulses, introducing a surface modulation to mimic roughness, with the aim of investigating how the surface morphology evolves over time.

The final part of the thesis focused on in-situ LIBS measurements of short-term retention on fusion-relevant samples during and after exposure to deuterium plasma in the PSI-2 linear device. Two materials were investigated: tungsten and tantalum, the latter being a less studied but promising candidate for fusion applications, for which retention data (expected to be more severe than in tungsten) are scarce in the literature. Samples were exposed for approximately three hours, reaching a total fluence of $\sim 3.3 \cdot 10^{25}\,\mathrm{m}^{-2}$ with an estimated ion energy of around 80 eV.

Qualitative outgassing curves were reconstructed by tracking the integrated intensity of the D_α emission line across successive spectra acquired after the end of the plasma exposure. Since no absolute calibration was performed, these curves represent only a qualitative temporal evolution of the deuterium signal associated with the first LIBS pulse, to ensure sampling of the surface-trapped deuterium only.

A comparison between tungsten and tantalum curves suggested a faster decrease of deuterium signal during the first 150 min after plasma termination. However, these results must be interpreted with caution, because the D_α line in tantalum spectra is affected by overlap with nearby emission lines, leading to a difficult signal detection especially for longer times. For this reason, the investigation of

alternative spectral lines, such as D_β, may represent, despite its lower intensity, a valuable improvement for future experiments on tantalum retention.
To provide a quantitative reference for deuterium concentration, complementary NRA measurements were performed on the same samples analyzed by LIBS. NRA mapping around a LIBS crater, with depth resolution around 3.5 μm, showed that tantalum retains substantially more deuterium than tungsten under the same exposure conditions. Reconstructed deuterium depth profiles indicated near-surface concentrations for tungsten between 0.1% and 0.04%, decreasing with depth. In contrast, tantalum showed a near-surface deuterium content of about 2% and 3%, almost two orders of magnitude higher than tungsten, with high local variability and a tendency to increase toward the bulk. This behavior supports the conclusion that, under the investigated conditions, bulk trapping mechanism could play a more significant role in tantalum than in tungsten.
Overall, the work presented in this thesis highlights the importance and potential of numerical modeling as a support tool for LIBS diagnostics, providing validated results for both ns and ps ablation regimes; the latter will be directly relevant for future experiments on the BiGyM linear device. Moreover, in-situ LIBS measurements demonstrated the capability of the technique to probe short-term deuterium retention, highlighting also the difficulties when dealing with signal identification in the presence of spectral overlap, as in the case of tantalum. The combined use of LIBS and NRA proved to be essential to obtain a consistent and physically grounded interpretation of hydrogen isotope retention, ultimately confirming the significantly higher deuterium concentration in tantalum compared to tungsten despite the difficulties about signal identification.

Bibliography

[1] F. Crescenzi, H. Greuner, S. Roccella, E. Visca, and J.H. You. ITER-like divertor target for DEMO: Design study and fabrication test. *Fusion Engineering and Design*, 124:432–436, November 2017. ISSN 09203796. doi:10.1016/j.fusengdes.2017.02.014.

[2] INTERNATIONAL ATOMIC ENERGY AGENCY. Summary of the ITER Final Design Report. Technical report, IAEA, Vienna, 2001.

[3] C. Bachmann, G. Aiello, R. Albanese, R. Ambrosino, F. Arbeiter, J. Aubert, L. Boccaccini, D. Carloni, G. Federici, U. Fischer, M. Kovari, A. Li Puma, A. Loving, I. Maione, M. Mattei, G. Mazzone, B. Meszaros, I. Palermo, P. Pereslavtsev, V. Riccardo, P. Sardain, N. Taylor, S. Villari, Z. Vizvary, A. Vaccaro, E. Visca, and R. Wenninger. Initial DEMO tokamak design configuration studies. *Fusion Engineering and Design*, 98–99:1423–1426, October 2015. ISSN 09203796. doi:10.1016/j.fusengdes.2015.05.027.

[4] J. P. Freidberg. *Plasma Physics and Fusion Energy*. Cambridge Univ. Press, Cambridge, 1. paperback ed edition, 2008. ISBN 978-0-521-85107-7 978-0-521-73317-5.

[5] J. Wesson. *Tokamaks*. Number 149 in International Series of Monographs on Physics. Oxford Univ. Press, Oxford, 4. ed edition, 2011. ISBN 978-0-19-959223-4.

[6] H. P. Furth. Fusion energy development: Breakeven and beyond. *Journal of Fusion Energy*, 7(2-3):99–106, September 1988. ISSN 0164-0313, 1572-9591. doi:10.1007/BF01054628.

[7] S. Li, H. Jiang, Z. Ren, and C. Xu. Optimal Tracking for a Divergent-Type Parabolic PDE System in Current Profile Control. *Abstract and Applied Analysis*, 2014:1–8, 2014. ISSN 1085-3375, 1687-0409. doi:10.1155/2014/940965.

[8] S. I. Krasheninnikov and A. S. Kukushkin. Physics of ultimate detachment of a tokamak divertor plasma. *Journal of Plasma Physics*, 83(5):155830501, October 2017. ISSN 0022-3778, 1469-7807. doi:10.1017/S0022377817000654.

[9] M. Huguet, K. Dietz, J. L. Hemmerich, and J. R. Last. The JET Machine: Design, Construction, and Operation of the Major Systems. *Fusion Technology*, 11(1):43–70, January 1987. ISSN 0748-1896. doi:10.13182/FST87-A25000.

[10] P. Barabaschi, Y. Kamada, H. Shirai, and the JT-60SA Integrated Project Team. Progress of the JT-60SA project. *Nuclear Fusion*, 59(11): 112005, November 2019. ISSN 0029-5515, 1741-4326. doi:10.1088/1741-4326/ab03f6.

[11] J. Hu, W. Xi, J. Zhang, L. Huang, D. Yao, Q. Zang, Y. Hu, G. Zuo, Q. Yuan, J. Qian, Z. Zhou, X. Zhang, M. Wang, H. Xu, Y. Xie, Z. Wang, H. Liu, Y. Sun, L. Wang, G. Li, H. Yin, Y. Yang, X. Gong, K. Lu, G. Xu, J. Chen, F. Liu, J. Li, Y. Song, and the EAST team. All superconducting tokamak: EAST. *AAPPS Bulletin*, 33(1):8, April 2023. ISSN 2309-4710. doi:10.1007/s43673-023-00080-9.

[12] A. Kallenbach, R. Dux, R. Fischer, J. C. Fuchs, J. Hobirk, A. Kappatou, T. Lunt, T. Pütterich, V. Rohde, P. A. Schneider, B. Sieglin, M. Teschke, W. Treutterer, and the ASDEX Upgrade Team. Operation of the ASDEX Upgrade tokamak. *Plasma Physics and Controlled Fusion*, 67(8):085005, August 2025. ISSN 0741-3335, 1361-6587. doi:10.1088/1361-6587/adf257.

[13] A. J. Creely, M. J. Greenwald, S. B. Ballinger, D. Brunner, J. Canik, J. Doody, T. Fülöp, D. T. Garnier, R. Granetz, T. K. Gray, C. Holland, N. T. Howard, J. W. Hughes, J. H. Irby, V. A. Izzo, G. J. Kramer, A. Q. Kuang, B. LaBombard, Y. Lin, B. Lipschultz, N. C. Logan, J. D. Lore, E. S. Marmar, K. Montes, R. T. Mumgaard, C. Paz-Soldan, C. Rea, M. L. Reinke, P. Rodriguez-Fernandez, K. Särkimäki, F. Sciortino, S. D. Scott, A. Snicker, P. B. Snyder, B. N. Sorbom, R. Sweeney, R. A. Tinguely, E. A. Tolman, M. Umansky, O. Vallhagen, J. Varje, D. G. Whyte, J. C. Wright, S. J. Wukitch, J. Zhu, and the SPARC Team. Overview of the SPARC tokamak. *Journal of Plasma Physics*, 86(5):865860502, October 2020. ISSN 0022-3778, 1469-7807. doi:10.1017/S0022377820001257.

[14] M. Merola, D. Loesser, A. Martin, P. Chappuis, R. Mitteau, V. Komarov, R.A. Pitts, S. Gicquel, V. Barabash, L. Giancarli, J. Palmer, M. Nakahira, A. Loarte, D. Campbell, R. Eaton, A. Kukushkin, M. Sugihara, F. Zhang, C.S. Kim, R. Raffray, L. Ferrand, D. Yao, S. Sadakov, A. Furmanek, V. Rozov, T. Hirai, F. Escourbiac, T. Jokinen, B. Calcagno, and S. Mori. ITER plasma-facing components. *Fusion Engineering and Design*, 85(10-12):2312–2322, December 2010. ISSN 09203796. doi:10.1016/j.fusengdes.2010.09.013.

[15] J. Roth, E. Tsitrone, and A. Loarte. Plasma–wall interaction: Important ion induced surface processes and strategy of the EU Task Force. *Nuclear Instruments and Methods in Physics Research Section B: Beam Interactions with Materials and Atoms*, 258(1):253–263, May 2007. ISSN 0168583X. doi:10.1016/j.nimb.2006.12.168.

[16] J. Roth, E. Tsitrone, A. Loarte, Th. Loarer, G. Counsell, R. Neu, V. Philipps, S. Brezinsek, M. Lehnen, P. Coad, Ch. Grisolia, K. Schmid, K. Krieger, A. Kallenbach, B. Lipschultz, R. Doerner, R. Causey, V. Alimov, W. Shu, O. Ogorodnikova, A. Kirschner, G. Federici, and A. Kukushkin. Recent analysis of key plasma wall interactions issues for ITER. *Journal of Nuclear Materials*, 390–391:1–9, June 2009. ISSN 00223115. doi:10.1016/j.jnucmat.2009.01.037.

[17] M. J. Van De Pol, S. Alonso Van Der Westen, D. U. B. Aussems, M. A. Van Den Berg, S. Brons, H. J. N. Van Eck, G. G. Van Eden, H. J. W. Genuit, H. J. Van Der Meiden, T. W. Morgan, J. Scholten, J. W. M. Vernimmen, E. G. P. Vos, and M. R. De Baar. Operational characteristics of the superconducting high flux plasma generator Magnum-PSI. *Fusion Engineering and Design*, 136:597–601, November 2018. ISSN 09203796. doi:10.1016/j.fusengdes.2018.03.033.

[18] A. Kreter, C. Brandt, A. Huber, S. Kraus, S. MÖller, M. Reinhart, B. Schweer, G. Sergienko, and B. Unterberg. Linear Plasma Device PSI-2 for Plasma-Material Interaction Studies. *Fusion Science and Technology*, 68(1):8–14, July 2015. ISSN 1536-1055, 1943-7641. doi:10.13182/FST14-906.

[19] Plasma-Wall Interaction in Linear Plasma Devices. https://www.fz-juelich.de/en/ifn/ifn-1/forschung/plasma-wall-interaction-in-linear-plasma-devices, 2025.

[20] A. Uccello, W. Bin, A. Bruschi, F. Causa, A. Cremona, M. De Angeli, D. Farina, G. Gatto, G. Gervasini, F. Ghezzi, G. Gittini, G. Granucci, G. Grosso, L. Laguardia, M. Lontano, V. Mellera, D. Minelli, A. Nardone, M. Pedroni,

F. Ripamonti, N. Rispoli, E. Vassallo, and D. Ricci. Linear plasma device GyM for plasma-material interaction studies. *Frontiers in Physics*, 11: 1108175, February 2023. ISSN 2296-424X. doi:10.3389/fphy.2023.1108175.

[21] F. F. Chen. Helicon discharges and sources: A review. *Plasma Sources Science and Technology*, 24(1):014001, January 2015. ISSN 0963-0252, 1361-6595. doi:10.1088/0963-0252/24/1/014001.

[22] P. Guittienne, A. Howling, and I. Furno. *Resonant Network Antennas for Radio-Frequency Plasma Sources: Theory, Technology and Applications*. IOP Publishing, February 2024. ISBN 978-0-7503-5296-3 978-0-7503-5294-9. doi:10.1088/978-0-7503-5296-3.

[23] O. Svelto and D. C. Hanna. *Principles of Lasers*. Springer, New York, 5th ed edition, 2010. ISBN 978-1-4419-1302-9.

[24] J.-C. Diels and W. Rudolph. *Ultrashort Laser Pulse Phenomena: Fundamentals, Techniques, and Applications on a Femtosecond Time Scale*. Optics and Photonics. Elsevier / Academic Press, Amsterdam ; Boston, 2nd ed edition, 2006. ISBN 978-0-12-215493-5.

[25] G. S. Maurya, A. Marín-Roldán, P. Veis, A. K. Pathak, and P. Sen. A review of the LIBS analysis for the plasma-facing components diagnostics. *Journal of Nuclear Materials*, 541:152417, December 2020. ISSN 00223115. doi:10.1016/j.jnucmat.2020.152417.

[26] S. S. Harilal, B. E. Brumfield, N. L. LaHaye, K. C. Hartig, and M. C. Phillips. Optical spectroscopy of laser-produced plasmas for standoff isotopic analysis. *Applied Physics Reviews*, 5(2):021301, June 2018. ISSN 1931-9401. doi:10.1063/1.5016053.

[27] J. P. Singh and S. N. Thakur, editors. *Laser-Induced Breakdown Spectroscopy*. Elsevier, Amsterdam, Netherlands ; Cambridge, MA, second edition edition, 2020. ISBN 978-0-12-818829-3.

[28] S. S. Mao, X. Mao, R. Greif, and R. E. Russo. Initiation of an early-stage plasma during picosecond laser ablation of solids. *Applied Physics Letters*, 77(16):2464–2466, 2000.

[29] S. S. Harilal, J. R. Freeman, P. Diwakar, and A. Hassanein. Comparison of nanosecond and femtosecond LIBS. In *CLEO: 2013*, page CTu2H.8, San Jose, California, 2013. OSA. ISBN 978-1-55752-972-5. doi:10.1364/CLEO_SI.2013.CTu2H.8.

[30] C. Li, D. Xu, S. Song, and X. Gao. Enhancement of spectral line intensity and lifetime of femtosecond laser-induced Cu plasma in a cylindrical cavity. *Optik*, 271:170113, December 2022. ISSN 00304026. doi:10.1016/j.ijleo.2022.170113.

[31] S. Mittelmann. *Optical Emission Spectroscopy of Ultra-Short Laser-induced Plasmas*. PhD thesis, Heinrich-Heine-Universität Düsseldorf, February 2023.

[32] M. Born and E. Wolf. *Principles of Optics: Electromagnetic Theory of Propagation, Interference and Diffraction of Light*. Cambridge University Press, Cambridge ; New York, 7th expanded ed edition, 1999. ISBN 978-0-521-64222-4 978-0-521-63921-7.

[33] Y. Zhang, F. Wang, J. Liu, and J. Sun. Simulation of the inverse bremsstrahlung absorption by plasma plume in laser penetration welding. *Chemical Physics Letters*, 793:139434, April 2022. ISSN 00092614. doi:10.1016/j.cplett.2022.139434.

[34] P. M. Ossi. *Plasmi per superfici*. Polipress, Milano, 2006. ISBN 978-88-7398-026-1.

[35] R. Rozman, I. Grabec, and E. Govekar. Influence of absorption mechanisms on laser-induced plasma plume. *Applied Surface Science*, 254(11):3295–3305, March 2008. ISSN 01694332. doi:10.1016/j.apsusc.2007.11.029.

[36] W. L. Kruer. *The Physics of Laser Plasma Interactions*. Frontiers in Physics. Boulder, Colo. [u.a.] Westview, 2003. ISBN 978-0-8133-4083-8.

[37] S.-A. Irimiciuc. *Experimental and Theoretical Studies on the Dynamics of Transient Plasma Plumes Generated by Laser Ablation in Various Temporal Regimes*. PhD thesis, Alexandru Ioan Cuza" University, October 2017.

[38] M. V. Shugaev, M. He, Y. Levy, A. Mazzi, A. Miotello, N. M. Bulgakova, and L. V. Zhigilei. Laser-Induced Thermal Processes: Heat Transfer, Generation of Stresses, Melting and Solidification, Vaporization, and Phase Explosion. In Koji Sugioka, editor, *Handbook of Laser Micro- and Nano-Engineering*, pages 83–163. Springer International Publishing, Cham, 2021. ISBN 978-3-030-63646-3 978-3-030-63647-0. doi:10.1007/978-3-030-63647-0_11.

[39] D. N. Wang, Y. Wang, and C. R. Liao. Femtosecond laser micromachining on optical fiber. In *Laser Surface Engineering*, pages 359–381. Elsevier, 2015. ISBN 978-1-78242-074-3. doi:10.1016/B978-1-78242-074-3.00014-3.

[40] A. Ikeda, M. Matsumoto, S. Ogura, T. Okano, and K. Fukutani. Knudsen layer formation in laser induced thermal desorption. *The Journal of Chemical Physics*, 138(12):124705, March 2013. ISSN 0021-9606, 1089-7690. doi:10.1063/1.4795827.

[41] J. Wu, Y. Qiu, X. Li, H. Yu, Z. Zhang, and A. Qiu. Progress of laser-induced breakdown spectroscopy in nuclear industry applications. *Journal of Physics D: Applied Physics*, 53(2):023001, January 2020. ISSN 0022-3727, 1361-6463. doi:10.1088/1361-6463/ab477a.

[42] A. Ciucci, M. Corsi, V. Palleschi, S. Rastelli, A. Salvetti, and E. Tognoni. New Procedure for Quantitative Elemental Analysis by Laser-Induced Plasma Spectroscopy. *Applied Spectroscopy*, 53(8):960–964, August 1999. ISSN 0003-7028, 1943-3530. doi:10.1366/0003702991947612.

[43] N. Zhang, T. Ou, M. Wang, Z. Lin, C. Lv, Y. Qin, J. Li, H. Yang, N. Zhao, and Q. Zhang. A Brief Review of Calibration-Free Laser-Induced Breakdown Spectroscopy. *Frontiers in Physics*, 10:887171, June 2022. ISSN 2296-424X. doi:10.3389/fphy.2022.887171.

[44] A. Marín Roldán, M. Pisarčík, M. Veis, M. Držík, and P. Veis. Calibration-free analysis of a tungsten-based target for diagnostics of relevant fusion materials comparing picosecond and nanosecond LIBS. *Spectrochimica Acta Part B: Atomic Spectroscopy*, 177:106055, March 2021. ISSN 05848547. doi:10.1016/j.sab.2020.106055.

[45] P. Veis, A. Marín-Roldán, V. Dwivedi, J. Karhunen, P. Paris, I. Jõgi, C. Porosnicu, C. P. Lungu, V. Nemanic, and A. Hakola. Quantification of H/D content in Be/W mixtures coatings by CF-LIBS. *Physica Scripta*, 2020 (T171):014073, January 2020. ISSN 0031-8949, 1402-4896. doi:10.1088/1402-4896/ab7ebd.

[46] L. Mercadier, A. Semerok, P.A. Kizub, A.V. Leontyev, J. Hermann, C. Grisolia, and P.-Y. Thro. In-depth analysis of ITER-like samples composition using laser-induced breakdown spectroscopy. *Journal of Nuclear Materials*, 414 (3):485–491, July 2011. ISSN 00223115. doi:10.1016/j.jnucmat.2011.05.030.

[47] J. Oelmann, C. Li, S. Brezinsek, M. Rasinski, C. P. Dhard, R. König, V. Winters, and C. Linsmeier. Depth resolved analysis of hydrogen in W7-X graphite components using laser-induced ablation-quadrupole mass spectrometry (LIA-QMS). *Nuclear Materials and Energy*, 18:153–158, January 2019. ISSN 23521791. doi:10.1016/j.nme.2018.12.019.

[48] D. Zhao, C. Li, Z. Hu, C. Feng, Q. Xiao, R. Hai, P. Liu, L. Sun, D. Wu, C. Fu, J. Liu, N. Farid, F. Ding, G.-N. Luo, L. Wang, and H. Ding. Remote *in situ* laser-induced breakdown spectroscopic approach for diagnosis of the plasma facing components on experimental advanced superconducting tokamak. *Review of Scientific Instruments*, 89(7):073501, July 2018. ISSN 0034-6748, 1089-7623. doi:10.1063/1.5024848.

[49] S. Almaviva, L. Caneve, F. Colao, V. Lazic, G. Maddaluno, P. Mosetti, A. Palucci, A. Reale, P. Gasior, W. Gromelski, and M. Kubkowska. LIBS measurements inside the FTU vessel mock-up by using a robotic arm. *Fusion Engineering and Design*, 157:111685, August 2020. ISSN 09203796. doi:10.1016/j.fusengdes.2020.111685.

[50] J. Ristkok, S. Almaviva, J. Likonen, J. Karhunen, I. Jõgi, P. Paris, S. Soni, P. Veis, S. Atikukke, J. Butikova, R. Yi, I. Jepu, P. Gasior, C. Porosnicu, M. Bojan, B. Solomonea, and S. Brezinsek. Preparing LIBS for in-situ measurements in JET tokamak: System overview and co-deposited layer thicknesses. *Nuclear Materials and Energy*, 44:101968, September 2025. ISSN 23521791. doi:10.1016/j.nme.2025.101968.

[51] R. Yi, R. Rayaprolu, J. Likonen, S. Almaviva, I. Jepu, G. Sergienko, A. Widdowson, N. Jones, S. Atikukke, T. Dittmar, J. Karhunen, P. Gasior, M. Sackers, S. Soni, E. Wüst, J. Butikova, W. Gromelski, A. Hakola, I. Jõgi, P. Paris, J. Ristkok, P. Veis, and S. Brezinsek. In-vessel and depth-resolved semi-quantitative analysis on hydrogen isotopes and wall materials in JET by LIBS operated on a remote handling arm. *Nuclear Materials and Energy*, 45: 102016, December 2025. ISSN 23521791. doi:10.1016/j.nme.2025.102016.

[52] X. Jiang, G. Sergienko, B. Schweer, N. Gierse, M. Hubeny, A. Kreter, S. Brezinsek, and Ch. Linsmeier. Design and development of a LIBS system on linear plasma device PSI-2 for in situ real-time diagnostics of plasma-facing materials. *Nuclear Materials and Energy*, 12:1224–1230, August 2017. ISSN 23521791. doi:10.1016/j.nme.2016.11.021.

[53] X. Jiang, G. Sergienko, B. Schweer, S. Möller, M. Freisinger, A. Kreter, S. Brezinsek, and Ch. Linsmeier. An upgraded LIBS system on linear plasma device PSI-2 for in-situ diagnostics of plasma-facing materials. *Fusion Engineering and Design*, 146:96–99, September 2019. ISSN 09203796. doi:10.1016/j.fusengdes.2018.11.044.

[54] D. Nishijima, R.P. Doerner, M.J. Baldwin, and G.R. Tynan. Dynamic deuterium retention properties of tungsten measured using laser-induced

breakdown spectroscopy. *Nuclear Fusion*, 61(11):116028, November 2021. ISSN 0029-5515, 1741-4326. doi:10.1088/1741-4326/ac26ef.

[55] E. Wüst, T. Schwarz-Selinger, C. Kawan, L. Gao, and S. Brezinsek. Depth-resolved deuterium retention analysis in displacement-damaged tungsten using laser-induced breakdown spectroscopy. *Physics of Plasmas*, 31(8): 082510, August 2024. ISSN 1070-664X, 1089-7674. doi:10.1063/5.0211493.

[56] P. Gasior, M. Bieda, M. Kubkowska, R. Neu, and J. Wolowski. Laser induced breakdown spectroscopy as diagnostics for fuel retention and removal and wall composition in fusion reactors with mixed-material components. *Fusion Engineering and Design*, 86(6-8):1239–1242, October 2011. ISSN 09203796. doi:10.1016/j.fusengdes.2011.02.046.

[57] X. Jiang, G. Sergienko, A. Kreter, S. Brezinsek, and Ch. Linsmeier. In-situ study of short-term retention of deuterium in tungsten during and after plasma exposure in PSI-2. *Nuclear Fusion*, 61(9):096006, September 2021. ISSN 0029-5515, 1741-4326. doi:10.1088/1741-4326/ac112e.

[58] S. Sinha. Nanosecond laser ablation of Thoria fuel pellets for microstructural study. *Journal of Nuclear Materials*, 396(2-3):257–263, January 2010. ISSN 00223115. doi:10.1016/j.jnucmat.2009.11.019.

[59] S. Sinha. Nanosecond laser ablation for pulsed laser deposition of yttria. *Applied Physics A*, 112(4):855–862, September 2013. ISSN 0947-8396, 1432-0630. doi:10.1007/s00339-013-7706-3.

[60] S. Sinha. Thermal model for nanosecond laser ablation of alumina. *Ceramics International*, 41(5):6596–6603, June 2015. ISSN 02728842. doi:10.1016/j.ceramint.2015.01.106.

[61] S. Tao, B. Wu, Y. Zhou, and Y. Gao. Thermal modeling and experimental study of infrared nanosecond laser ablation of silicon. *Journal of Applied Physics*, 106(12):123507, December 2009. ISSN 0021-8979, 1089-7550. doi:10.1063/1.3271413.

[62] Y. Deng, Y. Zhou, Y. Zhang, D. Chen, and X. Zhou. Numerical and experimental analysis of nanosecond laser ablation of SiC. *Materials Science in Semiconductor Processing*, 151:107020, November 2022. ISSN 13698001. doi:10.1016/j.mssp.2022.107020.

[63] Y. Li, J. Li, W. Zhang, and G. Jin. Application of pulsed laser ablation thermal model in nanosecond pulsed laser removal of the epoxy resin

paint film. *Optics & Laser Technology*, 175:110806, August 2024. ISSN 00303992. doi:10.1016/j.optlastec.2024.110806.

[64] X. Wang, Y. Huang, C. Li, and B. Xu. Numerical simulation and experimental study on picosecond laser ablation of stainless steel. *Optics & Laser Technology*, 127:106150, July 2020. ISSN 00303992. doi:10.1016/j.optlastec.2020.106150.

[65] L. Peng, M. Li, P. Wang, X. Li, Y. Zhang, M. He, C. Zhou, H. Zhang, and S. Chen. Numerical simulation and investigation of ultra-short pulse laser ablation on Ti6Al4V and stainless steel. *AIP Advances*, 13(6):065018, June 2023. ISSN 2158-3226. doi:10.1063/5.0152500.

[66] C. Chen, F. Zhang, Y. Zhang, X. Xiong, B.-F. Ju, H. Cui, and Y.-L. Chen. Single-pulse femtosecond laser ablation of monocrystalline silicon: A modeling and experimental study. *Applied Surface Science*, 576:151722, February 2022. ISSN 01694332. doi:10.1016/j.apsusc.2021.151722.

[67] H. J. Van Der Meiden, S. Almaviva, J. Butikova, V. Dwivedi, P. Gasior, W. Gromelski, A. Hakola, X. Jiang, I. Jõgi, J. Karhunen, M. Kubkowska, M. Laan, G. Maddaluno, A. Marín-Roldán, P. Paris, K. Piip, M. Pisarčík, G. Sergienko, M. Veis, P. Veis, S. Brezinsek, and The EUROfusion Wp Pfc Team. Monitoring of tritium and impurities in the first wall of fusion devices using a LIBS based diagnostic. *Nuclear Fusion*, 61(12):125001, December 2021. ISSN 0029-5515, 1741-4326. doi:10.1088/1741-4326/ac31d6.

[68] D. Zhao, D. Wu, J. Oelmann, S. Brezinsek, Q. Xiao, R. Yi, L. Cai, and H. Ding. Highly depth-resolved characterization of fusion-related tungsten material based on picosecond laser-induced breakdown spectroscopy. *Journal of Analytical Atomic Spectrometry*, 35(12):2867–2879, 2020. ISSN 0267-9477, 1364-5544. doi:10.1039/D0JA00340A.

[69] J. Cheng, J. Cao, Y. Huang, S. Edwardson, W. Perrie, G. Dearden, and D. Liu. Metal ablation study with a 10 picosecond laser under low and median fluence. *Optics & Laser Technology*, 121:105792, January 2020. ISSN 00303992. doi:10.1016/j.optlastec.2019.105792.

[70] J. Cheng, W. Perrie, M. Sharp, S. P. Edwardson, N. G. Semaltianos, G. Dearden, and K. G. Watkins. Single-pulse drilling study on Au, Al and Ti alloy by using a picosecond laser. *Applied Physics A*, 95(3):739–746, June 2009. ISSN 0947-8396, 1432-0630. doi:10.1007/s00339-008-5037-6.

[71] D. Zhao, N. Gierse, J. Oelmann, S. Brezinsek, M. Rasinski, Y. Liang, C. Linsmeier, and H. Ding. Investigation of laser ablation features of molybdenum bulk for picosecond laser-based techniques in fusion devices. *Fusion Engineering and Design*, 151:111379, February 2020. ISSN 09203796. doi:10.1016/j.fusengdes.2019.111379.

[72] A. Uccello. *Development of Nanostructured Rhodium Films for Diagnostic Mirrors Employed in Nuclear Fusion Systems*. PhD thesis, Politecnico di Milano, March 2014.

[73] A. Bultel, V. Morel, A. Favre, G. Godard, A. Benyagoub, I. Monnet, A. Sémérok, M. Dinescu, S. Markelj, P. Magaud, and C. Grisolia. Towards ps-LIBS tritium measurements in W/Al materials. *Fusion Engineering and Design*, 146:1971–1974, September 2019. ISSN 09203796. doi:10.1016/j.fusengdes.2019.03.079.

[74] M. Fikry, W. Tawfik, and M. M. Omar. Investigation on the effects of laser parameters on the plasma profile of copper using picosecond laser induced plasma spectroscopy. *Optical and Quantum Electronics*, 52(5):249, May 2020. ISSN 0306-8919, 1572-817X. doi:10.1007/s11082-020-02381-x.

[75] R. Noll. *Laser-Induced Breakdown Spectroscopy: Fundamentals and Applications*. Physics and Astronomy (Springer-11651). Springer Berlin Heidelberg Springer e-books, Berlin, Heidelberg, 2012 edition, 2012. ISBN 978-3-642-20668-9.

[76] C. Palmer and E. G. Lowen. *Diffraction Gratings Handbook*. Richardson Gratings, Newport Corporation. MKS Instruments, Inc., Rochester, New York, USA, 7th edition, 2014.

[77] COMSOL AB. COMSOL Multiphysics v6.1. Technical report, COMSOL AB, Stockholm, Sweden, 2023.

[78] S. Cipelli, A. Hussain, G. Dilecce, P. F. Ambrico, D. Aceto, A. Cremona, I. Casiraghi, O. De Pascale, L. Laguardia, M. Pedroni, D. Ricci, D. Ripamonti, J. Scionti, and A. Uccello. Nanosecond laser ablation modeling of silicon and tungsten as support activity for LIBS diagnostic. *Journal of Nuclear Materials*, 620:156315, February 2026. ISSN 00223115. doi:10.1016/j.jnucmat.2025.156315.

[79] H. D. Vora, S. Santhanakrishnan, S. P. Harimkar, S. K. S. Boetcher, and N. B. Dahotre. Evolution of surface topography in one-dimensional

laser machining of structural alumina. *Journal of the European Ceramic Society*, 32(16):4205–4218, December 2012. ISSN 09552219. doi:10.1016/j.jeurceramsoc.2012.06.015.

[80] COMSOL AB. Heat Transfer Module User's Guide. Technical Report v6.1, COMSOL AB, Stockholm, Sweden, 2023.

[81] E. Ohmura. Temperature Rise of Silicon Due to Absorption of Permeable Pulse Laser. In Vyacheslav Vikhrenko, editor, *Heat Transfer - Engineering Applications*. InTech, December 2011. ISBN 978-953-307-361-3. doi:10.5772/28046.

[82] T. Moscicki. Differences in Nanosecond Laser Ablation and Deposition of Tungsten, Boron, and WB_2 /B Composite due to Optical Properties. *International Journal of Optics*, 2016:1–13, 2016. ISSN 1687-9384, 1687-9392. doi:10.1155/2016/5438721.

[83] G. Galasso. *Modelling the Nanosecond Laser Ablation of a Silicon Target*. PhD thesis, Technische Universit{\"a}t Wien, 2017.

[84] E. J. Kautz, D. J. Senor, and S. S. Harilal. The interplay between laser focusing conditions, expansion dynamics, ablation mechanisms, and emission intensity in ultrafast laser-produced plasmas. *Journal of Applied Physics*, 130(20):204901, November 2021. ISSN 0021-8979, 1089-7550. doi:10.1063/5.0069732.

[85] A. V. Bulgakov and N. M. Bulgakova. Thermal model of pulsed laser ablation under the conditions of formation and heating of a radiation-absorbing plasma. *Quantum Electronics*, 29(5):433–437, May 1999. ISSN 1063-7818, 1468-4799. doi:10.1070/QE1999v029n05ABEH001503.

[86] J. Straus, K. Kolacek, J. Schmidt, O. Frolov, M. Vilemova, J. Matejicek, A. Jager, L. Juha, M. Toufarova, A. Choukourov, and K. Kasuya. Response of fusion plasma-facing materials to nanosecond pulses of extreme ultraviolet radiation. *Laser and Particle Beams*, 36(3):293–307, September 2018. ISSN 0263-0346, 1469-803X. doi:10.1017/S0263034618000332.

[87] P. Tolias. Analytical expressions for thermophysical properties of solid and liquid tungsten relevant for fusion applications. *Nuclear Materials and Energy*, 13:42–57, December 2017. ISSN 23521791. doi:10.1016/j.nme.2017.08.002.

[88] Y. Zhang, J. R. G. Evans, and S. Yang. Corrected Values for Boiling Points and Enthalpies of Vaporization of Elements in Handbooks. *Journal of*

Chemical & Engineering Data, 56(2):328–337, February 2011. ISSN 0021-9568, 1520-5134. doi:10.1021/je1011086.

[89] A. D. Rakhel, A. Kloss, and H. Hess. On the Critical Point of Tungsten. *International Journal of Thermophysics*, 23(5):1369–1380, September 2002. ISSN 0195-928X, 1572-9567. doi:10.1023/A:1019873110953.

[90] S. Mittelmann, J. Riedlinger, B. Buchner, T. Schwarz-Selinger, M. Mayer, and G. Pretzler. Ablation characteristics of tungsten with ultra-short laser pulses. *Journal of Applied Physics*, 136(10):103103, September 2024. ISSN 0021-8979, 1089-7550. doi:10.1063/5.0222073.

[91] D. R. Lide. *CRC Handbook of Chemistry And Physics*. CRC press, 1993.

[92] J. Zhang, L. Zhao, A. Rosenkranz, C. Song, Y. Yan, and T. Sun. Nanosecond pulsed laser ablation of silicon—finite element simulation and experimental validation. *Journal of Micromechanics and Microengineering*, 29(7):075009, July 2019. ISSN 0960-1317, 1361-6439. doi:10.1088/1361-6439/ab208b.

[93] M. De Podesta. *Understanding the Properties of Matter*. CRC press, 2020.

[94] N. M. Bulgakova. Theoretical Models and Qualitative Interpretations of fs Laser Material Processing. *Journal of Laser Micro/Nanoengineering*, 2(1): 76–86, March 2007. ISSN 18800688. doi:10.2961/jlmn.2007.01.0014.

[95] G. Savriama and N. Semmar. Numerical Simulation of Laser Processing Materials: An Engineering Approach. In Noreen Sher Akbar and O. Anwar Beg, editors, *Modeling and Simulation in Engineering Sciences*. InTech, August 2016. ISBN 978-953-51-2608-9 978-953-51-2609-6. doi:10.5772/63945.

[96] MATLAB. Image Processing Toolbox User's Guide. Technical Report MATLAB R2022b, The MathwWorks, Inc., Natick, MA, USA, 2022.

[97] Z. Lin, L. V. Zhigilei, and V. Celli. Electron-phonon coupling and electron heat capacity of metals under conditions of strong electron-phonon nonequilibrium. *Physical Review B*, 77(7):075133, February 2008. ISSN 1098-0121, 1550-235X. doi:10.1103/PhysRevB.77.075133.

[98] P. Dominic, D. Iabbaden, F. Bourquard, S. Reynaud, A. Nakhoul, A. Weck, J.-F. Colombier, and F. Garrelie. Unveiling nature and consequences of tungsten oxidation upon ultrafast laser irradiation. *Applied Surface Science*, 655:159580, May 2024. ISSN 01694332. doi:10.1016/j.apsusc.2024.159580.

[99] J. P. Colombier, P. Combis, F. Bonneau, R. Le Harzic, and E. Audouard. Hydrodynamic simulations of metal ablation by femtosecond laser irradiation. *Physical Review B*, 71(16):165406, April 2005. ISSN 1098-0121, 1550-235X. doi:10.1103/PhysRevB.71.165406.

[100] T.J. Novakowski, A. Sundaram, J.K. Tripathi, S. Gonderman, and A. Hassanein. Deuterium desorption from ion-irradiated tantalum and effects on surface morphology. *Journal of Nuclear Materials*, 504:1–7, June 2018. ISSN 00223115. doi:10.1016/j.jnucmat.2018.03.023.

[101] W. T. Chandler and R. J. Walter. Hydrogen Effects in Refractory Metals. In I. Machlin, R. T. Begley, and E. D. Weisert, editors, *Refractory Metal Alloys Metallurgy and Technology*, pages 197–249. Springer US, Boston, MA, 1968. ISBN 978-1-4684-9122-7 978-1-4684-9120-3. doi:10.1007/978-1-4684-9120-3_6.

[102] D. Nishijima, M. Patino, and R. P. Doerner. Development of a LIBS system for *in-situ* surface measurements during plasma exposure in PISCES-A. *Review of Scientific Instruments*, 89(10):10J105, October 2018. ISSN 0034-6748, 1089-7623. doi:10.1063/1.5034349.

[103] A. Kramida and Y. Ralchenko. NIST Atomic Spectra Database, NIST Standard Reference Database 78, 1999.

[104] D. Matveev, X. Jiang, G. Sergienko, A. Kreter, S. Brezinsek, and C. Linsmeier. Short-term retention in metallic PFCs: Modelling in view of mass spectrometry and LIBS. *Physica Scripta*, 96(12):124079, December 2021. ISSN 0031-8949, 1402-4896. doi:10.1088/1402-4896/ac43d6.

Acknowledgments

Prima di tutto desidero ringraziare la mia supervisora Anna per essere sempre stata disponibile e per il prezioso supporto fornito durante la scrittura di questa tesi. Grazie per essere stata sempre presente, anche ad orari poco convenzionali e per l'efficienza con cui mi hai sempre aiutato a risolvere problemi scientifici e burocratici.
Un sentito ringraziamento va al mio secondo supervisore, il professor Gianmaria De Tommasi, che nonostante la distanza è stato sempre disponibile per ogni dubbio e chiarimento.
Un grande grazie anche ad Andrea, per essere sempre stato pronto a darmi una mano anche quando gli argomenti erano più ostici. Senza i tuoi consigli e i continui confronti molti dubbi sarebbero ancora lì a rallentarmi.
Ringrazio inoltre tutti i membri del gruppo (Bi)GyM, tra cui Irene, Francesco, Laura, Daria, Matteo e tutti gli altri. Spero che, con il contributo di tutti, l'upgrade della macchina possa essere completato al più presto, per puntare a nuovi e importanti risultati scientifici.
Un ringraziamento particolare va ai miei due compagni di ufficio: Luca, che mi ha accompagnato nella prima parte di questo percorso, e Jimmy, per la seconda. Grazie Jimmy per esser sempre disponibile per ogni dubbio o consiglio e per non tirarti mai indietro quando mi serve una mano.
Un grande ringraziamento va anche ai colleghi di Bari, Giorgio, Paolo, Domenico, Arshad e alla direttrice Olga. Grazie per avermi accolto durante le mie due visite e per tutto il supporto fornito nello svolgimento degli esperimenti e nel confronto sui risultati ottenuti. Senza di voi, la validazione sperimentale non sarebbe stata possibile.
Ringrazio infine Dario Ripamonti dell'Istituto ICMATE per la grande disponi-

bilità e per il supporto nelle misure SEM, risultate estremamente utili per l'interpretazione degli esperimenti.
I would like to express my sincere gratitude to Sebastijan Brezinsek for giving me the opportunity to carry out a research experience at the Forschungszentrum Jülich, which proved to be fundamental for my personal growth as a Ph.D. student and as a scientist. The visiting period in Jülich allowed me to gain hands-on experience with laser systems and LIBS diagnostics, as well as to obtain key results that significantly contributed to this thesis.
I would also like to thank all the people who supported me during this experience. In particular, I am deeply grateful to Rongxing for his help in preparing and performing the experiments, and for patiently addressing all my questions. I also thank Gennady, Dmitry, and Arkadi, for their assistance and valuable suggestions. I would also like to extend my gratitude to Sören Möller for providing me the NRA measurements.
I am deeply grateful to my office mate in Jülich, Erik, as well as Christoph and all the other colleagues I met there, for warmly welcoming me into the research group and involving me in all the activities.
Finally, I would like to thank all the friends I met during my stay in Jülich — Vincenzo, Alvaro, Giorgi, Lev, Tomasz, Wajahat, Giorgi, and Danish — for the time spent together at the Guesthouse, the parties, and all the wonderful moments we shared. I truly hope that our paths will cross again in the future.
Ringrazio anche chi non ha fatto parte di questo percorso, ma ha fatto parte della mia vita. Un enorme grazie ad Ale e Genzo per essere i miei punti di riferimento fin da quando eravamo alti così.
Grazie ai miei amici di capodanno per avermi regalato feste straordinarie e anche ai miei amici di Lodi per essere delle certezze nella mia vita. Un grande grazie in particolare a Ste, compagno di ping pong e altre mille avventure. Grazie perché anche nei momenti più difficili cerchi sempre di tirarmi su e mai di abbattermi. Grazie anche a tutti gli amici che non leggeranno questi ringraziamenti forse un po' troppo formali; dopotutto, prima o poi, questa tesi doveva pur finire!
Infine uno dei grazie più grandi va alla mia famiglia. Grazie a mamma, papà, Francesco ed Elisa per esserci e sostenermi sempre anche quando la mia parte razionale si fa da parte.
Grazie a Maia per tutte le nostre passeggiate. Grazie a zii e cugini per essere una famiglia così unita. Grazie ai miei tre nonni per essere ancora qua, è sempre bellissimo passare del tempo con voi. Grazie a mio nonno Alfonso per tutto quello che mi hai insegnato e perché so che se fossi quaggiù saresti orgoglioso di me.